ACS Catalysis

pubs.acs.org/acscatalysis Review

Geometric and Electronic Effects in Hydrogenation Reactions

Shanjun Mao, Zhe Wang, Qian Luo, Bing Lu, and Yong Wang*

Cite This: ACS Catal. 2023, 13, 974–1019 Read Online

ACCESS | Metrics & More | Article Recommendations

ABSTRACT: Selective hydrogenation has a long history of being an important reaction process for the preparation of high-value chemicals. The geometric and electronic structures of the catalysts largely determine their basic catalytic performance, including activity, selectivity, and stability. However, the complexity of the components and structures of the catalytic active sites poses a significant challenge to the characterization and the sequential performance attribution. On the basis of summarizing the geometric and electronic structure research in this field, this Review will pay special attention to the adsorption and activation modes of reactants, reaction kinetics, identification and classification of structural sensitivity, methods for geometric and electronic regulation, and distinctive concepts for catalyst design, to enlighten the further development of high-efficiency hydrogenation catalysts.

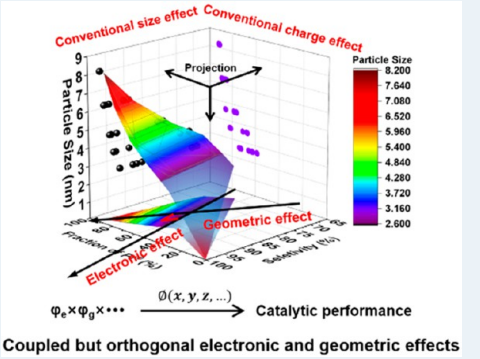

Coupled but orthogonal electronic and geometric effects

KEYWORDS: *Catalysts, hydrogenation reaction, kinetics, electronic effects, geometric effects, recognition conversion*

1. INTRODUCTION

Since drilling for fire, the progress and development of human society has been inseparable from chemistry. From the ancient hydrometallurgy of copper, papermaking, and gunpowder to the modern synthetic ammonia and the extraction of penicillin, the chemical industry has been supporting the growing material demand of human society. However, human society is now facing major problems such as the depletion of fossil resources and environmental pollution. How to efficiently use the limited resources on the Earth and develop green and sustainable chemical production technology has become the focus of attention. As one of the important energy-saving and environmental protection technologies, catalytic technology can greatly accelerate the production efficiency of the chemical industry, reduce the production of waste, play a decisive role in the development of the chemical industry and society, and is known as the "heart" of the organic industry. The first industrial application of catalyst can be traced back to the end of the 19th century for the production of oleum. At present, more than 85% of the global production of chemical products is performed under catalysis, and the annual contribution is estimated to account for 35% of the global DGP.[1]

Catalytic hydrogenation is an important chemical industry process, which is widely used in the synthesis of petrochemical and fine chemical intermediates. It is estimated that ~25% of chemical processes contain at least one hydrogenation process.[2,3] For example, in the petrochemical industry, hydrodenitrification and hydrodesulfurization processes are widely used to remove trace nitrogen/sulfur elements from crude oil.[4] In olefin industry, semi hydrogenation of alkynes is the main way to produce polymer-grade ethylene, propylene, and butene.[5] Cyclohexanone is an important chemical intermediate for the production of nylon-6 or nylon-66.[6] One-step hydrogenation of phenol is an important green and efficient production technology route.[7,8] In addition, hydrogenation of aromatic rings or other unsaturated groups is also one of the important methods to improve oil products.[9−12] At present, bulk industrial chemicals are mostly transformed through the petrochemical route. With the increasing depletion of petrochemical resources, the green and efficient transformation of biomass platform molecules into industrial bulk chemicals and their intermediates by hydrogenation (deoxygenation) reaction is gradually reflecting its importance.[13−16] On the other hand, reducing various reducible functional groups such as −C≡C, −C═C, −C═O, NO_2, −C≡N, −C−OR, COOR, and $CONR_2$ to corresponding key intermediates such as olefins, alcohols, and amines is also a very popular means in the production of fine chemicals.[2,5,17−19]

Selective hydrogenation is the most challenging type of reactions in the field of catalytic hydrogenation. It refers to the process of preferentially reducing only one or part of the functional groups (or substrates) when there are two or more reducible functional groups in the system. Obviously, the degree of response of the catalyst to different functional groups

Received: October 19, 2022
Revised: December 1, 2022
Published: December 30, 2022

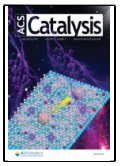

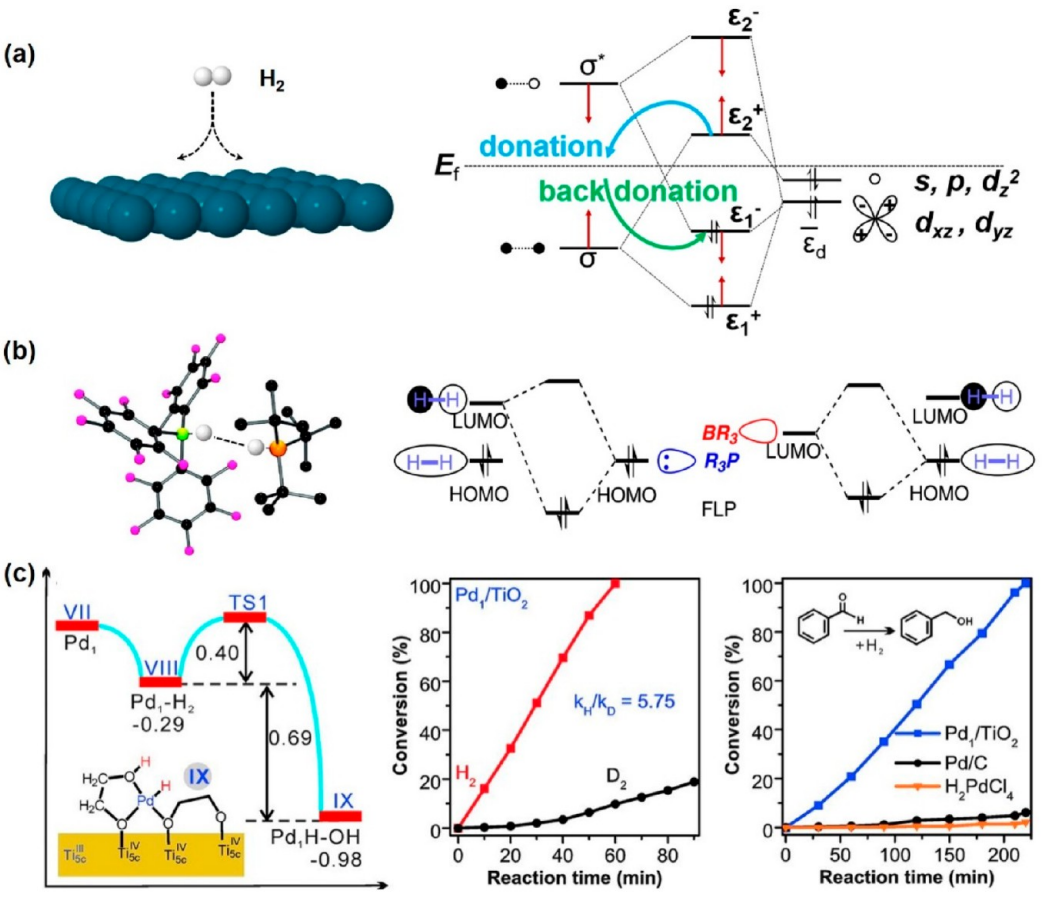

Figure 1. Mechanisms for H_2 dissociation: (a) homolytic cleavage and (b) heterolytic cleavage. [] (c) homolytic cleavage followed by H transfer. [Panel (a) has been reproduced with permission from ref 23 Copyright 2007, American Chemical Society, Washington, DC. Panel (b) has been reproduced with permission from ref 24. Copyright 2013, Thieme Gruppe. Panel (c) has been reproduced with permission from ref 40. Copyright 2016, AAAS.]

will determine the conversion rate of multiple reducible functional groups, and it will ultimately show different reaction selectivity. Supported metal catalysts are commonly used in selective hydrogenation. However, due to the complex and diverse types of active centers of nanometals, the different regulatory mechanisms of carriers on active metals and the impact of reaction microenvironment, it is very challenging to accurately predict and design the actual catalytic performance of catalysts. Therefore, the study of the structure−activity relationship of catalysts is one of the core topics in the design and preparation of efficient heterogeneous selective hydrogenation catalysts.

A typical catalytic hydrogenation process includes chemical adsorption (dissociation), migration, reaction, and product desorption of hydrogen and the reaction substrate at the active site. The activation of H_2 is the premise of hydrogenation reaction. Its activation mode will not only affect the reaction performance of the catalyst, but also involve the understanding of the reaction mechanism. At present, there are two main mechanisms of H_2 activation: homolytic cleavage and homolytic cleavage. However, a considerable number of researchers have deviations in their understanding of these two mechanisms. Therefore, this Review will first introduce the activation mechanism of H_2 and reactant, to explain the process more clearly. Reaction kinetics is a conventional method to study the reaction mechanism and activity. Intrinsic reaction kinetic parameters can provide us with a lot of valuable information about the reaction process, to provide a basis for the design and optimization of catalysts. For example, the reaction order can show the adsorption of reactants, and the reaction activation energy can be used to evaluate the reaction activity of catalytic active sites, and sometimes it can even be used to prove the change of physicochemical parameters during catalyst optimization. Based on the discussion of H_2 activation mechanism, this Review will continue to briefly introduce some contents of hydrogenation kinetics, and elaborate the optimization direction of selective hydrogenation catalyst from the kinetic or macro level. Next, on the basis of the above cognition, we will sort out and summarize the research on the two key physical parameters of the electronic and geometric effects of catalysts in recent years, and then dialectically elaborate the specific reaction system. Finally, through the summary of the research status, we will put forward some enlightening ideas for selective hydrogenation, and make corresponding prospects for the development of this direction in the future.

2. THE ADSORPTION AND ACTIVATION OF H_2 AND REACTANT

2.1. The Adsorption and Activation of H_2. H_2 is the most important hydrogen source in industrial hydrogenation process, so the activation of H_2 is very important for a

https://doi.org/10.1021/acscatal.2c05141
ACS Catal. 2023, 13, 974−1019

hydrogenation catalyst. At present, there are two main mechanisms of H_2 activation, namely, homolytic cleavage and heterolytic cleavage. For transition-metal catalysts, the homolytic cleavage mechanism is generally followed. Figure 1a shows the d-σ* feedback molecular orbital model of homolytic cleavage mechanism.[20] When H_2 interacts with a single transition-metal atom, limited by the orbital symmetry in the three bonding principles, the bonding orbital σ of H_2 recombines with the s, p, and d_{z^2} orbitals of metal atoms to form new bonding orbital ε_1^+ and antibonding orbital ε_2^+; Similarly, the antibonding orbital of σ* in H_2 recombines with the d_{xz} and d_{yz} orbitals of metal atoms to form the new bonding orbital ε_1^- and the antibonding one ε_2^-. Of course, if it interacts with the surface of a metal catalyst, the antibond orbital of H_2 σ* changes to have a linear combination with the d-band of the metal catalyst. When H_2 approaches the surface of a metal catalyst from a long distance, the slight orbital overlap between the bonding orbital of σ in H_2 and s, p, and dz^2 orbitals of metal atoms results in a small splitting between bonding orbital ε_1^+ and antibonding orbital ε_2^+. In accordance, the antibonding orbital ε_2^+ is below the Fermi level (E_f) of the metal surface and in an electron-filled state. As H_2 gradually approaches the catalyst surface closer, splitting between ε_1^+ and ε_2^+ gradually becomes larger, and eventually ε_2^+ crosses over the E_f of the metal surface. At this time, the electrons on ε_2^+ are transferred to the metal catalyst, which also means the electrons in the bonding orbital of σ in H_2 transfer to metal catalysts (σ-donation). Since the bonding orbital of ε_1^- is always below the E_f of the metal surface, the antibonding orbital of H_2 σ* is then in the electron-filled state. It means that the electrons of the metal catalyst are transferred back to H_2 (σ* back-donation), according to the law of charge conservation. Obviously, the relative position of E_f and ε_2^+ or σ determines whether d-σ* feedback can occur and, in turn, determines whether the catalyst can spontaneously activate H_2. For noble metals in group IB, the d-band orbitals are fully filled and E_f lies above the top of the d-band accordingly. Then the ability to activate hydrogen is weak, and a certain activation energy is usually required. For group VIII transition metals, the d-band orbitals are not fully filled and E_f lies in the d-band accordingly, which can activate H_2 spontaneously and realize the barrier-free process.

Because of the influence of the traditional d-σ* feedback mechanism for H_2 activation on the metal catalyst surface, as well as the concern that the presence of oxygen or sulfur species will consume H_2, researchers believed that oxides and sulfides were unsuitable as hydrogenation catalysts under mild conditions for a long time, despite the fact that vanadium aluminum oxide catalysts catalyzed olefin hydrogenation in 1948.[20,21] In recent years, with the discovery of a metal-free hydrogen activation mechanism called "frustrated Lewis acid−base pairs", i.e., heterolytic cleavage as shown in Figure 1b, researchers started to reevaluate the requirements of the electronic structure of the active sites for H_2 activation.[22,23] Different from the homolytic cleavage mechanism on metal catalysts, the heterolytic cleavage mechanism of H_2 on frustrated Lewis acid−base pairs is much easier to understand.[24,25] As shown in Figure 1b, the highest occupied orbital (HOMO) of frustrated Lewis base and the lowest unoccupied orbital (LUMO) of H_2, i.e., the antibonding orbital σ*, interact with each other to fill the LUMO of H_2 with electrons. Then the strength of HOMO in H_2 is weakened. In addition, the LUMO of frustrated Lewis acid interacts with the HOMO of H_2, and draws the electrons of the bonding orbital in H_2, further weakening the strength of HOMO in H_2. Note that H_2 splits to be two bonded ions with opposite charge at the same time of the H−H bond breaking. This phenomenon that H_2 interacts with acid and alkali simultaneously is called "synergistic activation". Therefore, the heterolytic cleavage of H_2 on the frustrated Lewis acid−base pair is also known as the synergistic activation mechanism. Obviously, the performance of synergistic activation is determined by the relative position of their orbital energy levels and the steric hindrance of the frustrated Lewis acid and base sites.

Comparing the two mechanisms on H_2 activation, the biggest difference lies in the fact that the homolytic cleavage mechanism requires the participation of d-orbitals or metal atoms, while the heterolytic cleavage mechanism does not prescribe the type of orbitals. Another difference is that the homolytic cleavage mechanism only requires at least one metal site, while the heterolytic cleavage one requires both acid and alkali sites to participate at the same time. Note that neither of the two mechanisms has clear requirements for the valence state of the catalyst. For example, the heterolytic cleavage mechanism does not have to occur on metallic catalysts. Based on the heterolytic cleavage mechanism, researchers then developed a series of metal-oxide-based selective hydrogenation catalysts. Pérez-Ramírez and co-workers[26,27] and Song et al.[28] found that the formation of oxygen vacancies is crucial to hydrogenation activity. Furthermore, Chrétien and Metiu[29] and Ramirez-Cuesta and co-workers[30] obtained key evidence for the dissociation of hydrogen on La_2O_3 and CeO_2, respectively. Theoretical calculations also found that the oxygen vacancy is the active site for H_2 activation,[31,32] and served as a solid frustrated Lewis acid−base pair. Although these metal-oxide-based hydrogenation catalysts (ZrO_{2-x}, ZnO_{1-x}) are generally less active than supported-metal catalysts, they often show high selectivity.[33,34] For example, CeO_{2-x} and other metal-oxide-based catalysts show a selectivity of 90%−100% for the semihydrogenation of alkynes, which is very promising for the purification of industrial ethylene gas.[26,27,35] Although the overall reaction temperature (>400 K) is higher than the decomposition temperature of some fine chemicals of high added value (only 350 K for retinin (an intermediate for the synthesis of vitamin A), for example),[36] it is possible to further improve the catalytic performance of the catalyst and apply it to the synthesis of fine chemicals by modifying the catalyst.[37] Active heterolytic splitting H species (H^+ and H^-) are also reported to be formed on metal-based catalysts and have a great impact on the activity and selectivity of hydrogenation, since the metal atoms can be regarded as Lewis acids. The addition of triethylamine can promote the heterolytic cleavage of hydrogen on Ru catalyst, so that the turnover frequency (TOF) of toluene hydrogenation increases from 66 h^{-1} to 120 h^{-1}.[38] The pyridine ring in Ru/PVPy can also realize the heterolytic cleavage of H_2, which regulates the reaction mechanism and the selectivity for quinoline hydrogenation. Inspired by this, the author loaded Ru on the strongly alkaline carrier MgO and found a similar effect.[39] Zheng et al. prepared stable monatomic dispersed Pd_1/TiO_2 catalyst with photochemical methods on ultrathin titanium dioxide nanosheets modified with ethylene glycol and considered that the obvious enhanced activity to hydrogenation was attributed to the heterolytic cleavage of H_2, based on a large value of the kinetic isotope effect up to 5.75.[40]

https://doi.org/10.1021/acscatal.2c05141
ACS Catal. 2023, 13, 974−1019

Although several researching results claimed that heterolytic cleavage of H_2 occurs on defective metal oxides, organic base-grafted nanometal catalyst, single atom catalyst, etc., this conclusion should still be drawn more carefully. The question to the current experimental results lies in that they were not obtained through an *in situ* way. In other words, the current results about the H^+ and H^- species cannot tell the difference between the actual heterolytic cleavage of H_2 and the hydrogen spillover process at the interface of heterojunction. In fact, a homolytic cleavage and sequential spillover process should be taken seriously as several theoretical calculation results indicated that H_2 first underwent a molecular chemisorption on a metal site to activate and then split into H^+ and H^- species through sequential spillover, as shown in Figure 1c.[40] Although the final states showed no difference with heterolytic cleavage mechanism, the catalytic performance might vary. For instance, the energy barrier for the hydrogenation of nitroarenes with molecular adsorbed H_2 is only half for that with split atomic H on CoS_2 catalyst.[41] The reason to emphasize this matter is that it is critical for us to explore distinctive catalyst systems that can activate H_2, distinctive H_2 activation mechanisms, and the utilization modes of active hydrogen species in the future.[42−45]

2.2. The Adsorption of Reactant. The adsorption of the reactant on the catalyst is also informative for mechanism study and catalyst design, and closely related with the electronic and geometric effects, especially when several reducible functional groups coexist. Hence, we only discuss the basic adsorption modes of some typical molecules in this section, providing researchers a simple visual reaction picture. Acetylene, ethylene, and acrolein are chosen as the representatives, because of their simplicity of molecular structures and rich connotation for selective hydrogenation investigations.

The adsorption of small hydrocarbons with unsaturated carbon carbon (CC) bonds, such as C_2H_2 and C_2H_4, on transition-metal surfaces is of great scientific significance, because of their frequent involvement in many elementary catalytic reactions in the carbon cycle process for chemical industry, including selective hydrogenation reaction.[2,18,46−48] The prerequisite to a clearer understanding of CC bond transformation on metal surfaces is the unequivocal determination of the basic adsorption sites, bond making mechanisms, geometric structures, and orientations of the adsorbed molecules on metal surfaces. All studies so far have come to the conclusion that, for low adsorbate coverages, the CC bond in adsorbed C_2H_2/C_2H_4 lies parallel to the surface at low temperatures in most cases if no surface reaction occurs, as seen in Figure 2, despite the fact that the kind of bonding varies, depending on the electric and geometric structure of the surface.[49−51] In every instance, the contact with the metal surface via the electrons in CC bond lengthens the carbon−carbon bond and bends the hydrogen atoms away from the surface.[52] The Dewar−Chatt−Duncanson model,[53,54] which was initially presented to explain C_2H_4 coordination in organometallic complexes, is commonly used to describe this form of bonding. In this model, the bonding of CC bonds in C_2H_2/C_2H_4 to the metal surface is described as a donation of π electrons in the CC bond into the empty *d*-orbitals or bands of metal and back-donation of filled *d*-electrons from the metal into the π^* antibonding orbital of the CC bond, which can also be called the *d*-π^* feedback mechanism, which is very similar to the *d*-σ^* feedback mechanism for H_2 activation on the metal

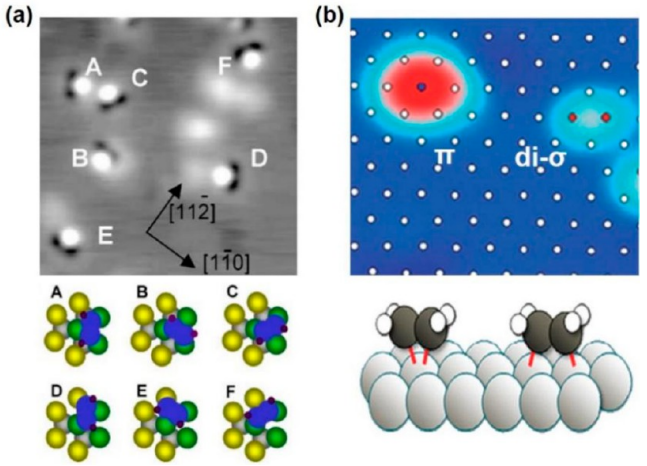

Figure 2. Scanning tunneling microscope images and the related theoretical models for (a) C_2H_2 adsorption on Pd(111) and (b) C_2H_4 adsorption on Pt(111). [Panel (a) has been reproduced with permission from ref 49. Copyright 2005, Elsevier. Panel (b) has been reproduced with permission from ref 50. Copyright 2011, American Chemical Society, Washington, DC.]

catalyst surface. C_2H_2/C_2H_4 undergoes a rehybridization process from the sp^2 state to somewhere between sp^2 and sp^3 due to the donation and back-donation of electrons, which is one of the origins of C−H bond bending. Thanks to the high sensitivity of the stretching frequency to the hybridized state of the CC bond, it is then possible to determine and testify the hybridization state of the adsorbed molecule experimentally by measuring the vibrational frequency corresponding to the ν_2(CC) stretching mode. In the case of gaseous C_2H_2, C_2H_4, and C_2H_6, which represent the sp, sp^2, and sp^3 hybridized systems, ν(CC) is measured to be 1974, 1623, and 993 cm^{-1}, respectively.[52,55] The related ν(CC) for C_2H_4 adsorption on transition-metal surfaces are shown in Table 1.[52,56,57]

Table 1. ν(CC) for C_2H_4 Adsorption on Surfaces of Different Transition Metals[a]

	ν(CC) [cm^{-1}]	
transition metal	111	100
Pd	1502	1135
Pt	980, 1230	984
Ni	1200, 1390, 1385	1130
Zeise's salt[b]	1515	

[a]Data taken from refs 56−58. [b]Zeise's salt can be represented by the formula $K[Pt(Cl)_2(CH_2{=}CH_2)]$.

The ν(CC) of C_2H_4 is strongly dependent on the species of transition metal on (111) with a vibration wavelength much longer on Pd(111) than that on Pt(111) and Ni(111). It indicates that C_2H_4 seems to rehybridize closer to the sp^3 state on Pt(111) and Ni(111), while there is much less distortion on Pd(111). However, the ν(CC) of C_2H_4 is similar on (100) of the above three metals, implying a rehybridization of similar extent.

Apart from a series of spectroscopic methods, theoretical calculation and scanning tunneling microscopy (STM) will give more visual information for C_2H_2/C_2H_4 adsorption.[49−51,59,60] Rutger et al. has summarized the adsorption energies and configurations of C_2H_2, C_2H_4, and the related

https://doi.org/10.1021/acscatal.2c05141
ACS Catal. 2023, 13, 974−1019

Table 2. Periodic DFT Calculated Binding Energies and Adsorption Modes for C_2H_x (x = 1−5) Species on Pd(111) at 0.25 Monolayer Coverage[61]

adsorbate	structural formula	mode	structure (figure)	adsorption site	binding energy [kJ mol^{-1}]
ethylene	$H_2C{=}CH_2$	π	3a	atop	−27
ethylene	$H_2C{=}CH_2$	di-σ	3b	bridge	−62
acetylene	$HC{\equiv}CH$	di-σ	3c	bridge	−136
acetylene	$HC{\equiv}CH$	$\eta^2\eta^2$(C,C)	3d	hollow	−168
ethyl	$H_3C{-}CH_2$	η^1(C)	3f	atop	−140
ethylidene	$H_3C{-}CH$	η^2(C)	3g	bridge	−334
ethylidyne	$H_3C{-}C$	η^3(C)	3h	hollow	−511
vinyl	$H_2C{=}CH$	$\eta^1\eta^2$(C,C)	3i	hollow	−254
vinylidene	$H_2C{=}C$	$\eta^1\eta^3$(C,C)	3j	hollow	−363
acetylidene	$HC{\equiv}C$	$\eta^1\eta^3$(C,C)	3k	hollow	−411
acetylidene	$HC{\equiv}C$	$\eta^2\eta^3$(C,C)	3h	hollow	−415
hydrogen	H	η^3	3l	hollow	−267

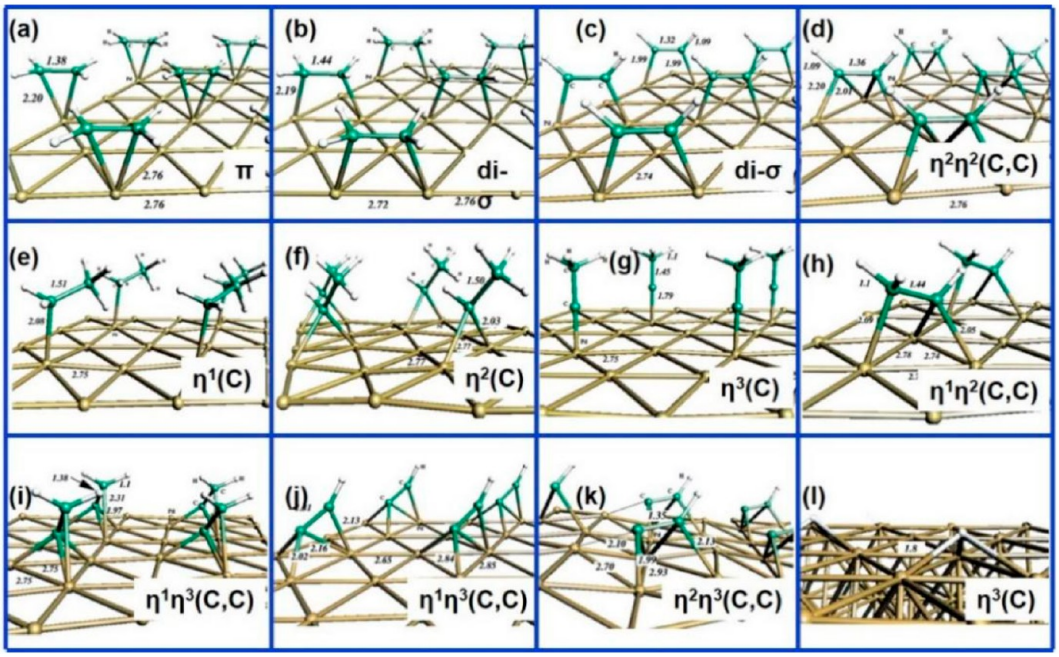

Figure 3. (a−l) The related adsorption structures of different modes for H and C_2H_x (x = 1−5) species on Pd(111) at 0.25 monolayer coverage. [Reproduced with permission from ref 61. Copyright 2002, American Chemical Society, Washington, DC.]

intermediates on Pd(111), as shown in Table 2 and Figure 3.[61] Generally, two relative stable adsorption modes exist for C_2H_2 and C_2H_4, respectively. The DFT calculation of C_2H_2 adsorption on Pd(111) has led to two main types of structures, named as $\eta^2\eta^2$(C,C) and di-σ, respectively, as shown in Figure 3, which was also confirmed by temperature-programmed desorption (TPD) results.[62] C_2H_2 in $\eta^2\eta^2$(C,C) mode locates on the 3-fold fcc hollow site with a σ-bonding of C=C to two adjacent metal atoms and a π-bonding to the third one in the vertical direction with a binding energy of −168 kJ/mol, which is higher than that in the less-stable di-σ mode (−136 kJ/mol) in which C=C involves two σ-bondings with two adjacent metal atoms at a bridge site. In contrast, the most favorable adsorption configuration for C_2H_4 on Pd(111) is the di-σ mode with a binding energy of only −62 kJ/mol, much smaller than that for C_2H_2. The calculated value is in good agreement with UHV-TPD experiments estimated as −59 kJ/mol.[57,63] The less-stable π-bound mode for C_2H_4 is close to half of the value of the di-σ mode energy at −30 kJ/mol. And these two adsorption modes are interswitchable.[50] Unlike C_2H_4 adsorbing in the di-σ mode, the hydrogen atoms and C≡C bond on C_2H_2 are not on the same vertical plane in $\eta^2\eta^2$(C,C) mode, which was confirmed by STM with a molecular tip, as seen in Figure 2.[49] As depicted schematically in Figure 2a, the center of the protrusion rests on a 3-fold hollow site and each depression is situated near a Pd atom. The topographic image of C_2H_2 has a mirror plane that is perpendicular to the Pd(111) surface in the $[1\bar{1}2]$ direction, suggesting that the CC bond is parallel to the $[\bar{1}10]$ direction and that the molecular orbital interacts with the d-orbitals of Pd atoms, which significantly contributes to the protruding portion of the adsorbed C_2H_2.

Acrolein is another typical probe molecule to study the adsorption behavior, because it contains more than one reducible and conjugated groups. And the competitive adsorption between C=C and C=O bonds or their intermediates will play a more important role to the selectivity control. According to the results from DFT calculation, there are up to nine possible adsorption modes for acrolein on different metal surfaces, as seen in Figure 4.[18] The specific

https://doi.org/10.1021/acscatal.2c05141
ACS Catal. 2023, 13, 974−1019

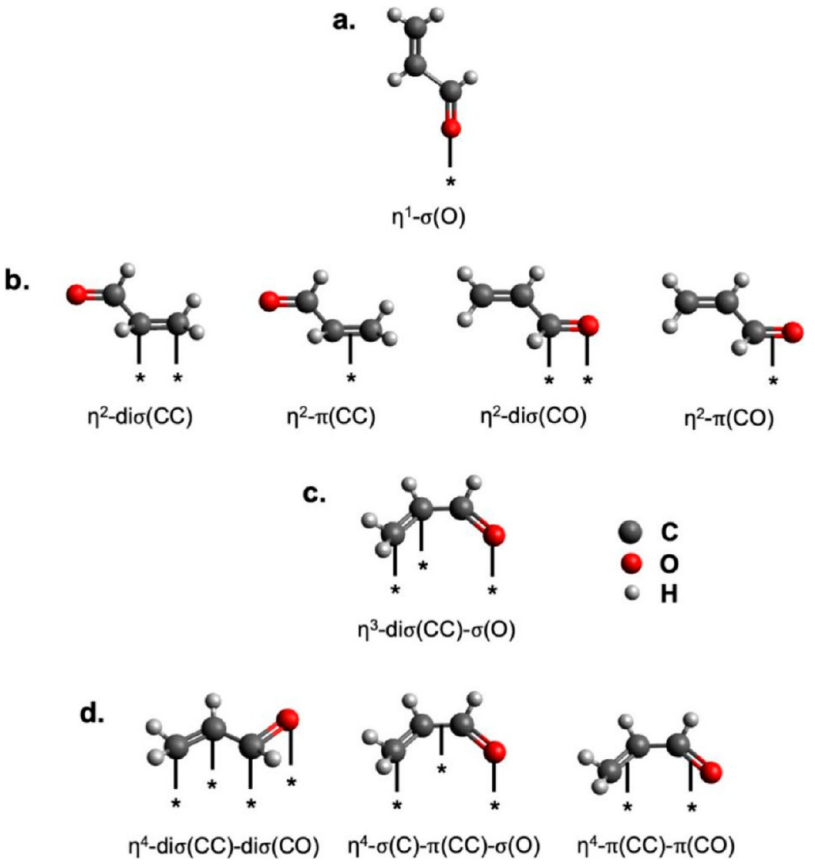

Figure 4. Possible adsorption modes for acrolein on metal surfaces: (a) η^1-mode (atop) via the carbonyl O; (b) η^2-modes via either the C═C or the C═O bond, as well as a metallocycle via the terminal atoms; (c) η^3-mode via the C=C bond and the carbonyl O; and (d) η^4-modes involving all backbone atoms. [Reproduced with permission from ref 18. Copyright 2020, American Chemical Society, Washington, DC.]

adsorption mode is closely related to the type of metal. On group 10 metals such as Pt, acrolein binds mainly via planar η^3 and η^4 configurations on Pt facets (Table 3), with C═C bond binding more strongly than C═O bond at the same binding mode of di-σ mode.[18] The adsorption mode changes to vertical η^1 configuration via the carbonyl O at the edge sites of Pt. The adsorption energy of acrolein is approximately −1.1 eV on Pt(111). The desired intermedite allyl alcohol shows essentially the similar adsorption strength as acrolein and will be further hydrogenated to *n*-propanol instead of desorption. Hence, the selectivity of allyl alcohol is thermodynamically controlled since the hydrogenation of C═C and C═O are both favorable. In the presence of aliphatic substituents at β-carbon, the adsorption of the C═C bond is then sterically weakened. Accordingly, the adsorption mode shifts from planar η^3 and η^4 configurations to a vertical η^1-σ(O) configuration (analogous to Figure 4a) at high coverage, which is favorable for the selective hydrogenation of C═O. What's more, unsaturated alcohols with a larger number of substituents or bulkier substituents show weaker adsorption, which is thereby beneficial for their desorption rather than over hydrogenation to corresponding saturated alcohols. The same trend holds on Pd and Ni. On group 11 metals (Au, Ag, Cu), since the activation of H_2 is limited due to the full occupation of the *d*-band, the selectivity of unsaturated alcohols turns to be kinetically controlled. Compared to that on group 10 metals, the adsorption of acrolein is also significantly weaker on Au and Ag, as evidenced by a transformation of adsorption from di-σ to predominantly π binding modes, as shown in Table 3. The adsorption of allyl alcohol remains similarly weak adsorption strength as acrolein. As a result, desorption of allyl alcohol is no longer the key factor, with regard to determining the selectivity. Another point that must be emphasized is that the hydrogenation of the C=O bond will change to be kinetically more favorable on Au and Ag facets with subsurface O.[64]

3. REACTION KINETICS FOR SELECTIVE HYDROGENATION

A kinetic approach is certainly valuable for a better mechanistic understanding of selective hydrogenation reactions, and furthermore favorable for rational catalyst design based on geometric and electronic modification.[65−70] The discussion that follows in this section will highlight several key aspects guarding the basic catalytic performance and enlightening some behaviors reflecting geometric and electronic effects.

Langmuir−Hinshelwood kinetics is most popular for metal catalysts in selective hydrogenation reactions, with a typical characteristic that both H_2 and reactants first undergo a chemisorption on the catalyst surface.[71] Particularly, this mechanism is also called the Horiuti−Polanyi mechanism, where H_2 dissociates first and performs the sequential addition of H atoms to the adsorbed hydrocarbon.[72,73] Assuming that the rate-determining step for a selective hydrogenation reaction between H_2 and the reactant is controlled by the surface addition procedure of the two adsorption species H_{ads} and R_{ads}, whose concentrations on catalyst surface can be

https://doi.org/10.1021/acscatal.2c05141
ACS Catal. 2023, 13, 974−1019

Table 3. Statistics of Stable Adsorption Modes of Acrolein in Figure 4 on Metal Surfaces of Group 10 vs 11[a,b]

host	promoter	facet	adsorption mode
Pt		(111)	η^2-diσ(CC)
Pt		(111)	η^3-diσ(CC)-σ(O)
Pt		(110)	η^4-diσ(CC)-diσ(CO)
Pt		(211)	η^2-diσ(CC)
Pt		(211)	η^4-σ(C)-π(CC)-σ(O)
Pt	Sn	(111)	η^2-σ(C_4)-σ(O)-OSn
Pt	Sn	(111)	η^3-diσ(CC)-σ(O)-OSn
Pt	Fe	(111)	η^3-diσ(CC)-σ(O)-OFe
Pt	Fe_{sub}	(111)	η^3-diσ(CC)-σ(O)
Pt	Co ML	(111)	η^4-diσ(CC)-diσ(CO)
Pt	Co_{sub} ML	(111)	η^2-diσ(CC)
Pt	Ni ML	(111)	η^4-diσ(CC)-diσ(CO)
Pt	Ni_{sub} ML	(111)	η^4-diσ(CC)-diσ(CO)
Pt	Cu ML	(111)	η^4-diσ(CC)-diσ(CO)
Pt	Cu_{sub} ML	(111)	η^2-diσ(CC)
Pd		(111)	η^2-diσ(CC)
Ni		(111)	η^4-diσ(CC)-diσ(CO)
Au		(110)	η^2-π(CC)
Au		(211)	η^2-diσ(CO)
Au		(211)	η^2-π(CC)
Au	In	(110)	η^2-diσ(CO)-OIn
Ag		(111)	η^2-π(CC)
Ag		(110)	η^2-π(CC)+η^1-σ(O)
Ag		(110)	η^4-π(CC)-π(CO)
Ag		(100)	η^2-diσ(CC)
Ag		(100)	η^4-π(CC)-π(CO)
Ag		(211)	η^4-π(CC)-π(CO)
Ag		(221)	η^4-π(CC)-π(CO)
Ag	Pd	(111)	η^2-π(CC)-Pd
Ag	O_{sub}		η^4-π(CC)-π(CO)

[a]Cases with a monolayer of promoter on a given metal are indicated as "ML". All promoters interacting with the adsorbate reside in the surface layer, unless specified with a subscript "sub" for the subsurface layer. [b]Data taken from ref 18.

expressed by θ_H and θ_R, the rate equation in Langmuir–Hinshelwood kinetics can then be written as

$$r_R = -\frac{dC_R}{dt} = k_T\theta_H\theta_R = \frac{k_T b_H P_{H_2} b_R P_R}{(1 + b_H P_{H_2} + b_R P_R)^2} \quad (3\text{-}1)$$

Figure 5 shows a plot of the rate equation (eq 3-1), as a function of H_2 pressure (P_{H_2}). Meanwhile the pressure of the reactant (P_R) is kept constant.[71] Apparently, the reaction rate encounters a maximum along with P_H. At the point of maximum, $\theta_H = \theta_R$. The effect of P_R on the reaction rate can also be drawn in Figure 5, as shown by the dashed lines. The curve of r_R moves to the right, together with a decrease in value at lower P_H and then an increase at higher P_{H_2}. Besides, the rate for hydrogenation is basically proportional to P_{H_2} at lower P_{H_2} conditions, while it becomes inversely proportional to P_R when P_H goes higher.

If both H_2 and the reactant adsorbed weakly on catalyst surface, then $1 \gg \theta_H + \theta_R$, and so eq 3-1 can be simplified to a second-order rate expression:

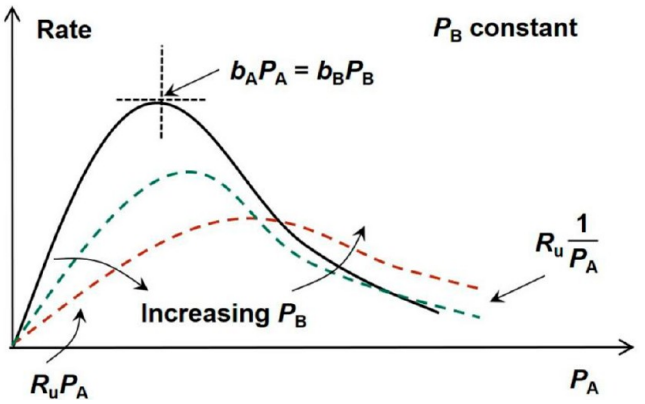

Figure 5. Trends for reaction rate of the Langmuir–Hinshelwood model for a bimolecular reaction of A and B over a catalyst as a function of P_A with P_B held constant, showing the effect of increasing the value of P_B. [Reproduced with permission from ref 71. Copyright 2019, Elsevier.]

$$r_R = -\frac{dC_R}{dt} = k'_T P_{H_2} P_R \quad (3\text{-}2)$$

In this case, the reaction rate is proportional to P_{H_2} and P_R simultaneously with a reaction order within 0–1, respectively.

If the reactant binds strongly while H_2 is relatively weakly adsorbed, then eq 3-2 reduces to

$$r_R = -\frac{dC_R}{dt} = \frac{k''_T P_{H_2}}{P_R} \quad (3\text{-}3)$$

On this condition, the reactant actually serves as a poison to the catalyst or hydrogenation reactions in that the reaction rate is inversely proportional to P_R in mathematics with a reaction order within −1–0.

When the products also adsorbed on the surface of the catalyst to any appreciable extent, the kinetics equation gets even more complicated. The detailed deduction and discussion are certainly beyond the scope of this Review, but we still want to give a brief description. A typical kinetics example is the selective hydrogenation of acetylene over supported palladium under tail-end conditions. As reported by Schuurman et al., power law expressions for the rates were written as follows:[68]

$$-r_{C_2H_2} = k_1 P_{C_2H_2}^{\alpha_1} P_{H_2}^{\beta_1} P_{C_2H_4}^{\gamma_1} \quad (3\text{-}4)$$

$$r_{C_2H_6} = k_2 P_{C_2H_2}^{\alpha_2} P_{H_2}^{\beta_2} P_{C_2H_4}^{\gamma_2} \quad (3\text{-}5)$$

The deduced reaction orders are given in Table 4;[68] the experimental values at 51 and 62 °C are given in Table 5 accordingly, after numerically integration of the rate equations and regression analysis.[68] Apparently, C_2H_2 serves as a poison for both C_2H_2 hydrogenation and C_2H_6 formation on supported Pd catalysts due to the large negative reaction order. As a result, though C_2H_2 decreases the reactivity, the selectivity to C_2H_4 is improved due to the repulsion of relative weak adsorbed intermediates as C_2H_4. C_2H_4 also plays a soft poison for C_2H_2 hydrogenation with a small negative reaction order, but is conducive to the overhydrogenation. Somehow, the reaction order for H_2 activation is overestimated with a value at ∼1.5, which was usually measured to be ∼1 in most cases.

When the reactant interacts directly from the gas phase with dissociative H_2 on the catalyst surface in a bimolecular

https://doi.org/10.1021/acscatal.2c05141
ACS Catal. 2023, 13, 974–1019

Table 4. Reaction orders corresponding to the derived rate-equations.[68]

	RC_2H_2			RC_2H_6		
reaction order	C_2H_2	H_2	C_2H_4	C_2H_2	H_2	C_2H_4
dependence on coverage	$1-2\theta C_2H_2$	$1-\theta H_2$	$-2\theta C_2H_4$	$-2\theta C_2H_2$	$1-\theta H_2$	$1-2\theta C_2H_4$
min−max	−1−1	0−1	−2−0	−2−0	0−1	−1−1

Table 5. Estimated Values of the Reaction Orders with Their 95% Confidence Intervals[a]

	RC_2H_2			RC_2H_6		
temperature [°C]	$\alpha_1(C_2H_2)$	$\beta_1(H_2)$	$\gamma_1(C_2H_4)$	$\alpha_2(C_2H_2)$	$\beta_2(H_2)$	$\gamma_2(C_2H_4)$
51	−0.88 ± 0.09	1.46 ± 0.16	−0.13 ± 0.07	−1.00 ± 0.20	1.42 ± 0.70	1.09 ± 0.50
62	−0.93 ± 0.07	1.49 ± 0.34	−0.19 ± 0.04	−1.56 ± 0.3	1.69 ± 0.88	0.30 ± 0.15

[a]Data taken from ref 68.

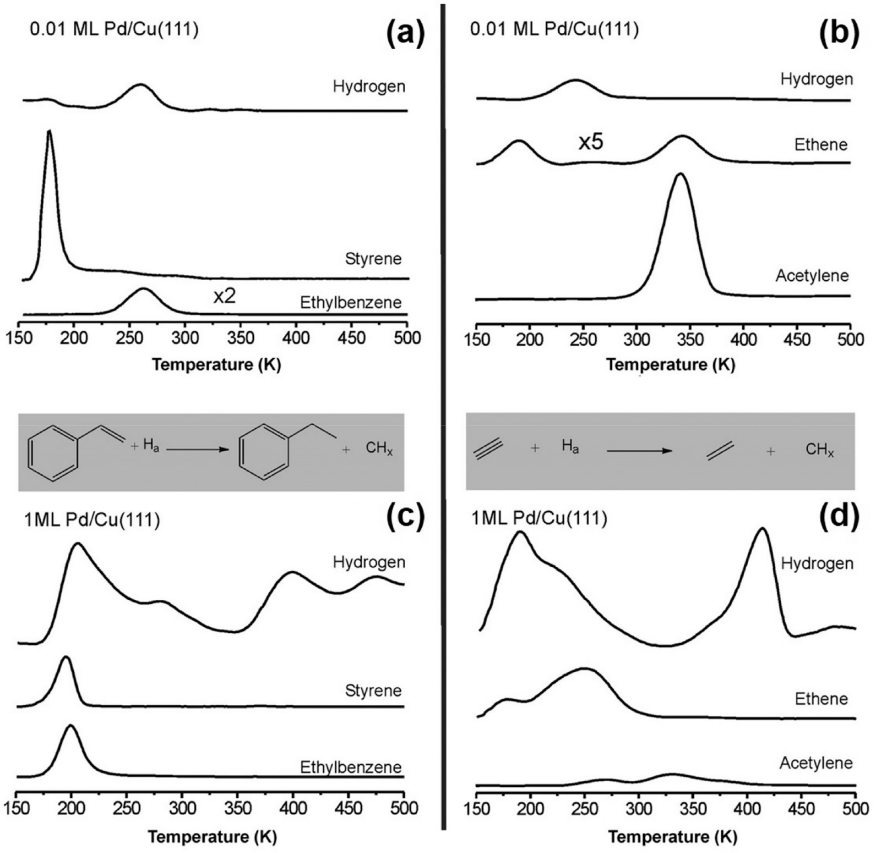

Figure 6. Representative TPR data showing the increase in selectivity obtained by atomically dispersing Pd atoms in Cu versus the extensive decomposition of the reactants on a 1-ML Pd layer: (a) styrene hydrogenation on 0.01-ML Pd/Cu(111) alloy, (b) acetylene hydrogenation on 0.01-ML Pd/Cu(111) alloy surface, (c) styrene hydrogenation on 1-ML Pd/Cu(111) alloy, and (d) acetylene hydrogenation on 1-ML Pd/Cu(111). In all cases, near-saturation H_a was deposited at 85 K followed by 0.5 ML of the hydrocarbon at 150 K. [Reproduced with permission from ref 84. Copyright 2012, AAAS.]

reaction, then reaction kinetics changes from the Langmuir−Hinshelwood mechanism to the Eley−Rideal mechanism, which was first postulated by Eley and Rideal in 1939 for ethylene hydrogenation reactions on metal catalysts.[74] Generally, this mechanism requires that the reactants interact with fully covered dissociative H adatoms on the surface from the gas phase to form the desired product, which can be determined by either the nature of the reactants themselves or the reaction conditions.[75] The rate equation is expressed as

$$r_R = -\frac{dP_R}{dt} = k_T P_R \theta_H = \frac{k_T P_R b_H P_{H_2}}{1 + b_H P_{H_2}} \quad (3\text{-}6)$$

The kinetic expression is similar to the case where both H_2 and the reactant adsorbed weakly on the catalyst surface in the Langmuir−Hinshelwood mechanism. However, the reaction order for P_H is considered to be a much lower positive value.

It can be seen that the activation of H_2 is always essential for most hydrogenation reactions, since the reaction order for H_2 participation often remains positive. However, the dissociation of H_2 on transition-metal surfaces is calculated to be nearly a barrier-free process, which is also confirmed by both experiments as H-D exchange, TPD and STM, and theoretical calculations.[75−79] Considering the fact that the optimal catalytic performance is confined by the ratio of θ_H and θ_R,

https://doi.org/10.1021/acscatal.2c05141
ACS Catal. 2023, 13, 974−1019

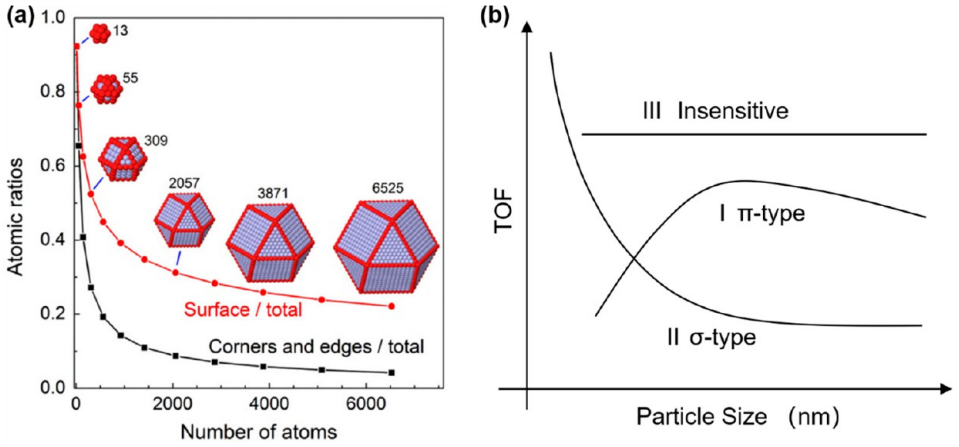

Figure 7. (a) The distributions of surface metal sites and undercoordinated sites, along with the particle size. (b) Three types of structure sensitivity−particle size relationship plotted as turnover number (TOF) versus particle size. [Panel (a) has been reproduced with permission from ref 98. Copyright 2015, Elsevier. Panel (b) has been reproduced with permission from ref 99. Copyright 1989, Elsevier.]

the factors determine the reaction order of H_2 for hydrogenation originate from the competitive chemisorption between H_2 and the reactant. In other words, the modification of the ratio of θ_H and θ_R is an important direction or aspect for catalyst optimization based on electronic and geometric effects, which has always been overlook and unreasonably interpreted for researchers. And, of course, the selectivity for hydrogenation of multireducible groups can be controlled by modulating the coverage ratio of these multireducible groups in theory. Another noteworthy situation, which is very likely to be neglected, is that the coverage and adsorption modes of adsorbed reactants should not vary in a broad range when a dozen of reaction temperatures are chosen to estimate the apparent energy barriers. Otherwise, the value will be underestimated, compared to the normal one. This is probably the cause for an obviously small activation energy (~30 kJ/mol) for C_2H_2 selective hydrogenation and a distinct product distribution for the hydrodeoxygenation of phenolic compounds operating at relatively high temperatures.[80−83] One is clear for the common sense that a notable reaction rate can be achieved with activation energies of this magnitude at room temperature. One possible reason for this is that the chosen temperature range for apparent energy barrier estimation or biomass upgrading is close to or beyond the desorption temperatures of the reactants, which results in sharp changes in coverage, production distribution, or even (sometimes) the hydrogenation mechanism (e.g., from the Langmuir−Hinshelwood mechanism to the Eley−Rideal mechanism).[72−74] As seen in Figure 6, the desorption of ethylbenzene and acetylene is complete at 300 and 375 K, respectively, which means that the coverage of the reactants will change dramatically during hydrogenation around those temperatures.[84] This phenomenon for kinetics estimation is often accompanied by the compensation effect, where the reaction rate constant and activation energy unreasonably change synchronously.[85−87] Aware of this, the insight to the electronic and geometric effects on catalyst optimization would be more clear.

4. THE GEOMETRIC AND ELECTRONIC EFFECTS FOR SELECTIVE HYDROGENATION

One must be aware of the multidimensional aspects and multiple scales that contribute to the observed catalytic performance. Supported metal catalysts for hydrogenation often involve the porosity for mass transportation and active site location on the micrometer or even millimeter to nanometer scale,[88] and encounter macroscopic phase and morphological transformations and microscopic surface reconstruction, active component aggregation, and leaching with a long time range from years to submilliseconds.[89−92] Besides, the electronic and geometric effects derived from the size of metal particle, alloying, support effects, self-modification from adsorbed reactants and/or intermediates, etc., are also responsible for the catalytic performance.[93] Since metal always serves as the key component for hydrogenation catalyst, we will focus on the factors related to metal component affecting the catalytic performance, i.e., the electronic and geometric effects in this section. The electronic and geometric effects of the metal particles reflect the structural sensitivity of one certain reaction, which is often shown in the form of particle size effect in metal catalysis.[2,48,94−97] The origin of these effects is usually explained by the preferential cleavage or activation of a certain bond on highly under-coordinated or defect sites. For Wulff-constructed nanoparticles of various sizes, as shown in Figure 7a, small nanoparticles own much more surface atomic ratios than the large ones.[98] And the proportion of higher undercoordinated (steps or edges) sites in these surface atoms also dominates for small particles. Unexpectedly, the site preferences can give rise to different classes of structure−sensitivity trends based on the bonding types. Figure 7b shows three types of typically observed structural sensitivity in TOF, as summarized by Che and Bennett:[99] an exponential decrease in activity with increased particle size, called "σ-type sensitivity"; an optimal particle size for π-type sensitivity; and a horizontal line for structure-insensitive cases.[100−102] The corresponding typical reactions explored in the early stage involve steam methane reforming (σ-type),[103−108] carbon dioxide methanation (π-type),[109−111] ethylene hydrogenation (insensitive),[112,113] etc.

steam methane reforming

$$CH_4 + H_2O \rightarrow CO + 3H_2 \qquad (\sigma\text{-type})$$

carbon dioxide methanation

$$CO_2 + 4H_2 \rightarrow CH_4 + 2H_2O \qquad (\pi\text{-type})$$

https://doi.org/10.1021/acscatal.2c05141
ACS Catal. 2023, 13, 974−1019

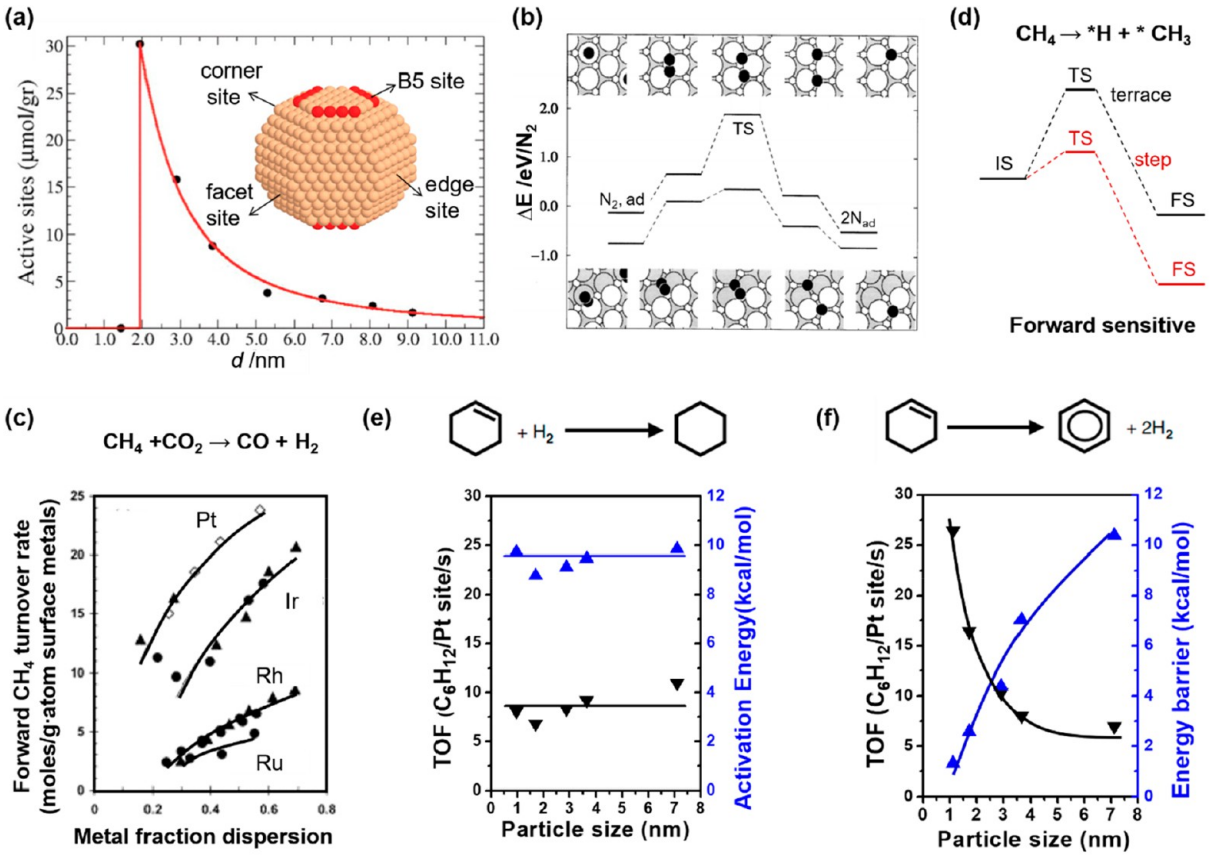

Figure 8. (a) Model for supported Ru particle with various types of sites. Population of B5 sites, as a function of particle diameter. B5 sites are shown in red. (b) Reaction path and energies for N_2 dissociation on Ru (0001) terraces (top) and steps (bottom). (c) Forward CH_4 turnover rates for CO_2 reforming of CH_4, as a function of metal dispersion on various supports ((▲) ZrO_2, (●) γ-Al_2O_3, (◇) ZrO_2−CeO_2 as supports). (d) Scheme of the activation energy−reaction energy relationships for CH_4 activation, as a function of structure for sensitivity analysis. Particle size effects for cyclohexene (e) hydrogenation and (f) dehydrogenation on supported Pt catalyst. [Panel (a) has been reproduced with permission from ref 121. Copyright 2005, AAAS. Panel (b) has been reproduced with permission from ref 124. Copyright 1999, American Physical Society. Panel (c) has been reproduced with permission from ref 105. Copyright 2004, American Chemical Society, Washington, DC. Panles (d)-(F) have been reproduced with permission from ref 114. Copyright 2018, American Chemical Society, Washington, DC.]

ethylene hydrogenation

$$C_2H_4 + H_2 \rightarrow C_2H_6 \qquad \text{(insensitive)}$$

This classification of structure insensitivity is very illuminating in a sense.

Consequently, we will discuss the geometric and electronic effects, beginning with the discussion of the origin of the different structural sensitivities for both activity and selectivity in selective hydrogenation system with multiple reducible functional groups in this section. Note that there have been several reviews giving thorough discussions on the particle size effect.[2,48,94−97,114−116] We will not simply repeat it here and will only try to distinguish the specific phenotype under a concrete reaction system when involved instead. However, it is challenging to separate these two impacts, because they get inherently entangled.[93,117−119] This section concentrates on a few potential scenarios and causes for the two impacts rather than providing a comprehensive display of the associated published results, so that readers can have a greater grasp of this topic. We will strive to choose and offer certain classic research results that are more accurate in interpretation, to minimize misleading.

4.1. The Geometric Effects for Selective Hydrogenation. The geometric effects of catalysts can be expressed in various forms, which can be summarized as surface coordination or steric effect, spatial structure confinement and matching effect, active site synergism effect, etc. In this Review, we will mainly focus on the first two effects, and they will be discussed separately in the following.

4.1.1. Surface Coordination or Steric Effect. For the hydrogenation reaction, the surface coordination structure of active metal is an important factor to which researchers attach great importance. It is the most important index to measure the sensitivity of a reaction to a geometric structure. Generally, researchers are used to study the influence of the size of metal particles on the reaction performance, which is commonly known as the size effect. The theoretical basis is the Wulff construction rule.[120] As shown in Figure 8a, there are many active sites with different coordination forms on the surface of a nanoparticle, such as facet sites with different Miller indices and various undercoordinated edge and corner sites (including defect sites).[121] The orbital saturation on the active sites with different degrees of coordination is different, so the reaction performance also varies. Meanwhile, different coordination structures will also affect the Coulomb repulsion between the adsorbed species on the surface, thus changing the potential energy surface of the reaction and causing different geometric structure sensitivity. When the size of the metal nanoparticles

https://doi.org/10.1021/acscatal.2c05141
ACS Catal. 2023, 13, 974−1019

decreases gradually, as shown in Figure 7a, the proportion of undercoordinated sites increases gradually and shows a nonlinear growth trend.[98] The smaller the particle size, the faster the growth rate. The types of main active sites on the surface of metal nanoparticles with a particle diameter of ∼1 nm are completely opposite to those of particles with a diameter of >5 nm. This is the reason why the reported results show that the relationship between the reaction performance and the size of nanoparticles is nonlinear, as illustrated in Figure 7b.

The bond nature of the activated substrate dictates which type of surface atom rearrangement offers the lowest activation energy.[102] This novel insight provides the basis for a classification of structure sensitive and insensitive reactions. Three phenotypes of structural sensitivity have been classified according to the type of chemical bonds to be activated, as shown earlier in Figure 7b. Specifically, the reactions involving the cleavage or formation of molecular π bonds, such as C═C, C═O, N≡N, etc., must be distinguished with the reactions involving σ-bond-activated reactions (C−H, O−H, N−H, C−X (where X = F, Cl, Br, I)). The cleavage of a π-bond requires a unique reaction center called B5 on an FCC surface or C7 on a BCC crystal surface composed of multiple metal atoms of step and edge sites, but there is no such active center on transition-metal particles of <2 nm, as shown in Figure 8a. This is called class I surface sensitivity. When the particle size is below the critical size, the reaction rate will decrease sharply. Hardeveld and Monfoort made a crucial early contribution where they discovered unique step-edge type sites (B5 sites, Figure 8a) on particles that had an incomplete octahedral structure.[121,122] They determined a critical size of ∼2 nm to crystals with octahedral shapes, as seen in Figure 8a, which cannot accommodate the B5 sites with smaller size, and proposed B5 sites to be active for N_2 activation. Surface science studies[123] and computational studies[124,125] also confirmed the unique activity of such sites for the dissociation of NO and N_2 at the step edges of Ru(0001), as shown in Figure 8b. The maximum in the rate of ammonia synthesis catalyzed by dispersed Ru particles was explained based on the requirement for the B5 sites.[121] Special activity for the same reaction on unique C7 sites of the Fe(111) was also found by surface science studies, which share a very similar structure to the B5 site. Later, Hammer and Nørskov noted that such step-edge structure dependence of dissociative adsorption was quite general for the cleavage of the π-bonds in diatomic molecules as CO, N_2, O_2, or NO.[126] For example, the cleavage of CO at B5 sites required an activation energy of only 65 kJ/mol on the corrugated $(11\bar{2}1)$ surface of Ru, compared to 210 kJ/mol on the Ru(0001) terrace.[127,128] Similar results were also found on Co surfaces.[129]

The activation of the σ chemical bonds on a single metal atom shows obviously different size relationships. In this case, the dependence of the reaction barrier on the coordination unsaturated surface atom is large in the forward direction, but the activation energy of the reverse recombination reaction does not change. The atoms on the edge and corner sites of particles have a great impact on the dissociation of σ-bonds (C−H, etc). This is called class II surface sensitivity, in which the rate will increase as the particle size shrinks. Hydrogenolysis of alkanes with the cleavage of C−C bonds are prototype reactions that increase in rate with shrunken particle size.[100,130] Taiet al. reported an enhanced activity of 3 nm Pd particles, compared to that on facet atoms.[131] C−H bond activation of methane also showed promotion in normalized activity with decreased particle size, as shown in Figure 8c.[105,132] Somorjai has also shown the tremendous impact that various levels of coordinative unsaturation of catalyst surface atoms have on hydrocarbon conversion processes.[133] Compared with isomerization to *n*-butane, the surface with a high proportion of kink sites showed the highest hydrogenolysis selectivity to isobutane. Isomerization is preferred for less-reactive terraces with atoms of higher coordination. On such surfaces, the rate for C−H bond activation is reduced and C−C bonds remain less accessible accordingly for bond cleavage. Calculations exhibited the large decrease in activation barrier of the cleavage of σ-type C−C bond from 173 kJ/mol on Pt(111) terrace to 102 kJ/mol along the (100) edge of stepped Pt(211).[134] It can be seen that the structural sensitivity of π and σ bond activation is very different. Since the activation of π-bond involves multiple atoms or ensemble sites, the structure of the transition state is closely related to the interacting atoms. Different transition-state configurations will then result from various active site topologies. Hence, no obvious BEP relationship can be expected on the active sites of different structures. Or, in other words, the effective BEP relationship is only limited to the active sites with similar topological structures. In contrast, as the σ bond activation only requires one metal atom, the structure of the nearby metal site merely influences the associated energy through Coulomb contact and has no impact on the transition-state structure. Therefore, the BEP relationship exists on sites of different structures. According to the bond energy decomposition analysis of C−H bond cleavage of CH_4 on Rh active site, the transition-state deformation energy of different active site structures is basically the same, which also confirms the conclusion that the transition-state structure is unchanged.[102] The key factor affecting the transition-state energy barrier is the interaction energy between the deformed molecule and the active site.[102] The interaction energy includes the Coulomb repulsion between the transition-state molecule and the active site. Obviously, the coordination structure of the active site is closely related to the repulsion interaction, which is the origin of coordination structure sensitivity for σ-bond activation, whereas the inverse reactions such as σ-bond formation (hydrogenation) usually exhibit behavior independent of particle size. This is called class III surface sensitivity. Despite the fact that, in theory, the third type of surface sensitivity demands that the TOF not vary when the metal particle size changes. In reality, the only circumstance where the specific activity or TOF change is no more than a factor of 2 when the dispersion of the active component changes in the order of magnitude is generally classified as the third type of surface sensitivity, because the electronic effect will be accompanied by the change of the metal particle size at the same time, along with the experimental error.[101] A thorough analysis of the hydrogenation of cyclopropane on a platinum catalyst showed that the specific activity was unrelated to the dispersion of platinum. On highly dispersed samples, only a 2-fold variation in specific activity was seen, whereas the platinum surface area varied by more than 4 orders of magnitude.[135] For a long list of reactions, including hydrogen−deuterium exchange, hydrogenation of nitrobenzene, 1-hexene, cyclohexene, benzene, and allyl alcohol, dehydrogenation of cyclohexane and isopropanol, and hydrogenolysis of cyclopentane, this conclusion was successful generalized.[99−101] Interestingly, class II and class III structural insensitivity are complementary. This is

https://doi.org/10.1021/acscatal.2c05141
ACS Catal. 2023, 13, 974−1019

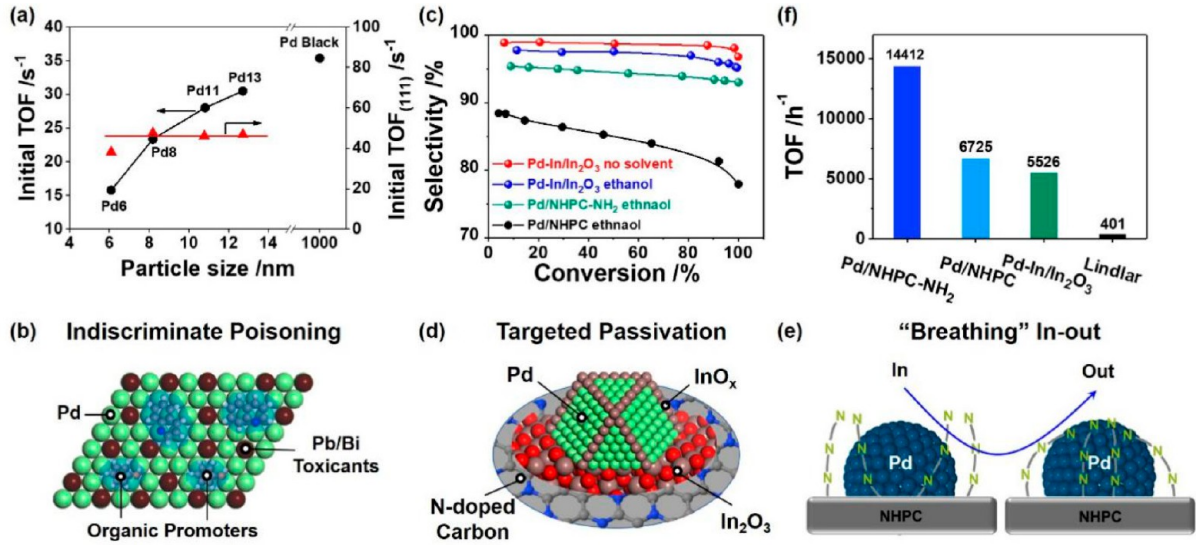

Figure 9. (a) Size dependence of TOF calculated per total number of surface atoms (black solid circle, left axis) and per the number of C^3_9 atoms of fcc cuboctahedron max-B5 crystal (red solid triangle, right axis) in MBY hydrogenation. (b) Model for commercial Lindlar catalyst. (c) Conversion−selectivity curves for MBY hydrogenation. (d) Model for targeted passivation. (e) Model for "breathing" catalyst. (f) Activity comparison of the above catalysts. [Panel (a) has been reproduced with permission from ref 146. Copyright 2007, Elsevier. Panel (b) has been reproduced with permission from ref 5. Copyright 2022, Tsinghua University Press. Panels (c), (e), and (f) have been reproduced with permission from refs 149 (Copyright 2019, Royal Society of Chemistry, London) and 150 (Copyright 2021, American Chemical Society, Washington, DC).]

determined by the microscopic reversibility of the reaction. The BEP relationship of the forward reaction of σ-bond activation was determined to be

$$\delta E_{af} = \alpha \delta E_{rf} \qquad (0 < \alpha < 1) \tag{4-1}$$

The corresponding BEP relationship of the reverse reaction process for σ bond formation is

$$\delta E_{ab} = -(1 - \alpha)\delta E_{rb} \qquad (0 < \alpha < 1) \tag{4-2}$$

in which δE_{af} and δE_{ab} are the change in the activation energy, and δE_{rf} and δE_{rb} the change in reaction energy of a forward and backward elementary reaction step, respectively.

It can be seen that, when the α value is close to 1, the activation energy for the forward reaction E_{af} is very sensitive to the reaction energy E_{rf}, which indicates structure sensitivity. At the same time, the absolute value of the slope of its reverse reaction process $-(1 - \alpha)$ is small and insensitive to structure. An example is the activation of CH_4 (structure-sensitive), and its reverse reaction (structure-insensitive).[128,136−139] As illustrated in Figure 8d, the cleavage energy barrier of a C−H bond is closely related with the dissociation energy, so this process can be structure-sensitive. However, the barrier for its reverse process is almost independent of the formation energy and can be structure-insensitive. The value of the BEP parameter α for the forward dissociation reaction is usually 0.7−0.9, implying a near complete cleavage of the molecular bond in the transition state.[136,140] Another example very familiar to researchers is that hydrogenation of cyclohexene to cyclohexane was well-known to be structure-insensitive, while the reverse process dehydrogenation of cyclohexane to benzene was structure-sensitive with class II type behavior, as shown in Figures 8e and 8f.[114] Similar BEP plots have been produced for CO and NO by the group of Hafner and the group of Liu and Hu.[141−144] It should be emphasized that the above discussion on the processes of π- or σ-bond cleavage or formation is valid on the condition that they are the reaction rate control steps; otherwise, it will be misjudged. For instance, dichloromethane hydrodehalogenation corresponds to class III surface sensitivity while having an apparent C−X bond activation mechanism.[145] Most likely, this is because the phase that controls rate in the hydrogenation process is the creation of the C−H bond. The aforementioned analysis of structural sensitivity for different chemical bond types is quite instructive. However, it is clear the guidance for hydrogenation selectivity is inadequate because class III in this technique encompasses many structurally insensitive hydrogenation activities. It is challenging to distinguish since a variety of structural sensitivity mixes can happen when selective hydrogenation involves more than two reducible groups. Finding a better coordination structure sensitivity analysis method or classification approach is thus required to combine it with the earlier classification methods.

Here, we try to roughly classify the reaction mechanisms according to the characteristics of the conversion-selectivity curve, such as the tandem mechanism or the parallel mechanism. This analysis or classification method based on the characteristics of reaction mechanism will give researchers a different understanding. And the concept for catalyst design will also be changed. For example, the dependence of MBY semihydrogenation rate showed that TOF increased twice when the diameter of Pd particle enlarged from 6 nm to 13 nm (Figure 9a).[146] This indicates that Pd atoms on the surface of a larger particle are more active than those on a smaller particle on average. The TOF remained steady when further increasing the Pd particle size. As a result, a TOF of 30 s^{-1} on Pd catalyst with a particle size of 13 nm was determined, being very similar with palladium black with a particle size as large as 1 μm (TOF = 35 s^{-1}, as shown in Figure 9a). However, the dependence of TOF on the particle size disappears when specific active sites as facet sites on (111) surface are only taken into consideration. Since the only type of surface atoms increased almost twice by ratio with particle sizes ranging from 6 nm to 13 nm are the ones located on the (111) facets, the main active sites for MBY semihydrogenation should be facet sites. Similar

https://doi.org/10.1021/acscatal.2c05141
ACS Catal. 2023, 13, 974−1019

results were also found in 1,3-butadiene hydrogenation.[147] Since the hydrogenation of alkenes is structure-insensitive, the direct methods to improve the selectivity to alkenes is to prepare catalysts with large Pd particles and further poison the facet sites to a certain extent to inhibit the olefin hydrogenation side reaction as conventional Lindlar catalyst do, as shown in Figure 9b,[5] if one follows the analysis method of structure sensitivity proposed by Che, Bennett, and Boudart.[99,100] Although the Lindlar catalyst is recognized to be very successful in chemical industrial field, the pollution and low efficiency caused by the use of heavy metal and toxic additives (to Pd active sites) has inspired great enthusiasm of researchers to develop more efficient and environmentally friendly substitutes.[148]

In contrast, if we carefully analyze the conversion−selectivity curves for the semihydrogenation of alkynes from a kinetic point of view, four informative phenomena can be observed, as shown in Figure 9c.[149,150] The first one is that the initial selectivity can reach ∼98% on bare Pd particles. The second one is that the decline in selectivity is almost linear with the conversion before reaching the end of the reaction. The third one is that a sharp parabola-type decrease was triggered when the conversion was beyond ∼90%. The fourth one is that the slope of the linear relationship in the second one and the parabola-type decrease at the end of the reaction are closely related with the concentration of the substrate. The higher the concentrate of the substrate, more gentle the slope and decrease of the selectivity. The above things indicate that the hydrogenation process from C≡C to C−C bond is actually sequential rather than parallel and that the catalytic performance of coincident active sites for both C≡C and C═C hydrogenation can be tuned by the competitive adsorption between them, which means that only undercoordinated sites as edge and corner sites should be considered to improve the C═C selectivity, while facet sites should be left alone.

This apparently enlighten us to adopt different strategies to modify the structures of the catalyst. For example, the most direct strategy to suppress the side hydrogenation of C═C bond is to target the under-coordinated sites passively, as shown in Figure 9d.[149] Meanwhile, in order to retain the activity of the original catalyst as much as possible, the exposed facet sites should be optimized. According to the Wulff construction rule, the optimal particle size of Pd is ∼4−5 nm. With this strategy, the highest yield for MBY semihydrogenation on Pd−In/In_2O_3 exceeded 98% at 99% conversion under no solvent and organic adsorbate conditions with 12-fold higher activity (ethanol as a solvent) than that on commercial Lindlar catalyst. The undercoordinated Pd sites can also be blocked by surfactants like PVP and etc.[151] Alloying is also efficient with this strategy since inert alloying atoms would occupy the undercoordinated lattice sites and dilute the inner Pd sites to improve the atomic utilization.[152] Another way is to introduce a moderate competitive adsorption between the adsorption strength of C≡C and C═C bond. Then the formed C═C products can be pushed off the catalyst surface in time and meanwhile prevent its readsorption. Note that this competitive adsorption interaction should be quite reversible and flexible to match with the reaction frequency. A "breathing" Pd catalyst with amine-functionalized support is an impressive example for C≡C semihydrogenation, as shown in Figure 9e.[150] The highest selectivity for MBY semihydrogenation on Pd/NHPC-DETA-50 reached 98% at 99% conversion under no solvent condition with 36-fold higher activity (Figure 9f, ethanol as solvent) than that on commercial Lindlar catalyst. The selectivity for internal alkyne semihydrogenation can even exceed 99%, and the amines for grafting can also be tuned.

For selective hydrogenation of trace acetylene (∼100 ppm) in a large ethylene stream, it resembles the late stage of alkyne semihydrogenation in the liquid phase. Herein, its conversion−selectivity curve is similar to that of liquid-phase alkyne semihydrogenation overall. A special point is that substantial overhydrogenation of ethylene is easy to occur when acetylene is almost totally converted, leading to even negative ethylene selectivity on the conversion−selectivity curves.[153−155] This is because the residual trace acetylene cannot totally prevent ethylene from adhering to and hydrogenating on the catalyst surface. Because of the limited diffusion rate of low-concentration acetylene, the micro area on the surface of metal nanoparticles can easily consume acetylene and form a local microenvironment without any acetylene, thus causing a serious overhydrogenation side reaction. Therefore, in addition to avoiding the exposure of the edge and corner positions, the Pd active center must be diluted to eliminate the extreme imbalance of the gas concentration in the micro region as much as possible, such as alloying, surface poisoning, monatomization, etc.[153,155−162] At the same time, it is necessary to increase the reaction temperature to accelerate Brownian motion and suppress the polarization of acetylene concentration in the reaction micro region. In addition, because of the lack of passivation of inert groups such as alkyl groups at both ends of acetylene, the Pd ensemble will also cause severe polymerization of acetylene, which will not only reduce ethylene selectivity, but also poison the catalyst surface.[153,154,163−169] Therefore, this also requires dilution of Pd active sites. Duan et al. has found that the distance of adjacent Pd atoms can be identified as a structural descriptor for configuration matching in acetylene semihydrogenation against coupling.[170] However, simply diluting the Pd active site cannot fundamentally solve the problem of overhydrogenation. In order to further improve the selectivity, it is also necessary to make use of the difference in adsorption energy between alkynes and alkenes on the catalyst surface to weaken or even inhibit the adsorption of alkenes on the active center and ensure the effective adsorption and hydrogenation of alkynes.[170,171] At present, many excellent articles on the semihydrogenation of acetylene have been reported, but most of them attribute the high selectivity to the difference between the desorption energy of ethylene and the activation energy of further hydrogenation.[156,172] This explanation is one-sided. In fact, most of the catalysts still have considerable ethylene direct hydrogenation activity under these conditions.[155,173−176] Therefore, a more complete selectivity criterion needs further development.

It can be seen that the catalyst design concepts obtained by the structural sensitivity analysis method based on the chemical bond type and the reaction kinetics curve are completely different for selective hydrogenation. Obviously, the structural sensitivity analysis method based on the reaction kinetics curve is more effective for the regulation of selectivity. Another example of structure sensitive tandem selective hydrogenation reaction is phenol hydrogenation.[6] The reaction involves σ activation of O−H bond and hydrogenation of aromatic ring in the meantime. According to the structural sensitivity analysis of the chemical bond type, the activity of this reaction belongs to the combination of type I and type III

https://doi.org/10.1021/acscatal.2c05141
ACS Catal. 2023, 13, 974−1019

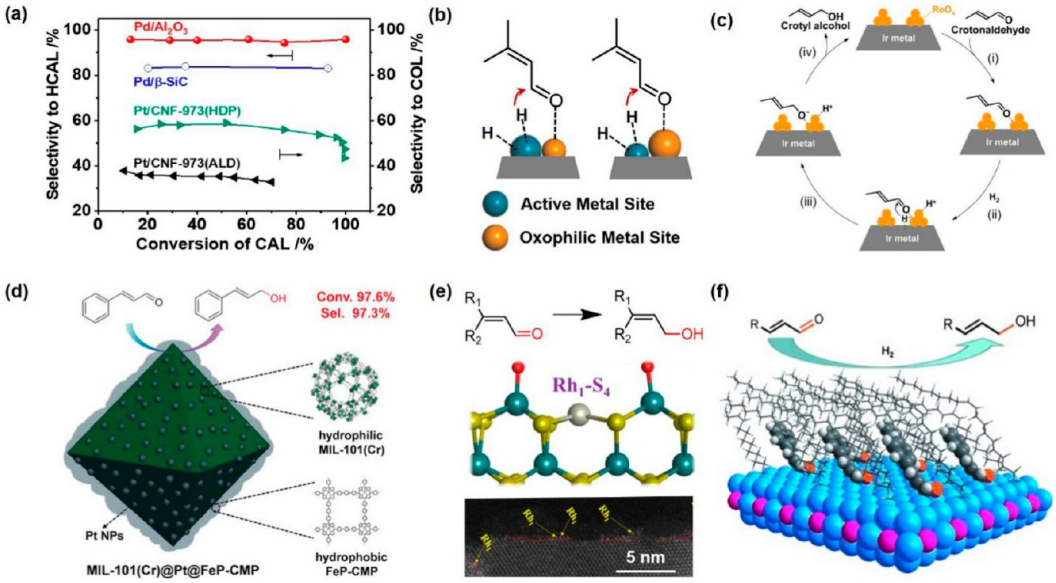

Figure 10. (a) Conversion−selectivity curves for cinnamaldehyde hydrogenation. Scheme for selective hydrogenation of unsaturated aldehydes with (b) oxyphilic adsorption site, with (c) the Lewis acid sites of oxide carriers, and with (d−f) the steric hindrance effect of space confinement. [Panel (a) has been reproduced with permission from ref 184, Copyright 2016, Royal Society of Chemistry, London. Panel (b) has been reproduced with permission from ref 187. Copyright 2008, Elsevier. Panel (c) has been reproduced with permission from ref 192. Copyright 2016, American Chemical Society, Washington, DC. Panel (d) has been reproduced with permission from ref 196. Copyright 2018, Wiley−VCH. Panel (e) has been reproduced with permission from ref 198. Copyright 2019, American Chemical Society, Washington, DC. Panel (f) has been reproduced with permission from ref 199. Copyright 2012, Wiley−VCH.]

sensitivity. It is predicted that the reaction generally has type I sensitivity, which was confirmed by the experimental results.[177,178] However, the structure sensitivity analysis cannot provide an effective solution for selective regulation. From the analysis of the conversion−selectivity curve, it can be concluded that the reaction follows a tandem mechanism, so the key to improve the selectivity is to block the further hydrogenation of cyclohexanone. Although the hydrogenation of carbonyl is geometrically sensitive, it can be performed at both planar and low coordination sites. It has been reported that the TOF for C═O hydrogenation of ketones increases with metal particle size since larger metal particles with a smaller proportion of undercoordinated surface sites would result in relatively weaker adsorbate−surface interaction and more balanced coverage between ketones and H_2 on a metal surface.[179] Unlike alkyne semihydrogenation, phenol cannot effectively inhibit the adsorption of cyclohexanone on the surface of metal sites. Therefore, the high selectivity of cyclohexanone cannot be achieved through the geometric effects such as the size and morphology modulation of metal particles or the selective deactivation of low coordination sites. In contrast, the use of an electronic effect has achieved good results. We will elaborate on this in the next section.

According to the characteristics of the conversion−selectivity curve, another type of selective hydrogenation reaction based on parallel reaction mechanism can be concluded, such as selective hydrogenation of α,β-unsaturated aldehydes and hydroformylation of olefins.[180−183] As shown in Figure 10a, the selectivity of the target product, enol, during selective hydrogenation of α,β-unsaturated aldehydes, hardly changes with the increase of conversion on the surface of commonly used Pd, Pt, and Ir catalysts.[181,184−187] It typically belongs to a parallel reaction mechanism. Based on the adsorption modes of unsaturated aldehydes introduced earlier, this selectivity change in the regular pattern is caused by the competitive adsorption and hydrogenation of C═C and C═O double bonds on the active site. Since the hydrogenation of the C═C bond in α,β-unsaturated aldehydes is more favorable in thermodynamics and kinetics, the metal active sites with different coordination structures do not have a high recognition ability for the hydrogenation of C═O double bond in the presence of the C═C bond.[188] In order to improve the hydrogenation selectivity of the C═O bond, we can only control the adsorption modes of reactants to inhibit the adsorption of the C═C bond on the active site. A common idea is to add an oxyphilic adsorption site and change the parallel adsorption mode to the vertical adsorption mode by strengthening the adsorption of C═O. For example, alloys are formed by adding transition metals (Co, Fe, Sn, Re, Zn, etc.) with strong oxygen affinity, as seen in Figure 10b, in which H_2 is activated by active metals as Pt, Ir, Ru, Ni, etc., and the C═O bond is activated by oxophilic metals.[18,46,188] After alloying, $Pt_{0.23}Co_{0.77}/C$ and $Cu_{0.08}Ni_{0.92}/SiO_2$ exhibited 100% and 96% selectivity to furfuryl alcohol at 100% conversion of furfural, outperforming the monometallic Pt/C and Ni/SiO_2.[189,190] 95% selectivity to cinnamyl alcohol at ∼100% conversion for cinnamaldehyde hydrogenation was also achieved on Pt_3Co/RGO-MW at 70 °C with a specific activity of 1428 h^{-1}.[185] Using the Lewis acid sites of oxide carriers to preferentially adsorb and activate C═O bonds, as shown in Figure 10c, such as SnO_x, FeO_x, ZnO_x, ReO_x, GaO_x, MoO_x, WO_x, NbO_x, CeO_x, etc., is also an effective method to regulate the adsorption mode.[18,46,188,191,192] By fabricating a cobalt-oxide-decorated Pt catalyst (Pt-CoO_x/C-LDH), the TOF for cinnamaldehyde conversion (15 084 h^{-1} at 80 °C) was significantly increased by 9.5 times, compared with that of the undecorated one. In addition, an unexpected yield of 99% to cinnamyl alcohol was also achieved.[193] A $YCo_XFe_{1-X}O_3$

https://doi.org/10.1021/acscatal.2c05141
ACS Catal. 2023, 13, 974−1019

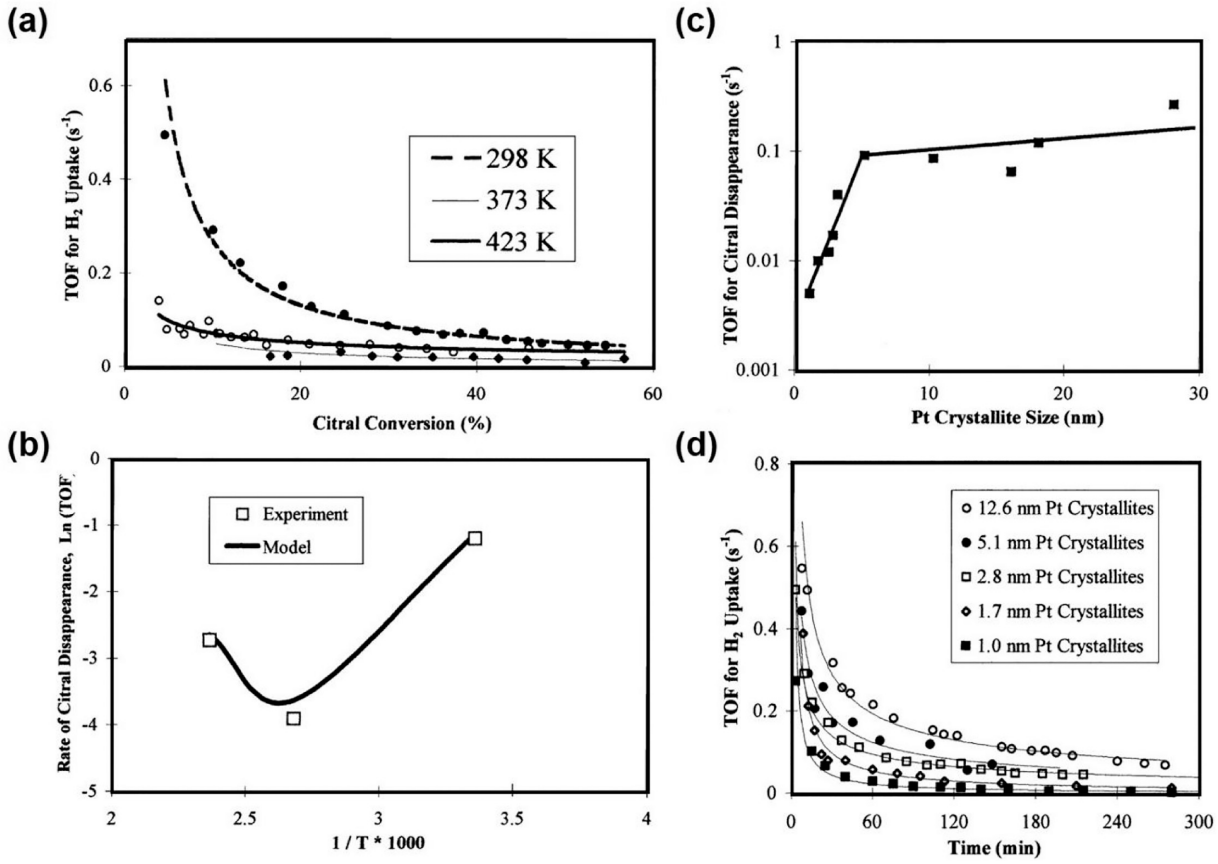

Figure 11. Effect of temperature on (a) H_2 uptake and (b) initial TOF for citral conversion during hydrogenation over Pt/SiO_2 at 298, 373, 423 K. Effect of average crystallite size on (c) TOF for citral conversion at 373 K and (d) TOF for H_2 uptake at 298 K. [Panels (a) and (b) have been reproduced with permission from ref 203. Copyright 2000, Elsevier. Panels (c) and (d) have been reproduced with permission from ref 212. Copyright 2000, Elsevier.]

perovskite oxide-supported Pt catalyst also reached 95% selectivity to cinnamyl alcohol at 99% conversion with a TOF of 15 163 h^{-1} at 90 °C.[194] Another idea is to utilize the steric hindrance effect of space confinement to force unsaturated aldehydes to adsorb vertically, but this method is usually more effective for long-chain unsaturated aldehydes. For example, when Pt nanoparticles were encapsulated into MOF channels, the catalyst showed excellent performance for a variety of unsaturated aldehydes, of which the highest yield of cinnamaldehyde was nearly 98%.[195] MIL-101@Pt@FeP-CMP sponge with a core−shell structure (FeP-CMPs: conjugated microporous and mesoporous polymers with iron(III) porphyrin, seen in Figure 10d) achieved 95% yield for cinnamyl alcohol at room temperature.[196] The hydrophobic porous shell structure promoted the adsorption of CAL around Pt NPs. Note that the steric hindrance effect of space confinement of the decorated porous metal oxides would also possibly benefit the selectivity for the semihydrogenation of alkynes due to the inhibition of the adsorption of C═C bonds if the pores are carefully controlled, e.g., by atomic layer deposition.[83,197] Apart from the traditional confinement with micropores, a pocketlike active site with HO−Mo−Rh_1−Mo−OH configuration was constructed on Rh_1/MoS_2, as seen in Figure 10e.[198] This enzyme-like catalyst exhibited amazing 100% yield to crotonol for selective crotonaldehyde hydrogenation. Besides introducing the steric effect through the space confinement of support, one can also achieve this goal through binding capping ligands on the surface of metal particles. For instance, the hydrogenation of cinnamaldehyde was completed in 9 h with a selectivity up to 95% to cinnamyl alcohol on oleylamine capped Pt_3Co nanoparticles (seen in Figure 10f) and the selectivity for cinnamyl alcohol still kept above 90% even when the reaction time was extended to 24 h.[199]

Returning to the coordination structure of the catalyst surface, we did not specifically address its structural sensitivity, such as the common size impact, when regarding the selective hydrogenation of α,β-unsaturated aldehydes. In fact, the relationship between the reaction activity, selectivity, and size and morphology of metal nanoparticles has been examined in numerous works. The results of the available studies, however, should be handled with caution. The reason lies in the catalytic performance being affected by the parallel structure-sensitive decarbonization side reaction.[181,200−202] As shown in Figure 11a, no significant deactivation for the activity (H_2 uptake or initial TOF) of citral hydrogenation was detected on Pt/SiO_2 during the course of reaction at 373 and 428 K, while substantial deactivation was observed at 298 K.[203] Unexpectedly, the activity decreased as the temperature increased. The reason has been verified to be the CO inhibition from the decarbonylation side reaction that occurred at undercoordinated sites by kinetic[203−205] and spectroscopic studies.[206−209] The apparent energy barrier for the decarbonylation reaction was only 29 kJ/mol while that for CO desorption was

https://doi.org/10.1021/acscatal.2c05141
ACS Catal. 2023, 13, 974−1019

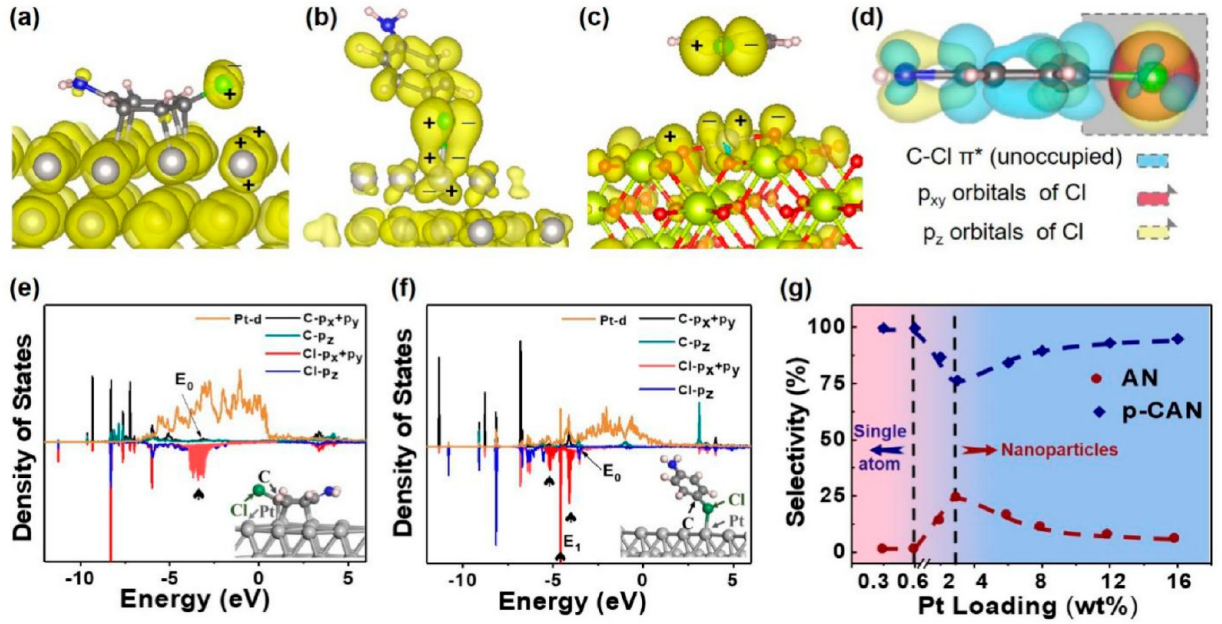

Figure 12. Residual unpaired frontier orbitals on Pt ((a) facet site, (b) edge site, (c) single atom site (Pt_1/CeO_2), and (d) *p*-chloronitrobenzene) and the interaction between them. Also shown is the projected density of states for the adsorption of *p*-chloronitrobenzene on Pt ((e) facet site and (f) edge site). (g) Unconventional size effect for the selectivity trend for the hydrogenation of *p*-chloronitrobenzene on the Pt/CeO_2 catalyst. [Reproduced with permission from ref 221. Copyright 2020, Elsevier.]

estimated to be 109 kJ/mol.[210,211] This suggests that the decarbonylation process can occur slowly and cover the catalyst surface at 298 K. At 373 K, although both the rates for CO formation and desorption are enhanced and yield a pseudo-steady-state balance, a larger fraction of active sites is inhibited by adsorbed CO. The pseudo-steady-state balance would experience conventional Arrhenius behavior, along with the reaction temperature, as shown in Figure 11b.[203] When reaction temperature is lower than the desorption temperature of CO, the inhibition of CO dominates. Then the initial activity of α,β-unsaturated aldehydes hydrogenation is insensitive to the portion of undercoordinated sites under this range of reaction temperature. Otherwise, the coverage of CO is strongly dependent on the supplier. Then the portion of undercoordinated sites deeply affects the initial hydrogenation activity. As a result, the polygonal line type particle size effect on the initial activity of α,β-unsaturated aldehydes hydrogenation is expected at 373 K, while it is not the case at 298 K, as shown in Figures 11c and 11d.[212] Acetylene semihydrogenation suffers from the similar situations by carbon deposition and will not be discussed in detail here. This type of secondary structure effect should be cautioned, which is caused by side reactions, reaction conditions, adsorption-induced surface rearrangement, a change in the rate-determining step, and other situations.[203,213,214] The absence of a significant variation in specific activity or selectivity with changes in the various crystallite sizes or morphologies clearly indicates the structure insensitivity. However, it does not necessarily imply the structure sensitivity in the other case. A different set of reaction conditions to crystallite size effects should be probed to exclude the mass-transfer limitation[215] and the process of the reaction should also be examined.[216]

In the end of the discussion of the surface coordination or steric effect, it is necessary to briefly elaborate on the electronic effect principle behind the coordination sensitivity. The essence of the modification or optimization of the coordination structure of the active site is to adjust the reacting orbitals of the active site, such as symmetry, ductility, and other fine electronic structures. According to the frontier orbital theory, the highest occupied molecular orbital (HOMO) and lowest unoccupied molecular orbital (LUMO) contributes the most reactivity.[217,218] Specifically, the residual unpaired orbitals determine most of the reactivity of the active sites on the surface of metal particles. Meanwhile, the residual unpaired orbitals are further related to the surface coordination structure.[219,220] As seen in Figure 12, the only residual unpaired orbitals on Pt(111) belong to d_{z^2} with only one quadrant in the vertical direction, while double quadrant d_{yz}/d_{xz} orbits stand perpendicularly on undercoordinated sites such as edge and corner sites.[221] When it comes to the planar single Pt sites, double quadrant dyz/dxz orbits stand perpendicularly on Pt, coupled with antiphase p orbital of adjacent oxygen on each side. The difference in the structure or morphology of residual unpaired orbitals on active sites of varied coordination structure determines the general reactivity. Take the C−Cl activation, for example; a premise must be met before the injection of electrons from the residual unpaired *d* orbitals of metal active sites to the LUMO (π^*) of the C−Cl bond, because of the unique core−shell orbital structure for HOMO (p_{xy}) and LUMO on the C−Cl bond, as shown in Figure 12d, i.e., the orbital symmetry between the residual unpaired *d*-orbitals of metal active sites and HOMO of C−Cl bond should match each other; otherwise, the strong coulombic repulsion between them would inhibit the following electron injection process. Apparently, the d_z^2 on Pt(111) with single orbital quadrant cannot match with double quadrant p_{xy} on C−Cl bond and steric effect occurs. In contrast, double quadrant d_{yz}/d_{xz} on Pt edge sites can bond effectively with p_{xy} on C−Cl bond. Therefore, the undercoordinated sites on Pt are responsible for the hydrodehalogenation side reaction and the size effect is expected for selective hydrogenation of halogenated nitrobenzene, as shown in Figure 12g. Another

https://doi.org/10.1021/acscatal.2c05141
ACS Catal. 2023, 13, 974−1019

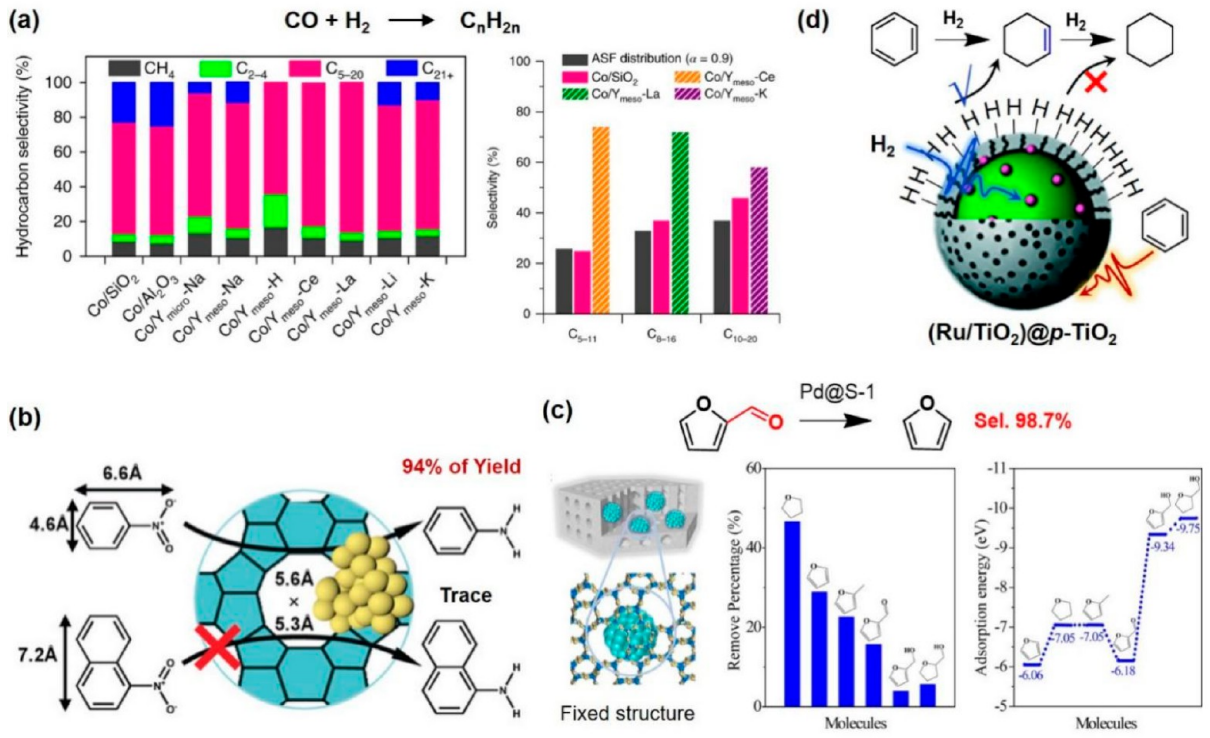

Figure 13. (a) The synergetic catalysis of Co metal site and molecular sieve breaks the ASF distribution of Fischer−Tropsch synthesis. (b) The size-selective catalysis of Pd@S-1 in the hydrogenation of nitrobenzene and 1-nitronaphthalene mixture. (c) The selective hydrogentaion of furfural to furan on Pd@S-1 with fixed structure and the relative escapability of various molecules on Pd@S-1 during the preadsorption and desorption test. (d) Benzene hydrogenation to cyclohexene with spillover hydrogen atom on Ru/TiO_2@p-TiO_2 catalyst where only H_2 is accessible to Ru metal site. [Panel (a) has been reproduced with permission from ref 228. Copyright 2018, Springer Nature. Panel (b) has been reproduced with permission from ref 232. Copyright 2016, Wiley−VCH. Panel (c) has been reproduced with permission from ref 235. Copyright 2021, American Chemical Society, Washington, DC. Panel (d) has been reproduced with permission from ref 43. Copyright 2017, Royal Society of Chemistry, London.]

example is the selective hydrogenation of α,β-unsaturated aldehydes. The coulombic repulsion between facet d_z^2 and the substituent group like alkyl group on α,β-unsaturated aldehydes is helpful for the selectivity to α,β-unsaturated alcohol.[181,222−226] Actually, the above electronic effect, such as orbital symmetry or steric effect derived from the surface coordination structure, can be roughly assessed with a simple but quantified descriptor coordination number. As seen, coordination number is a geometric description of the electron effect and researchers are prone to this geometric description for its vivid physical chemistry picture.

However, one should keep in mind that it is far from enough for selective hydrogenation with this rough descriptor, based on decades of years of experience. More accurate descriptors are urgently needed.

4.1.2. Spatial Confinement and Matching Effect. In addition to the coordination structure on the surface of the active site affecting the catalytic performance, the reaction microspace where the active site is located also has an important impact on the reaction performance. When the regulation of the surface coordination structure of the active site cannot achieve a satisfactory catalytic performance, the limitation of this strategy can often be well compensated by the design of the reaction space. In the discussion in the previous section, we have introduced several examples to improve the hydrogenation selectivity through the design of reaction space in detail, such as inhibiting the adsorption of C═C bond through space confinement to realize the selective hydrogenation of the C═O bond in α,β-unsaturated aldehydes.[195,196,198,199] In fact, the spatial confinement effect is quite common in molecular sieve catalysis, which is also known as shape-selective catalysis.[227] When metal sites are introduced into the molecular sieve, the hydrogenation selectivity can be controlled by the classical shape selection ability of the molecular sieve.

For research in the early stage, the shape-selective ability of molecular sieves did not directly affect the hydrogenation process, but functioned in the tandem catalytic process with two/multisite synergism. For example, loading Co nanoparticles on Y-type zeolites, the authors reported an integrated catalytic system for the direct conversion of syngas (CO/H_2) into different types of liquid fuels different from traditional Anderson−Schulz−Flory (ASF) distribution (seen in Figure 13a).[228] When metal nanoparticles are embedded inside the zeolite, the micropores in the zeolite can serve as diffusion channels and provide a local environment for reactions. Then the shape selectivity is introduced into the hydrogenation process. Generally, the spatial confinement effect can affect the hydrogenation process by sieving molecular diameters, controlling the adsorbing strength of reactants or crucial intermediates, and enriching the key intermediates in the micropores.[229−232] The molecular diameter sieving process usually occurs outside the zeolite. If the molecular diameter of any reactant in a feed mixture is larger than the maximum pore size of the zeolite, they are left unreacted and end up in a mixture with the products, since they cannot diffuse into the

https://doi.org/10.1021/acscatal.2c05141
ACS Catal. 2023, 13, 974−1019

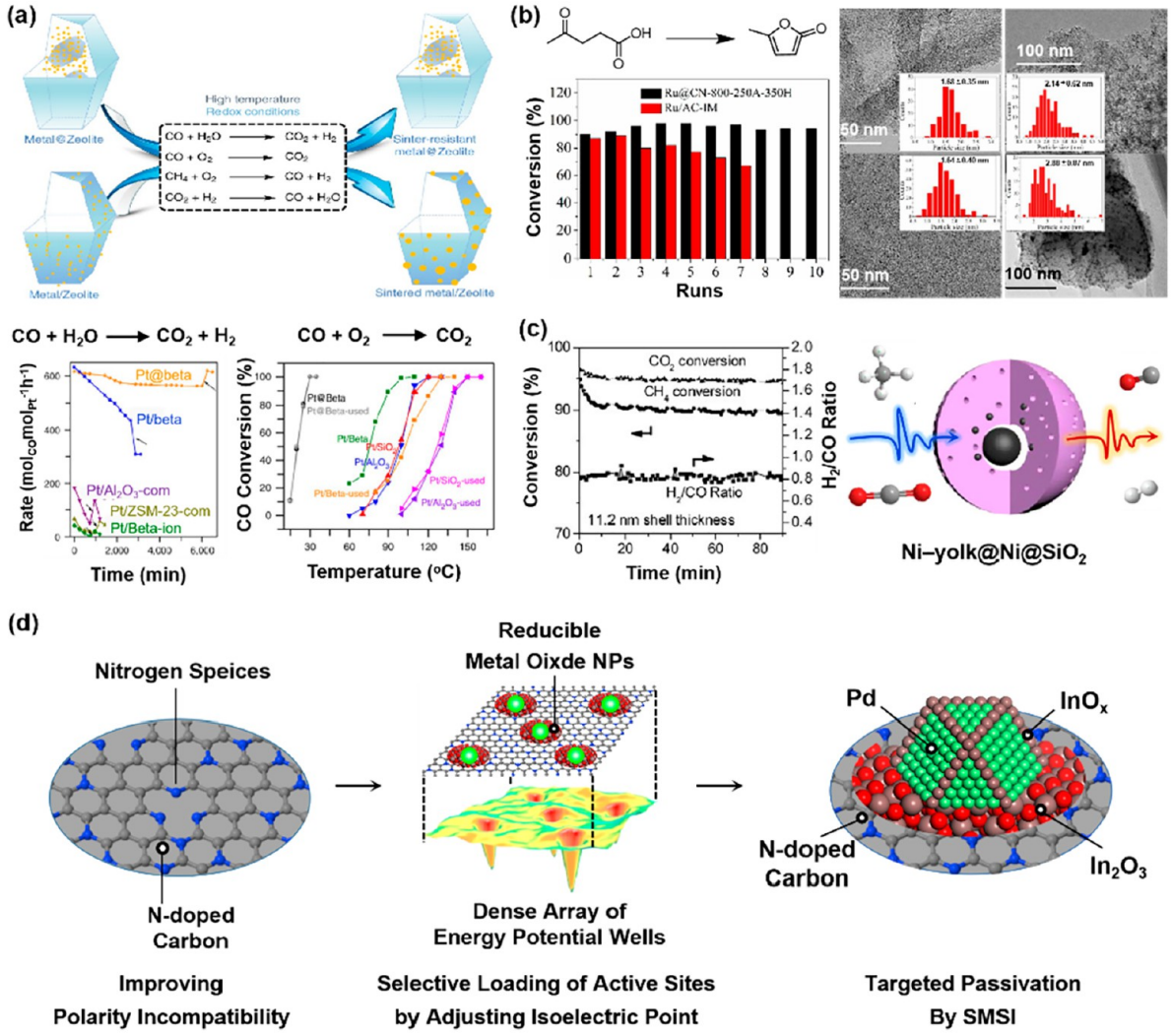

Figure 14. (a) Schematic model of metal nanoparticles fixed within and on the outer surfaces of zeolite crystals, and the catalytic performance comparison. (b) The stability test for carbon-embedded Ru catalyst in the hydrogenation of levulinic acid. (c) The stability and coke deposition resistance of yolk-satellite-shell structured Ni-yolk@Ni@SiO_2 nanocomposite catalyst for the dry reforming of methane. (d) Scheme of energy based spatial confinement. [Panel (a) has been reproduced with permission from ref 242. Copyright 2018, Springer Nature. Panel (b) has been reproduced with permission from ref 245. Copyright 2018, American Chemical Society, Washington, DC. Panel (c) has been reproduced with permission from ref 249. Copyright 2014, American Chemical Society, Washington, DC.]

zeolite framework. In the hydrogenation of nitrobenzene (4.6 Å × 6.6 Å) and 1-nitronaphthalene (6.6 Å × 7.3 Å) mixture with Pd nanoparticles encapsulated in Silicalite-1 (Pd@S-1), as seen in Figure 13b, aniline can realize 94% yield while 1-nitronaphthalene was only converted in trace amounts, since the diffusion of 1-nitronaphthalene with a large molecule size into the micropores (5.3 Å × 5.6 Å) of S^{-1} was suppressed.[232] Wang et al. synthesized a mesoporous carbon molecular sieve with embedded with Pt nanoparticles. The embedded Pt nanoparticles are connected with mesoporous channels through short micropores (~5.8 Å) formed by air etching. The efficient selective hydrogenation of 4-chloronitrobenzene to 4-chloroaniline in 4-chloronitrobenzene and 1-nitronaphthalene mixture was realized though the enhanced mass transfer from mesopores and size sieving of micropores.[233] A similar size/shape selectivity of Pd@S-1 was also observed in oxidation and carbon−carbon coupling reactions.[232] By fixing the Pd nanoparticles into S-1 zeolite (Pd@S-1), the catalyst exhibited an entirely different product distribution, compared to the supported ones.[234,235] As shown in Figure 13c, furan selectivity increased from 5.6% on Pd/S-1 to 98.7% on Pd@S-1 at 91.3% conversion.[235] The reason behind this phenomenon can be explained by the controlled diffusion of products such as furfural alcohol and furan through the distinction of adsorbing strength. The enriching of furfural alcohol in the micropores of zeolite benefits the further decarbonylation and hydrogenation to furan. When Bronsted acid sites were further introduced, the trapped furfural alcohol would go through the ring opening and hydrogenation processes and the main product changed to 1,5-pentanediol on Pd@H-ZSM-5.[236]

Besides the molecular sieve, other interesting encapsulated structures, such as core−shell MOFs and yolk−shell nanoreactors with micropores as mass transfer tunnels, can also exhibit the shape-selective catalysis.[195,237−239] In contrast to the shape-selective mass transfer to organic substrates in molecular sieves, sometimes the shape-selective mass transfer to H_2 on coated reducible metal oxide with strong hydrogen spillover ability will behave differently. Take benzene hydro-

https://doi.org/10.1021/acscatal.2c05141
ACS Catal. 2023, 13, 974−1019

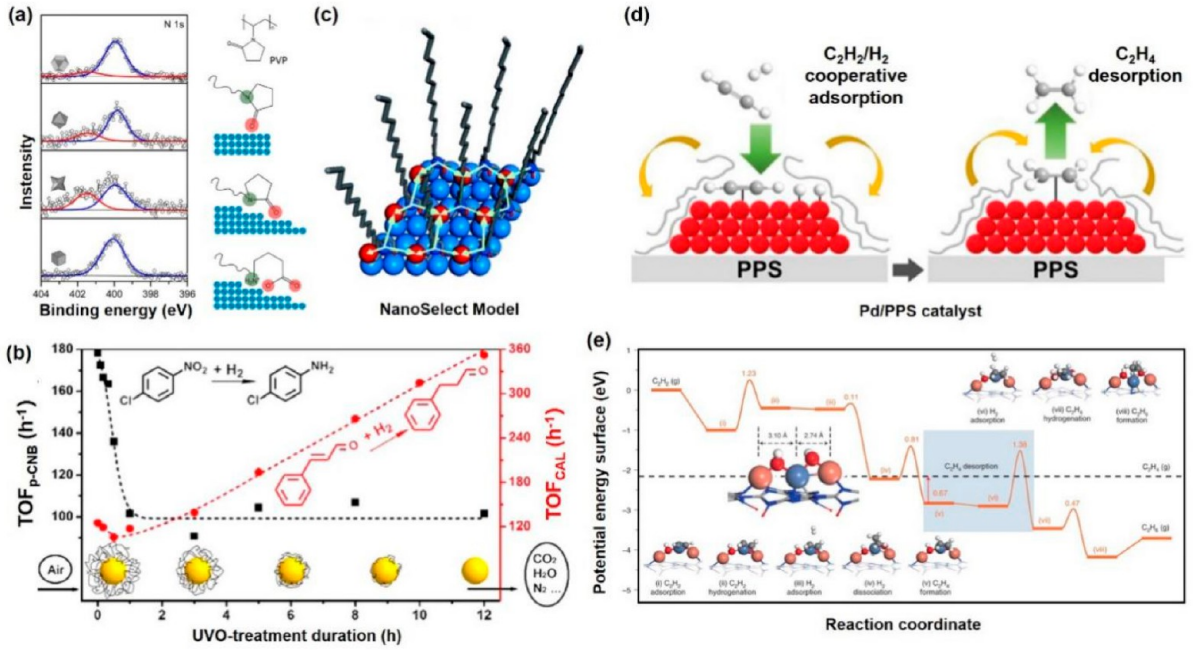

Figure 15. (a) N 1s spectra of PVP-Pd NPs immobilized on activated carbon, and schematic illustrating the interaction modes between PVP and Pd NPs. (b) Effects of UVO-treatment duration on the Au activity of Au-PVP/SiO_2 catalyst for *p*-CNB and CAL hydrogenation. (c) Scheme for NanoSelect catalyst. (d) Proposed scheme for acetylene partial hydrogenation on Pd/PPS. (e) Optimized potential energy surfaces of acetylene partial hydrogenation on Ni_1Cu_2/g-C_3N_4 dynamic atomic nickel catalyst. [Panel (a) has been reproduced with permission from ref 266. Copyright 2014, American Chemical Society, Washington, DC. Panel (b) has been reproduced with permission from ref 267. Copyright 2014, American Chemical Society, Washington, DC. Panel (c) has been reproduced with permission from ref 268. Copyright 2014, Wiley−VCH. Panel (d) has been reproduced with permission from ref 272. Copyright 2020, AAAS. Panel (e) has been reproduced with permission from ref 273. Copyright 2021, Springer Nature.]

genation to cyclohexene as an example; the selectivity remains very low at a relative high conversion, because of the easy hydrogenation of cyclohexene on the surface of Ru. Hence, the suppression of the further hydrogenation of cyclohexene is rather challenging. After coating a supermicroporous TiO_2 layer over Ru/TiO_2 catalyst (Ru/TiO_2@p-TiO_2), as shown in Figure 13d, only H_2 was allowed to diffuse into the supermicropores and attach the Ru sites.[43] Herein, different from the supported counterpart, the encapsulated Ru particles only serve as active sites for hydrogen dissociation while the porous TiO_2 surface acts as the active center for benzene hydrogenation (namely, hydrogenation of benzene through spillover H atoms). This change in hydrogenation mechanism accounts for inspiring enhanced catalytic performance with cyclohexene selectivity of ∼77% at 98% conversion, which is much higher than the rest of the results reported at that time. A similar idea has also been applied in alkane direct dehydrogenation, in which the dehydrogenation and hydrogenation desorption processes occur on different sites, preventing the traditional serious carbon deposition and exhibiting remarkably durable activity.

Apart from the effect on the selectivity, spatial structure confinement would also improve the stability of the catalyst significantly, in comparison with the supported nanocatalyst systems. By keeping the active center from coalescence, as shown in Figure 14a, metal particles (Pt, Pd, Rh, Ru, Au, Ag) encapsulated in zeolite, metal oxide, or carbon remained almost the original particle sizes after calcination at temperatures close to or even higher than the Tamman temperature,[240−243] which is a condition where the stabilities of supported metal catalysts are confronted with serious challenges. Metal leaching can also be greatly suppressed for metal catalysts with a spatial structure confinement effect. For example, the industrial Pd/C catalyst leached ∼6.7% of the Pd loading in the liquid hydrogenation of 4-nitrochlorobenzene for 90 h, while Pd@Beta exhibited almost undetectable leaching Pd species under the equivalent test.[244] Under more-severe reaction conditions, the Ru@CN-800−250A-350H catalyst displayed more excellent stability for the hydrogenation of levulinic acid at 100 °C with more than 10 successive recycling runs. The comparative supported Ru/AC-IM catalyst, however, as seen in Figure 14b, exhibited a drastic decrease in stability after three runs under the same reaction conditions.[245] A similar trend has also been found in the hydrogenation of benzoic acid, where supported catalysts reached a leaching as high as 49.3% for Rh/N−C−IM (after seven cycles) and 42.3% for Rh/N−C−$NaBH_4$ (after six cycles), while Rh@NC only endured 12.5% leaching of Rh content.[246] Note that this stabilization of metal components applies for various reactions as hydrogenation of CO_2, CO oxidation, Suzuki cross-coupling, etc.[247,248] Interestingly, the coke-induced deactivation of the catalyst can also be greatly reduced, although the exact reason is still under investigation. As shown in Figure 14c, a yolk-satellite-shell structured Ni-yolk@Ni@SiO_2 nanocomposite catalyst showed excellent durability for 90 h at 800 °C for the dry reforming of methane.[249] Similar results has also been reported on Ni@Al_2O_3 core−shell catalyst with remarkable activity and stability of a 50 h durability evaluation.[250] The carbon deposition for Ni@Al_2O_3 core−shell catalysts was only ∼15% weight loss, which probably can be further improved on the one with each Ni trapped within single Al_2O_3 shell and further modulation of

https://doi.org/10.1021/acscatal.2c05141
ACS Catal. 2023, 13, 974−1019

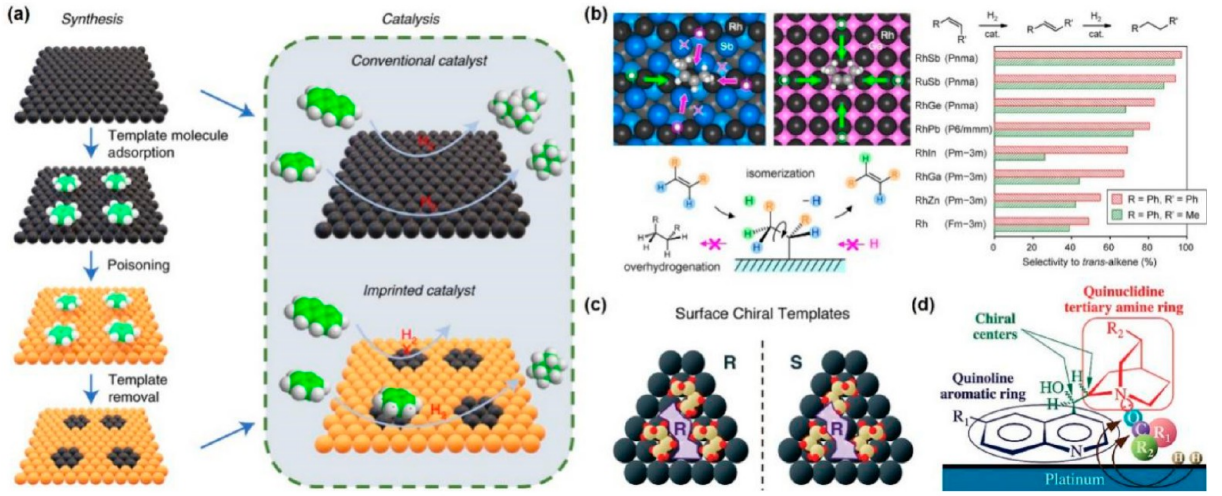

Figure 16. (a) Illustration of the molecular imprinting strategy over a palladium surface. (b) Mechanism for the geometric restriction of hydrogen access to *cis*-2-butene on RhSb(020) and RhGa(100) and the selectivities to *trans*-alkenes during *cis*-ST and *cis*-MS isomerizations on various SiO_2-supported Rh- and Ru-based intermetallic compounds and monometallic Rh catalysts. (c, d) Schematic illustrations of the two main models by which chiral modifiers are proposed to bestow enantioselectivity to heterogeneous catalysts: panel (c) depicts the formation of supramolecular surface chiral templates through self-assembly of achiral molecule and panel (d) depcits the formation of one-to-one complexes between the chiral modifier (cinchonidine) and the reactant. [Panel (a) has been reproduced with permission from ref 274. Copyright 2021, Springer Nature. Panel (b) has been reproduced with permission from ref 275. Copyright 2015, Wiley−VCH. Panel (c) has been reproduced with permission from ref 19. Copyright 2008, American Chemical Society, Washington, DC. Panel (d) has been reproduced with permission from ref 276. Copyright 2009, American Chemical Society, Washington, DC.]

the shell thickness. When changing the shell to more inert SiO_2, Ni@HSS shows negligible activity loss and carbon deposition after 55 h.[251] Besides the above direct spatial confinement effect by physical obstacle, energy-based spatial confinement provides us with another option.[252,253] As shown in Figure 14d, reducible metal oxide NPs dispersed on inert supports will induce a dense array of energy potential wells, which can further trap the metal active sites from agglomeration.[254,255] In addition, one can continue to apply the direct spatial confinement effect to further tune the active sites, such as the targeted passivation strategy as illustrated in Figure 9d. Recently, metal oxide nanoparticles such as TiO_2, Cr_2O_3, and CeO_x were used to disperse and stabilize multielemental alloy nanoparticles or even atomically dispersed catalysts with a similar concept.[256,257]

Single atom or the alloy catalyst is another typer of thriving catalyst, making full of the spatial confinement effect to disperse and stabilize the active metal species. Yet, we will not discuss it in detail here, since there have been many reviews to sort and classify it.[2,258−264] The spatial confinement effect from inorganic carriers is often rigid. In contrast, the flexible space confinement effect based on organic molecules can also effectively regulate the catalytic performance. Among them, the most widely known is the surface ligand effect caused by surfactants. Surfactants are commonly used for the stabilization of nanocrystallines with a colloidal method, since they are generally constituted by a polar group able to generate an electronic double layer and a lipophilic side chain that also provides steric repulsion for the parallel adsorption of large volume functional groups on the surface of the catalyst.[265] Generally, researchers study them by binding ligands on the surface of nanometals. Although the original intention of studying the ligand effect was to measure the negative interference brought by the surface ligand when studying the surface geometry effect of nanocrystalline catalysts, as seen in Figure 15a, researchers gradually found that its positive effect on selective regulation can also be utilized.[266] In addition to the aforementioned oleylamine-capped Pt_3Co nanoparticles for the selective hydrogenation of the C═O bond in α,β-unsaturated aldehydes, such catalysts are also widely used in other geometry-sensitive hydrogenation reactions. Xu et al. investigated the influence of the residual stabilizer on Au-PVP/SiO_2 catalyst to the selective hydrogenation reactions.[267] Results showed that the amount of PVP strongly impacted on the catalytic performance on the selective hydrogenation of *p*-chloronitrobenzene and cinnamaldehyde. The presence of residual PVP stabilizer was quite beneficial to the Au activity for the hydrogenation of *p*-chloronitrobenzene to *p*-chloroaniline, while it was detrimental to the efficiency for the hydrogenation of cinnamaldehyde to phenylpropanal (seen in Figure 15b). The detailed mechanism in the differences of the activity trend for the hydrogenation of *p*-chloronitrobenzene and cinnamaldehyde controlled by a capping agent still remains to be investigated further. Through the grafting of hexadecyl (2-hydroxyethyl) dimethylammonium dihydrogenphosphate (HHDMA) on the surface of Pd particles, Pd NanoSelect catalyst, as shown in Figure 15c, exhibited 93.5% yield to MBE for the hydrogenation of MBY, while eliminating the adoption of heavy metals such as Pb and Bi.[268−270] Excellent alkene selectivities were obtained in the hydrogenation of a batch of aliphatic alkynes (96%−99% at 95% conversion) on PVP-stabilized PdNPs.[151] PEG2000-grafted RuNPs as catalysts achieved 97% selectivity to methyl acrylate in the hydrogenation of methyl propiolate at 92% conversion.[271] In recent years, some different catalyst structures have also provided a distinctive perspective for studying the flexible spatial confinement effect of organic molecules. Lee et al. reported reversible huff-and-puff Pd catalysts where Pd particles were supported on a "soft" polyphenylene sulfide (PPS) plastic for acetylene partial hydrogenation in an ethylene-rich stream, as shown in Figure 15d.[272] The thermochemically stable and mobile PPS chains would cover

https://doi.org/10.1021/acscatal.2c05141
ACS Catal. 2023, 13, 974−1019

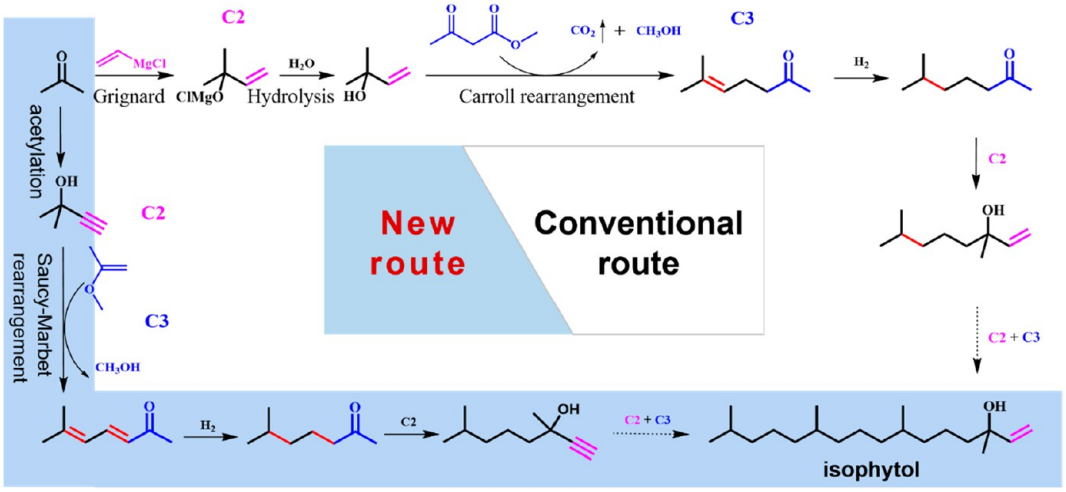

Figure 17. Route comparison for the synthesis of isophytol.

the Pd particles near the glass-transition temperature (~353 K) via strong metal−polymer interactions (Pd−S). During the reaction, acetylene's strong binding affinity to Pd opens a seam and enables H_2 activation. Once acetylene is hydrogenated to weakly binding ethylene, the recoverage of PPS on the Pd surface repels ethylene and inhibits further hydrogenation. However, the selectivity to ethylene is <80%, due to the low fluidity of plastics. In contrast to grafting the ligands on the surface of metal particles, Wang et al. reported a "breathing" catalyst by fixing the chain flexible alkylamine on the surface of the support, as seen in Figure 9e, in which the amino groups bind back to the metal surface.[150] When adjusting the chain length and the metal particle size, the metal surface would be covered by the amino groups. Since the strength of the interaction of Pd-amino groups is between the adsorption strengths of alkyne and alkene, then a recycle process is observed in which the binding of Pd-amino groups is broken upon the adsorption of alkyne and recovered upon the repulsion of alkene from hydrogenation, during which the recognition adsorption of the target substrate is achieved. The excellent flexibility of chain alkylamines makes the frequency of this reversible respiration procedure compatible with the hydrogenation rate. As a result, recorded activity (14 412 h^{-1}) and satisfied yield (98.2%) were realized in the meantime. This idea of using the difference of the adsorption energy of reactants and products on the catalyst surface to suppress side reactions and improve the selectivity of target products breaks through the inherent limitation of the original ligand-grafted catalyst that uses ligand steric hindrance to improve the product selectivity, and embodies the insight of using recognition adsorption to adjust the hydrogenation selectivity. Of course, this type of structural reversibility is not unique only to organic ligands. Through synergizing metal−support interactions and spatial confinement, Lu et al. reported a type of dynamic atomic nickel catalyst for the semihydrogenation of acetylene in excess ethylene.[273] Similar to the above two new catalysts, results reveal that the active nickel site, which is confined in two stable hydroxylated copper grippers, can dynamically change by breaking the interfacial nickel support bonds upon acetylene adsorption and forming these bonds upon ethylene desorption, as shown in Figure 15e. Such a dynamic interaction contributes 90% ethylene selectivity at almost full conversion of acetylene.

In any case, realizing atomic level space matching is a crucial avenue for the research in this field. A surface molecular imprinting strategy was reported to control the hydrogenation selectivity over a supported palladium catalyst, as shown in Figure 16a.[274] This strategy begins with the sequential adsorption on the metal surface of a template molecule, followed by polymer matrix poisoners. After removing the template molecules, active metal islands of predetermined shape and size is exposed. Because of the steric constraints of the template molecules, the exposed active metal islands exhibit high selectivity in the conversion of substrates that correspond in size and shape to the templates. Although the overall efficiency has been limited for selective hydrogenation until now, this tight matching surface molecular imprinting strategy itself is elaborating and enlightening. An investigation on the *trans*-hydrogenation of alkynes or *cis*−*trans* alkene isomerization displayed another example in the precise modification of surface structure. Hydrogen access to *cis*-2-butene encountered apparent geometric restrictions on RhSb(020) and RhGa(100) of *Pnma* structure with zigzag arrange of alloy elements, as shown in Figure 16b.[275] As a result, selective *cis*−*trans* alkene isomerization was realized. Perhaps the most familiar example is the asymmetric hydrogenation with a metal surface adsorbed with chiral modifiers.[19] The created local chiral space is always considered to be the origin for the asymmetric hydrogenation of the substrates. At present, mainly two families of chiral modifiers have been explored. One is tartaric acid, which has been used to promote the enantioselectivity for β-ketoester hydrogenation on nickel catalysts. Interestingly, since the tartaric acid molecule is not chiral, it cannot provide a local chiral space by itself to promote the asymmetric hydrogenation steps. Actually, the local chiral environment originates from the adsorbate superstructure formed by the self-assembly of the individual molecules in specific patterns, which enlightens us to the fact that the asymmetric process does not necessarily involve the participation or inducement of chiral molecules.[276] As shown in Figure 16c, three molecules of the enantiopure templating agents, such as 2-butoxide, either in the (R) (left panel) or the (S) (right panel) forms, assemble a pocket of specific chirality on the surface. Another family is based on cinchona alkaloids with chirality, as shown in Figure 16d, which are more promising and were used to enantioselectively

https://doi.org/10.1021/acscatal.2c05141
ACS Catal. 2023, 13, 974−1019

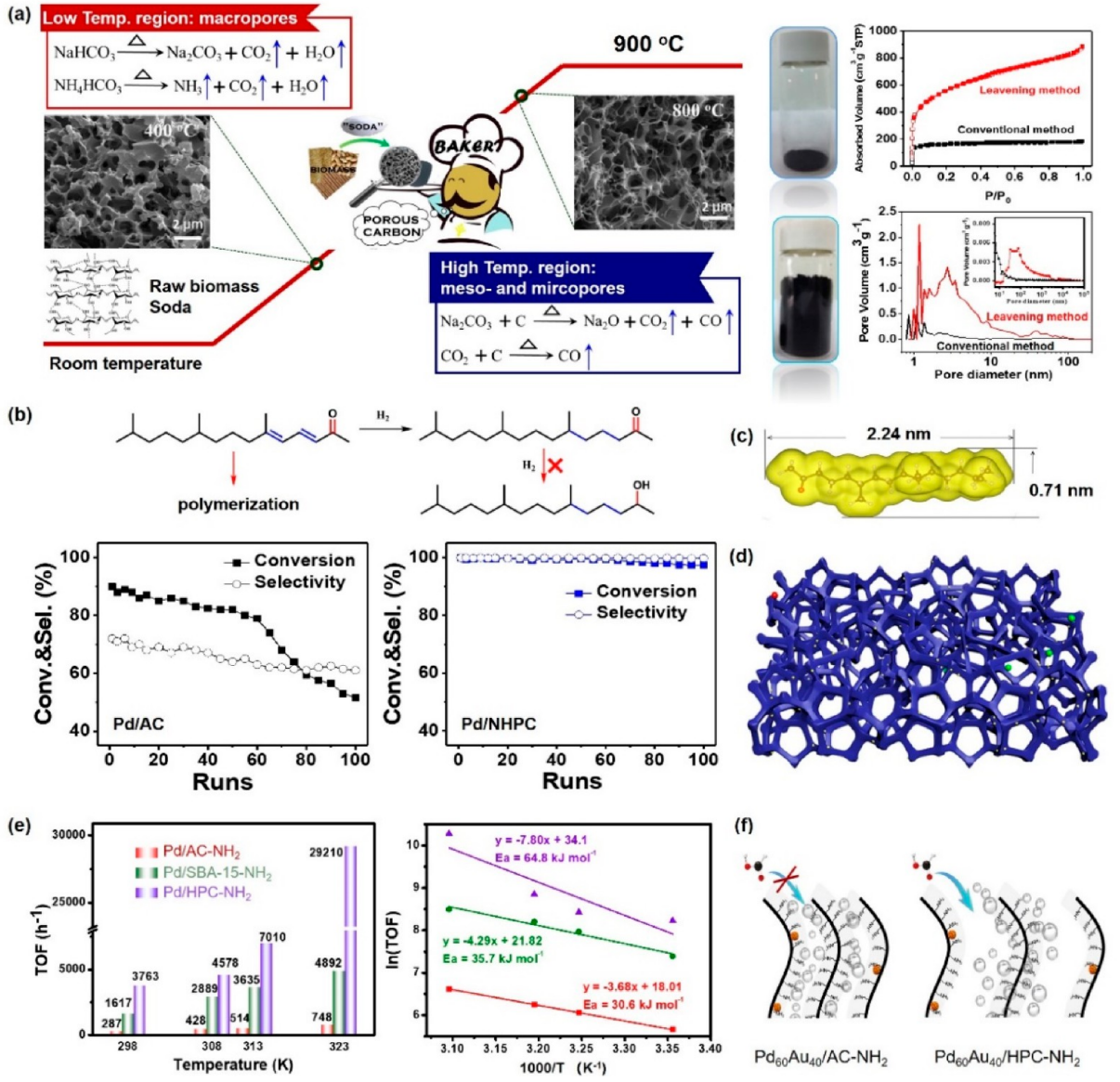

Figure 18. (a) Scheme for the leavening method for the preparation of nitrogen doped 3D-interconnected hierarchical porous carbon (NHPC) and the specific surface and pore distribution. (b) Comparison for catalytic performance of the selective hydrogenation of conjugated diketene (C18) on Pd/AC and Pd/NHPC. (c) van der Waals volume of C18. (d) Scheme of the 3D-interconnected hierarchical pores for NHPC. (e) Comparison for catalytic performance of dehydrogenation of formic acid without additive on catalysts of different pore sizes. (f) Scheme of the impact of bubbles for dehydrogenation of formic acid. [Panel (a) has been reproduced with permission from ref 291. Copyright 2015, Royal Society of Chemistry, London. Panels (e) and (f) have been reproduced with permission from ref 215. Copyright 2021, Elsevier.]

hydrogenate α-ketoesters on platinum catalysts at first.[19,276] Excellent enantiomeric excess (ee) values have been achieved with specific substrates, such as ethyl pyruvate.[277−279] The scope of reactions is still limited, although other examples such as the asymmetric hydrogenation of other ketonic molecules,[17,280−285] and alkenes,[17] as well as the asymmetric C−C bond couplings have already been reported to be positive. Now more chiral modifiers, such as amino acids[286,287] and aromatics (e.g., indans and indols),[288] and mechanisms revealing the origin of enantioselectivity, such as kinetic resolution and chiral catalysis, are being gradually discovered.

The confinement effect based on the restriction of pore size, which often leads to a decrease in efficiency for mass transfer. Serious side reactions such as carbon deposition will occur in the selective hydrogenation of metastable molecules of large size under such conditions. Therefore, sufficient mass transfer and reaction space should be given instead to such reactive molecules, to match the target reaction rate. This is particularly important for industrial catalysts, because most industrial reactions are actually mass-transfer-limited. Generally, reducing the carrier size by various methods to reduce or even eliminate the diffusion length of micropores and increasing the ratio of mesopores to macropores are relatively popular and effective methods. The key is how to develop an economic and effective method to improve the reaction mass transfer. Here, we give an example of the development of an industrial catalyst for the selective hydrogenation of conjugated diketene, a key intermediate of vitamin E. Vitamin E is mainly prepared industrially by condensation of isophytol (IP) with trimethylhydroquinone (TMHQ).[289] The preparation of isophenol is particularly complex. As shown in Figure 17, the most widely used route involves multiple steps of Grignard and hydrolysis

https://doi.org/10.1021/acscatal.2c05141
ACS Catal. 2023, 13, 974−1019

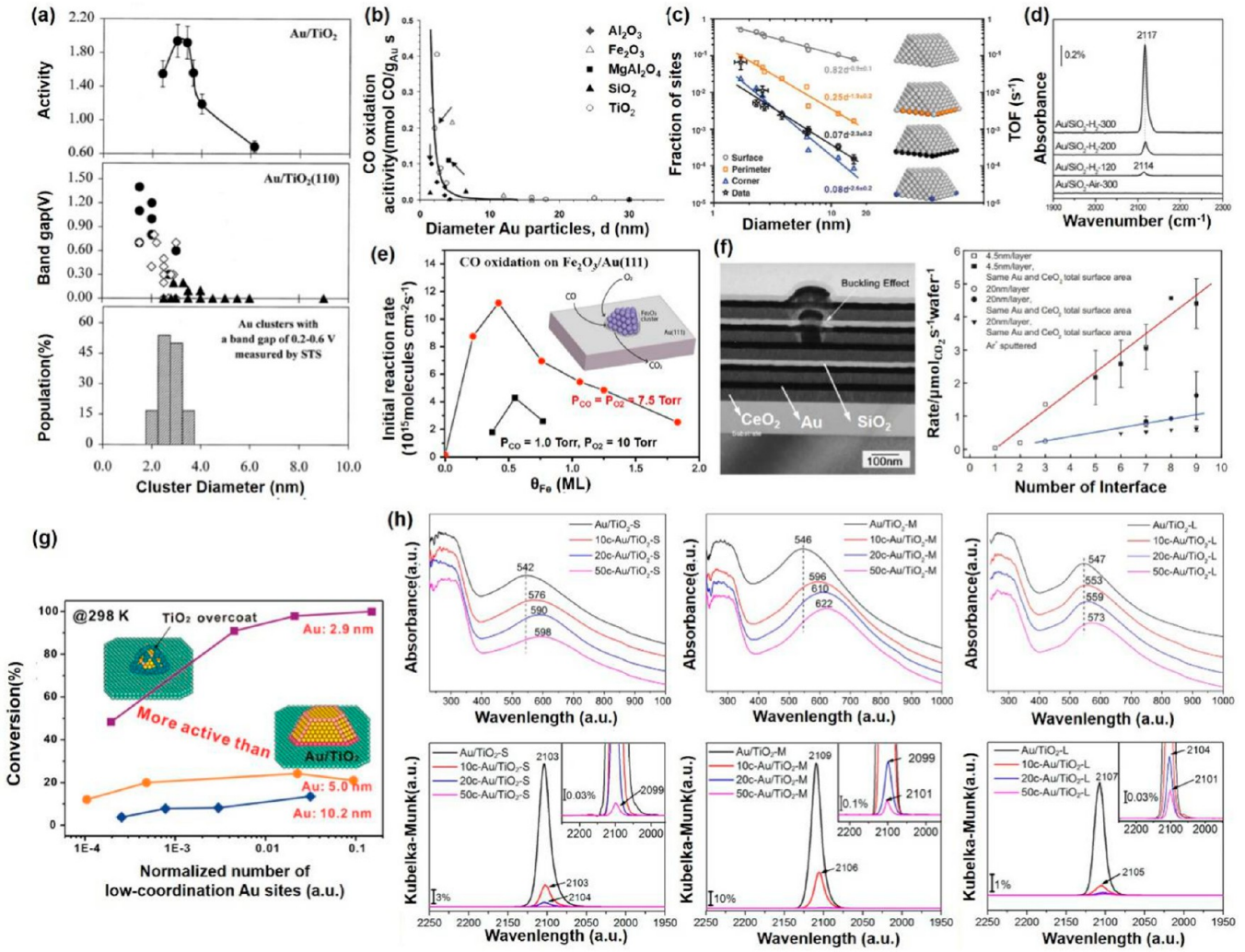

Figure 19. (a) The activity for CO oxidation and band gap measured by STS as a function of the Au particle size on TiO_2(110)-(1 × 1), and the relative population of the Au clusters (two atom layers in height) with a band gap of 0.2−0.6 V, as measured by STS. (b) Measured activities for CO oxidation on Au-based catalysts, as a function of the average particle size. (c) Calculated number of sites with a particular geometry (surface and perimeter or corner atoms in contact with the support), as a function of diameter and TOF of the nine ceria-based samples. (d) The infrared spectrum results of CO adsorption on Au NPs of different sizes. (e) CO_2 production rate during CO oxidation on Fe_2O_3/Au(111) catalysts with various Fe_2O_3 coverage. (f) CO_2 production rate normalized by catalyst on a 3-in. wafer and the TEM image of one typical sandwich-like catalyst. (g) CO conversion, as a function of the number of exposed low coordinated Au sites at room temperature. (h) UV-vis and DRIFT spectra of CO chemisorption on a series of Au/TiO_2 catalysts. [Panel (a) has been reproduced with permission from ref 302. Copyright 1998, AAAS. Panel (b) has been reproduced with permission from ref 303. Copyright 2004, Elsevier. Panel (c) has been reproduced with permission from ref 312. Copyright 2013, AAAS. Panel (d) has been reproduced with permission from ref 318. Copyright 2013, Royal Society of Chemistry, London. Panel (e) has been reproduced with permission from ref 315. Copyright 2012, Elsevier. Panel (f) has been reproduced with permission from ref 316. Copyright 2008, Wiley−VCH. Panels (g) and (h) have been reproduced with permission from ref 317. Copyright 2016, American Chemical Society, Washington, DC.]

reactions with an atomic economy of only 36%, enduring low atomic economy and serious environmental pollution. In view of the above problems, Wang et al. designed a new synthesis route of IP: starting from acetone, using long-chain conjugated diene as the key intermediate, only 11 steps involving acetylation, Saucy-Marbet rearrangement, and selective hydrogenation are needed. The atomic economy is >85% with H_2O as the only byproduct, which indicates that industrial waste emissions are largely avoided. The molecular dynamics diameter and size of the chain conjugated diketenes, however, are both large (0.71 nm) and long (>2 nm), as shown in Figure 18c. Because of the limitation of micropores (<2 nm), the internal diffusion of traditional Pd/AC is severely limited. As a result, the metastable conjugate structure formed by two C═C and one C═O bonds is easy to polymerize and block the channel, thus rapidly deactivating the catalyst. As shown in Figure 18b, the initial selectivity to saturated ketone only reached ∼70% at 90% conversion, and the selectivity and activity decreased continuously in the recycle process.[290] Therefore, Pd/AC shows terrible hydrogenation efficiency. It is necessary to develop catalysts with open and interconnected hierarchical pore structure on the support to strengthen the reaction mass transfer, to achieve high-efficiency hydrogenation of this key intermediate. Inspired by the bread leavening process, Wang et al. developed a one-pot "leavening method" to prepare nitrogen-doped 3D-interconnected hierarchical porous carbon (NHPC), as shown in Figure 18a, in which baking soda ($KHCO_3$ or $NaHCO_3$) is used as activators

https://doi.org/10.1021/acscatal.2c05141
ACS Catal. 2023, 13, 974−1019

and porogenic agents.[291,292] The specific surface area of NHPC could reach 1893 $m^2 g^{-1}$ and the proportion of mesopores and macropores as high as 82%. After loading on NHPC, the yield of the target product was as high as 99% on the new catalyst (Pd/NHPC). Meanwhile the catalyst could be stably reused for more than 60 times without obvious deactivation, because of the spacious reaction channel and space in NHPC (seen in Figure 18d). The pioneering work for the efficient selective hydrogenation of long-chain conjugated diketenes opens up a different green industrial route for the synthesis of IP or vitamin E. In addition, the application of NHPC to hydrogen production from the dehydrogenation of formic acid without additive, which involves the submicrometer bubble formation process, has also realized a satisfied performance.[215,293] As seen in Figures 18e and 18f, the TOF on $Pd_{60}Au_{40}$/HPC-NH_2 exhibited a value 2 orders of magnitude higher than that on $Pd_{60}Au_{40}$/AC-NH_2, because of the change of reaction kinetics from mass-controlled to kinetics-controlled.

4.2. The Electronic Effects for Selective Hydrogenation. Undoubtedly, the electronic structure of the catalyst will also affect the reaction performance. It can be even bolder to say that the catalytic performance of a catalyst is determined by its electronic structure. There would be no catalysis without an electronic effect. However, the elaborating of the electronic effect of the catalyst still must be very careful in specific cases. In the following, we will first take CO oxidation and acetylene hydrogenation as examples to describe the dangers of interpretation of electronic effects, then discuss in detail the manifestations of electronic effects under general and specific conditions. Eventually, we will propose some prerequisites or considerations to be followed in the study of electronic effects.

As the most important coinage metal, Au had been regarded as chemically inert for a long time, because of the lack of ability to activate any molecules.[97,294] However, this view has been subverted by the pioneering work of low-temperature CO oxidation on reducible metal oxide (TiO_2, α-Fe_2O_3, and Co_3O_4) supported gold nanoparticle catalyst by Haruta and co-workers.[295,296] This subversive discovery has led to extensive discussion on the origin of high activity, and multiple assumptions have been proposed.[297−301] One of the most familiar explanations is the electronic structure modulation from the nano effect, which has always been taken as an example to illustrate the quantum size effect at the nanoscale level. Goodman et al. observed a clearly metal−nonmetal transition for Au particles at a diameter of ∼3.5 nm (∼300 atoms) by measuring the band gap using scanning tunneling spectroscopy (STS).[302] Together with the maximum activity on ∼3.5 nm Au NPs (Figure 19a) on a conspicuous activity-size effect volcano curve, they hypothesized that the appearance of a nonmetallic property, i.e., the electronic effect, plays the primary role in the onset activity of CO oxidation on small Au NPs. However, Nørskov and co-workers suggested that the geometric factors such as the low coordinated Au active sites (LCSs) play a major role in the particle size effect of Au in CO oxidation, whereas the role of the support is relatively less important,[303−306] after collecting numerous published results for CO oxidation on Au catalysts on various supports and discovering an approximately proportional relationship about the activity of Au catalysts with the number of LCSs on the Au particles (Figure 19b).[303] This viewpoint has also been supported by the Overbury and Freund groups, because particle thickness does not play a significant role in CO adsorption.[307,308]

There also have been lots of researches proposing that the perimeter of Au/oxide interface is the key for CO oxidation (Figure 19c).[309−312] However, the way of studying the role of interfacial or perimeter sites by adjusting the size of gold particles cannot completely exclude the electronic effect brought by the particle size and the change of the ratio of LCSs.[313,314] To eliminate this defect, Mullins et al. ingeniously designed an inverse Fe_2O_3/Au(111) catalyst, as shown in Figure 19e, in which the initially inert Au(111) single crystal surface became active after depositing Fe_2O_3 nanoislands and exhibited a volcanic curve to the CO production rate with its maximum activity at 0.5 monolayers of Fe_2O_3 coverage.[315] The above results clearly demonstrated that the origin of the activity to CO oxidation does not necessarily come from the electronic effect or, more specifically, the quantum size effect at nanoscale, whereas it was directly derived from the formation of the Fe_2O_3/Au(111) interface. Furthermore, a sandwich-type Au/CeO_2 catalyst was designed as shown in Figure 19f with alternating Au and CeO_2 layers, in which only the sides of Au/CeO_2 interface were allowed to expose to the outside.[316] By varying the number of alternate Au and CeO_2 layers in this sandwich construction, it was possible to adjust the Au/CeO_2 interface without altering the size of each component. A linear relationship between the reaction rate and the amounts of Au/CeO_2 interfaces was found on this catalyst. Moreover, the catalyst became inactive when SiO_2 layers were inserted to separate Au/CeO_2 interfaces. These results also confirmed the unique activity of Au/CeO_2 interface for CO oxidation and excluded the size effect caused catalytic activity. Different from them, Lu et al. offered another option to investigate this topic. By selectively blocking the LCSs of Au NPs of different sizes (2.9, 5.0, and 10.2 nm) with ALD of TiO_2 precursor, the population of LCSs accessible for CO oxidation could be broadly tuned with the number of ALD cycles.[317] Results showed that the activity of Au catalysts largely remained steady, even though the number of exposed Au LCSs decreased by 3 orders of magnitudes after TiO_2 coating (Figure 19g) and the peaks in UV-vis diffuse reflectance spectra and DRIFT spectra of CO chemisorption in Figure 19h apparently shifted. The above discussion demonstrated that neither the quantum effect induced by size effect nor LCSs are likely to be the determining factor to the origin of the catalytic activity of Au.

However, there is no doubt that the quantum effect can influence the activity of Au for CO oxidation, but rather possibly in a negative way. Several studies revealed that when Au NPs are smaller than the critical size for the metallic−nonmetallic transition, the activity of Au NPs for low-temperature CO oxidation sharply decreases, or even completely deactivates.[311,318] The infrared spectrum results of CO adsorption in Figure 19d showed that CO was difficult to be adsorbed and activated on Au surface under this condition, leading to the activity loss. Therefore, the elaborating or correlating the change of the electronic structure based on the related characteristics, such as XPS, CO-IR,[317] STS,[302] and UV-vis,[317] with the activity variation of Au catalyst should be very cautious. It is very likely to be misleading. Another thing that should be noted is that the reaction behavior, such as the reaction mechanism and the rate-determining step, can be tuned by the reaction conditions and induce a reaction-condition-dependent structure sensitiv-

https://doi.org/10.1021/acscatal.2c05141
ACS Catal. 2023, 13, 974−1019

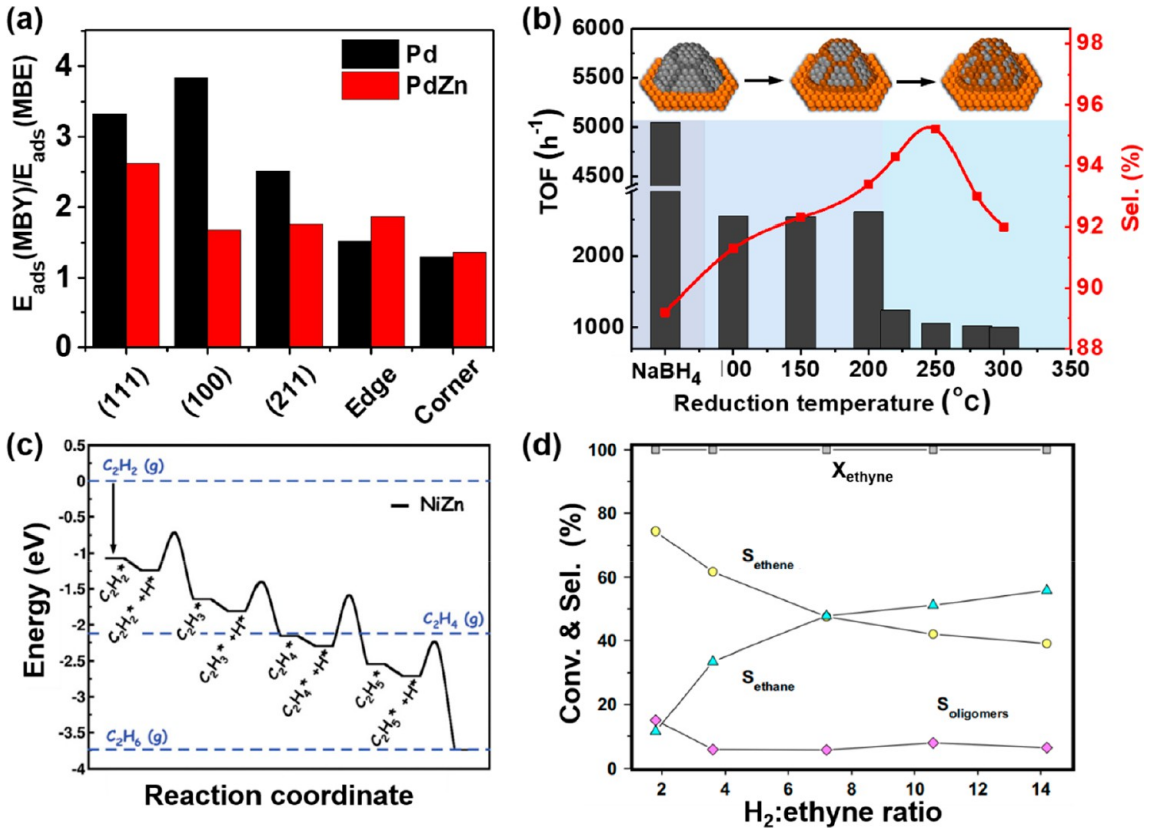

Figure 20. (a) Adsorption energy (E_{ad}) of MBY and MBE on Pd sites of different coordination. (b) Catalytic performance for MBY hydrogenation on Pd/In_2O_3 catalysts as a function of reduction temperature or site covering. (c) The relationship between the desorption energy to the energy barrier for the rate-determining hydrogenation step of ethylene on NiZn alloy catalyst. (d) The change of selectivity to ethylene along with the increase of H_2 to ethyne ratio on Pd_4S/CNF catalyst. [Panel (a) has been reproduced with permission from ref 152. Copyright 2017, Elsevier. Panel (b) has been reproduced with permission from ref 149. Copyright 2019, Royal Society of Chemistry, London. Panel (c) has been reproduced with permission from ref 172. Copyright 2008, AAAS. Panel (d) has been reproduced with permission from ref 333. Copyright 2016, Elsevier.

ity.[214,309,319] However, the results of electronic structure based on conventional ex-situ characterization methods are mostly independent with the reaction conditions, which will lead to the dilemma that the same electronic structure corresponds to different catalytic properties if one overlooks this case.

Another example is the semihydrogenation reaction of alkynes. For liquid-phase autoclave semihydrogenation reactions on Pd-based catalysts, Wang et al. have demonstrated that the overhydrogenation side reaction occurs on low coordinated sites as edge and corner Pd sites, while the facet sites are very selective to substituted alkenes before the full conversion of substituted alkyne.[149,152] The selectivity control is actually determined by the adsorption energy ratio of substituted alkyne to alkene, as shown in Figure 20a. The larger the ratio, the better the selectivity. These conclusions were also supported by other reports.[320−323] This means that the electronic structure modulation for facet sites is not necessary if one does not pursue the complete block of alkene hydrogenation after the full conversion of alkyne. Or, in other words, the electronic structure modulation of the facet Pd sites may well be unrelated to the improved selectivity to alkene before the late reaction stage. For example, several Pd alloy catalysts have showed better hydrogenation selectivity to alkene than monometallic Pd catalysts.[153,161,324−330] The d-band centers and the Pd_{3d} binding energies in XPS will certainly be tuned by the alloy elements to some extent.[331,332] However, both theoretical and experimental results from Wang et al. have confirmed that an alloy of Zn and In is detrimental to the selectivity to alkene (Figure 20b).[149,152] Hence the improved selectivity can only be attributed to the block of the low coordinated Pd sites with alloy elements. Under these circumstances, the alloying-induced modulation of the electronic structure should not be the determining factor, and the related characteristic results is misleading in these two cases. For gas-phase semihydrogenation reaction on Pd-based catalysts, especially for the semihydrogenation of trace acetylene in a large ethylene stream, the criterion of the adsorption energy ratio of acetylene to ethylene is no longer sufficient or complete to design an efficient catalyst, in that the residual acetylene in the local environment over the catalyst surface is not enough to completely occupy the surface sites of the catalyst when the trace acetylene is exhausted. As a result, another criterion involving the ratio of the desorption energy to the energy barrier for the rate-determining hydrogenation step of ethylene is employed, since it is easy to understand that weaker adsorption and more difficult subsequent hydrogenation process help to improve olefin selectivity at first glance (Figure 20c).[172] However, this criterion does not contain any information about the effect of acetylene, which means that the selectivity to ethylene will not be influenced if the trace acetylene is not fed, or in other words, the selectivity to ethylene will not decrease at 100% conversion of the trace acetylene. Obviously, this is not the case in reality, as seen in Figure 20d.[333] Therefore, the related electronic structures

https://doi.org/10.1021/acscatal.2c05141
ACS Catal. 2023, 13, 974−1019

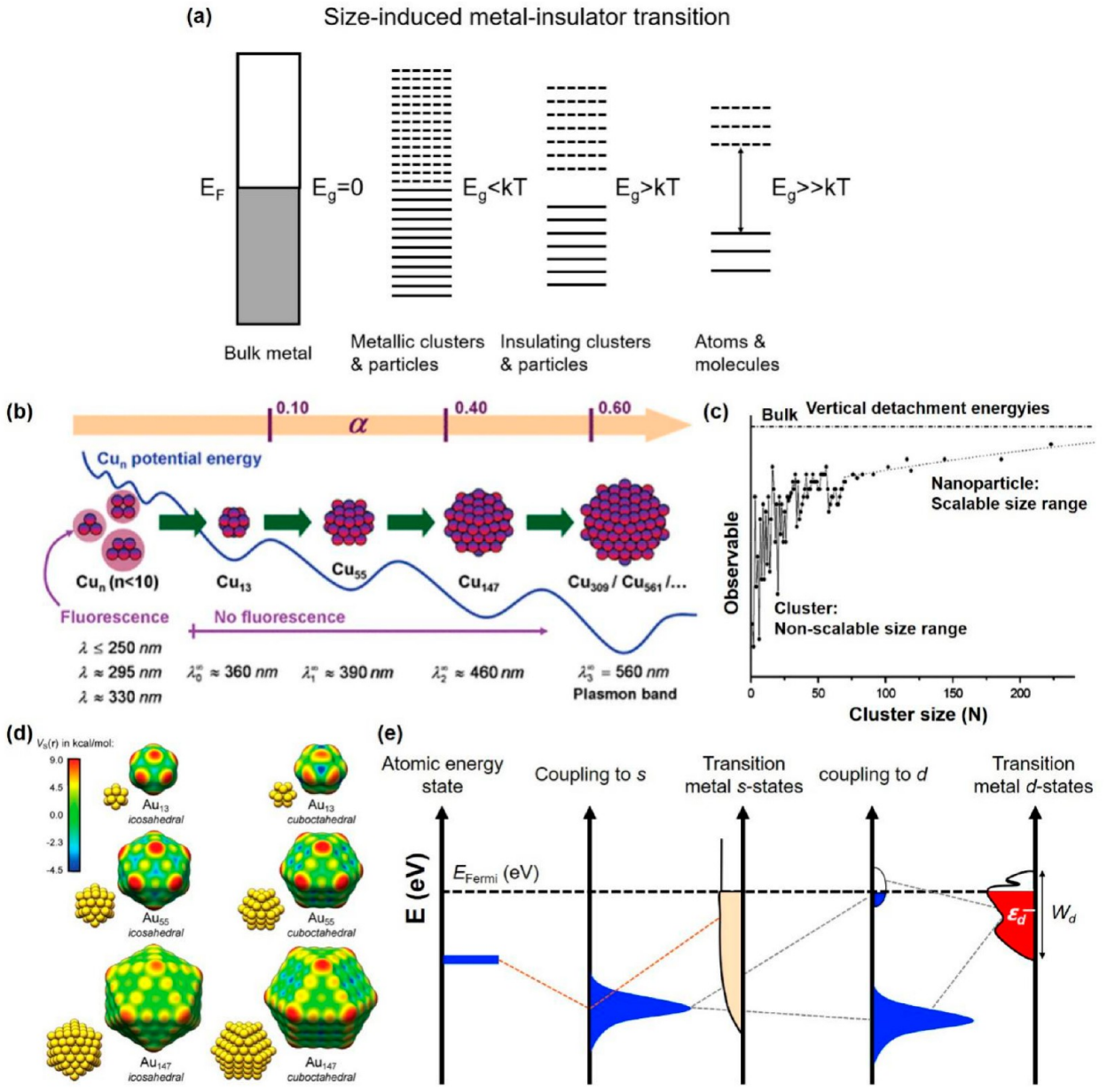

Figure 21. (a) Evolution of the electronic structure, along with the decreasing metal particle size. (b) Schematic picture of the evolution of the copper cluster size with increasing α value. α is defined as moles of $NaBH_4$ added)/(moles of $NaBH_4$ necessary for the stoichiometric reduction of Cu(II) cations. (c) Work function obtained from UPS of Au clusters with different atom number. (d) $V_{S(r)}$ values on the 0.001 Au isodensity surfaces of icosahedral and cubooctahedral clusters of Au_{13}, Au_{55}, and $Au1_{37}$. Color from red to yellow indicates the most positive sites, i.e., the sites most prone to interact with Lewis bases. (e) Schematic diagram illustrating interaction between the adsorbate with the delocalized s-states and localized *d*-states on the metal surface. [Panel (a) has been reproduced with permission from ref 334. Copyright 1999, Wiley−VCH. Panel (b) has been reproduced with permission from ref 344. Copyright 2009, American Chemical Society, Washington, DC. Panel (c) has been reproduced with permission from ref 346. Copyright 1992, American Institute of Physics. Panel (d) has been reproduced with permission from ref 349. Copyright 2017, American Chemical Society, Washington, DC. Panel (e) has been reproduced with permission from ref 352. Copyright 2005, Springer Nature.]

reflecting this criterion are not quite suitable to predict the high selectivity and a more accurate criteria still must be developed.

Although the effect of electronic structure on hydrogenation and even heterogeneous catalytic reaction is not as simple and clear as that of geometric structure, the significant impact on the reaction performance still cannot be ignored. Then some common electronic effects will be briefly introduced in the following. The electronic structure of a metal NP is strongly dependent on its size, especially at the nanoscale (Figure 21a).[94,334] Because of the electronic degeneracy in bulk metal, the electronic energy levels are compressed into bands according to the theory of energy band.[334] In contrast to bulk metal, the electronic energy levels gradually become discrete and even behave as molecular orbitals, due to the confinement of electron wave functions within the dimensions of the particles when decreasing the size of metal particle to the nanoscale and atomic regimes, where a distinctive HOMO−

https://doi.org/10.1021/acscatal.2c05141
ACS Catal. 2023, 13, 974−1019

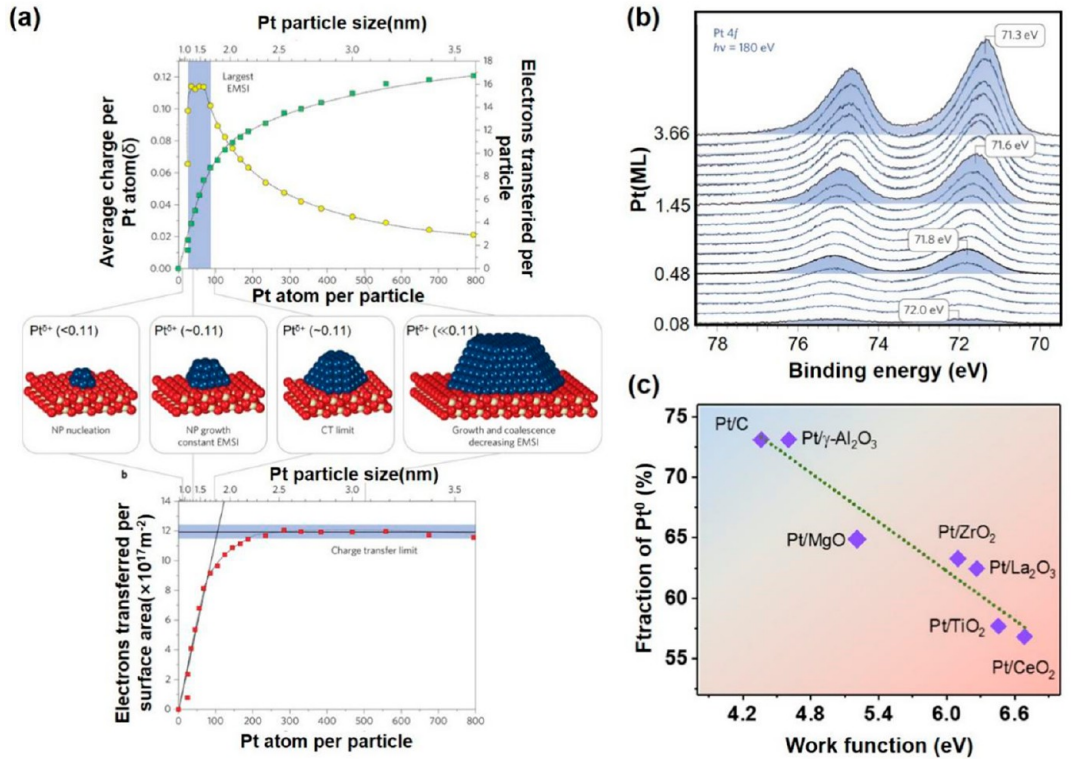

Figure 22. (a) The average electron loss on each Pt atom in Pt particles of different sizes measured by XPS (upper). The relationship between electrons transferred per surface area and the size of Pt deposited on CeO_2 (down). (b) The binding energy evolution of Pt 4f with the size of Pt NPs on CeO_2. (c) Relationship between the charge transfer and the work function of supports. [Panel (a) has been reproduced with permission from ref 370. Copyright 2015, Springer Nature. Panel (b) has been reproduced with permission from ref 370. Copyright 2015, Springer Nature. Panel (c) has been reproduced with permission from ref 117. Copyright 2022, Springer Nature.]

LUMO gap and metallic-nonmetallic transition occur.[94,334,335] This phenomenon is called quantum size effects.[94,302,336,337] The band gap between HOMO−LUMO can be approximately predicted by the Jellium model with eq 4-1:[338,339]

$$E_g = \frac{E_f}{N^{1/3}}$$

where N is the number of the atoms in the metal particle, E_F the Fermi level energy, and E_g the band gap energy, which approximates to the emission band in the photoluminescence spectrum from experiments. Hence, a shift in the fluorescence wavelength is well expected, along with the size modulation metal NPs, and one can also simply deduce the number of atoms of an unknown cluster from a simple photoluminescence spectrum with this formula. In addition, the metal−nonmetal transition is estimated to be pronounced when the size of a metal NP decreases to ∼2 nm, containing ∼300 atoms, as further evidenced by measuring the d-band spin−orbit splitting.[94,340,341] The discreteness of electronic energy levels also induce essential changes in the spectra of metal NPs, especially those related to the valence band, such as X-ray/ultraviolet photoelectron spectroscopy (XPS, UPS),[337,342,343] UV-vis spectroscopy,[344] scanning tunneling spectroscopy (STS),[302,345] etc. Then, these characteristic changes in the spectra can be employed as a descriptor to the change of the electronic structures of the catalyst and, furthermore, are possibly correlated to the catalytic performance. Taking free-standing Cu as an example, as shown in Figure 21b, Cu clusters with an atom number of <13 are photoluminescent.[344] Photoluminescence disappears for larger Cu clusters (0.8−2.0 nm) but a red-shift of UV−visible absorption bands occur as Cu clusters grow in size. Further increasing the size of nanoparticles to 2.9 ± 1.1 nm, the characteristic plasmon band of Cu NPs can be obtained. As for free-standing Au (see Figure 21c), the work function of Au clusters is also closely related to the particle size.[114,346] The work function varies greatly for Au clusters of <30 atoms, while it almost remains constant for the atomicity values greater than 70 atoms (>1.5 nm).

Besides the band gap modulation, the density of surface electrostatic potential (V_S) can also be tuned with the particle size, which forms the σ-hole theory afterward.[347−349] According to the σ-hole theory,[349] as shown in Figure 21d, there would be a maxima of V_S called σ-hole at LCSs of metal NPs when the single-occupied s-orbitals of metal NPs overlap with each other and form the bonding σ-orbitals. Then the density of σ-holes is coincident with that of LCSs. As a result, Brinck et al. suggested that V_S plays a key role to the adsorption affinity of CO and O_2 on the Au catalyst (13−147 atoms) and thereby the (high-temperature) catalytic activity, manifesting the important role of the electronic effect in size-dependent reactions.[349] This scenario is very suitable for Au catalyst in which the d-orbitals are fully occupied. Note that transition-metal active sites with different coordination environments possess different dangling d-orbitals and is critical to the cleavage to the σ-bonds. The nature of the electronic effect behind the coordination number has been elaborated in detail at the end of section 4.1.1. Hence, it will not be discussed here again.

When further increasing the particle size to realize the nonmetal−metal transition, typically above 2 nm, a well-known

https://doi.org/10.1021/acscatal.2c05141
ACS Catal. 2023, 13, 974−1019

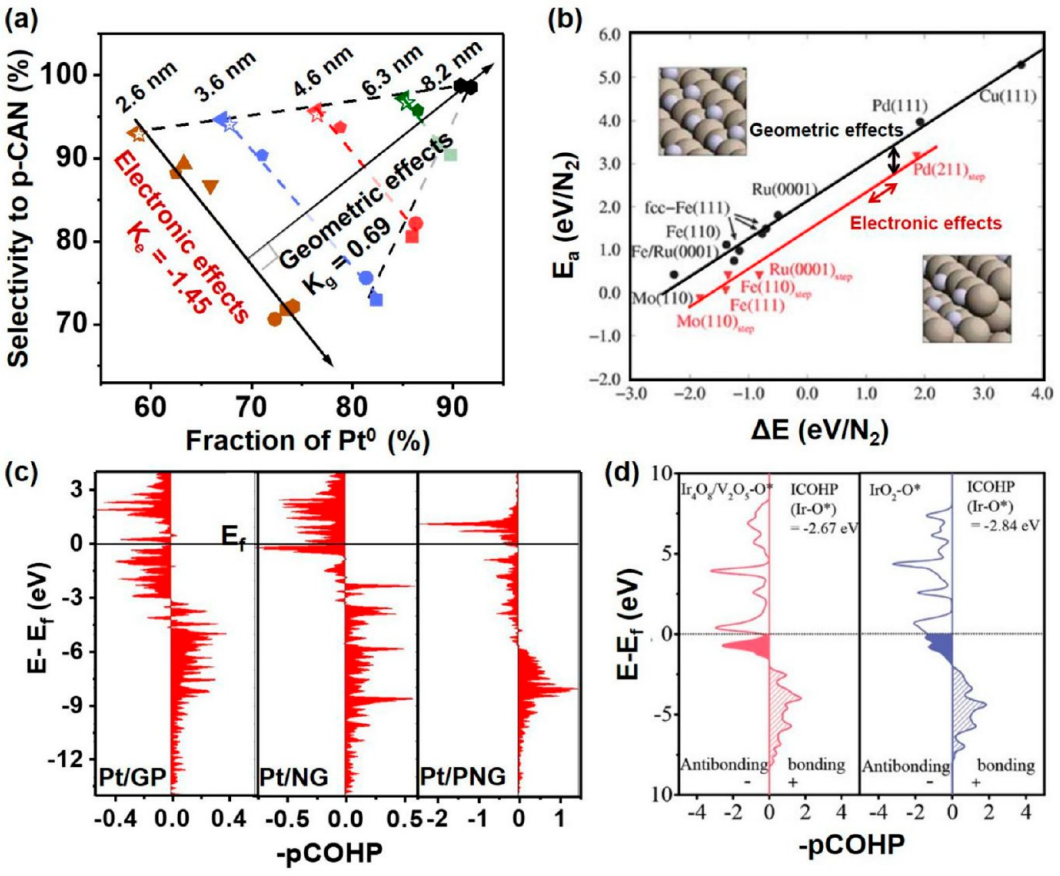

Figure 23. (a) Selectivity of *p*-CAN against the fraction of Pt^0 over different catalyst with various particle sizes of Pt. (b) The BEP relationship for NO dissociation over several stepped (red triangle) and close-packed (dark circle) surfaces. (c and d) *p*COHP curves for the adsorption of Pt NPs on pristine and nitrogen-doped carbon and O* intermediate adsorption on Ir active site for Ir_4O_8/V_2O_5 and IrO_2. [Panel (a) has been reproduced with permission from ref 117. Copyright 2022, Springer Nature. Panel (b) has been reproduced with permission from ref 119. Copyright 2008, Royal Society of Chemistry, London. Panel (c) has been reproduced with permission from ref 371. Copyright 2019, Elsevier. (d) Panel (d) has been reproduced with permission from ref 372. Copyright 2022, Wiley−VCH.

d-band center theory was developed by Nørskov et al. to quantify the reactivity of metal active sites on the basis of electronic effect at the molecular level (Figure 21e).[331,332,350−352] Based on this theory, the *d*-band center, derived from the first moment of the density of states projected onto the *d*-orbitals of the surface atoms, is a good descriptor to measure the ability of the surface metal atoms to bond with an adsorbate and also the ability for bond activation.[294,350,353] The *d*-band center theory has been successfully employed in many hydrogenation-related reactions with single-metal catalysts, such as ammonia synthesis, ethylene hydrogenation, phenol hydrogenation, oxygen reduction reaction, etc.[8,352,354−358] However, the shortcomings arise to this theory in that the d-band center carries no information of the band shape or dispersion. As a result, *d*-band center-based models, which all rely on surface-localized features, are unable to fully account for the asymmetries and distortions in the electronic structure brought on by alloying.[349,359−364] Revised d-band center theories are then developed, which involve shape-induced convolution effects,[365] polarization effects caused by magnetism,[366] and perturbations in both the substrate and adsorbate electronic states upon interaction.[367] In any case, the great thing about the d-band center theory is that it provides a simple method to deal with the relationship between complex band structures and the reaction performance, which indeed improves the confidence of researchers in the study of electronic structure effects.

When metal active sites are loaded on supports, charge transfer between metal active sites and the support becomes inevitable, because of the balance between their Fermi levels.[368] The charge transfer will alter the electronic structure, distribution, and stability of metal active sites, which will finally affect the catalytic performance.[369] The charge transfer is strongly dependent on the size of the metal active sites. Libuda et al. examined the size impacts of metal active sites on the electronic metal−support interaction (EMSI) between Pt and CeO_2 with synchrotron-radiation photoelectron spectroscopy, ranging from clusters to nanoparticles.[370] According to Figure 22a, the strongest electrical metal−support interaction is seen in Pt nanoparticles with 30−70 atoms, because they have the highest positive charge on each Pt atom. The charge transfer approaches its intrinsic limit for larger particles, possibly caused by the Fermi level pinning when the size of metal NPs increases further. This means the radius on charge modulation of the metal NPs by supports is also limited. For smaller particles (<30 atoms), charge transfer is partially suppressed by nucleation at defects and the shrink of the electron orbitals.[370,371] The charge transfer for metal NPs of varied sizes can also be reflected by XPS (Figure 22b), which reveals a typical shift to higher binding energies with the decrease of the

https://doi.org/10.1021/acscatal.2c05141
ACS Catal. 2023, 13, 974−1019

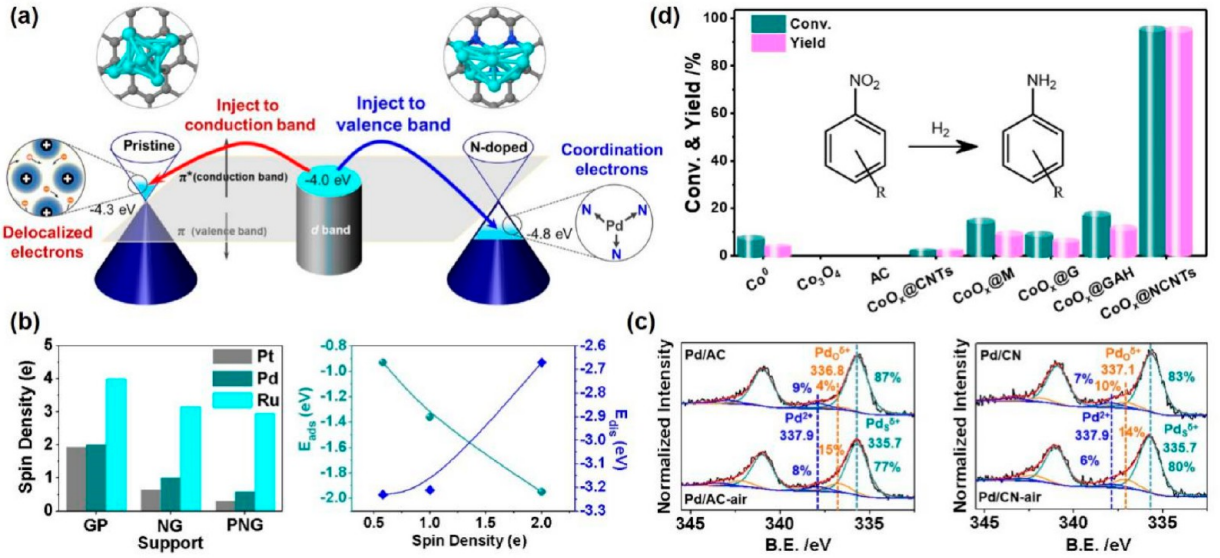

Figure 24. (a) Model for electron transfer between metal NPs and carbon supports. (b) The spin density change of the supported metal NPs after nitrogen doping of the carbon support and the relationship between O_2 adsorption/dissociation and spin density on metal NPs. (c) The ratio of metallic Pd for as-reduced and exposed catalysts. (d) The obvious increased activity for nitrobenzene hydrogenation on nitrogen stabilized Co catalyst. [Panels (a)−(c) have been reproduced with permission from ref 371. Copyright 2019, Elsevier. Panel (d) has been reproduced with permission from ref 377. Copyright 2015, American Chemical Society, Washington, DC.]

particle size.[118,370] The charge transfer can also be tuned by supports of different types. For metal NPs of a certain particle size, the degree of charge transfer is actually charged by the work function of the support (Figure 22c).[117] A linear relationship with negative slope between the remained fraction of metallic Pt and the work functions of supports has been found for Pt NPs on various supports, indicating that more electrons are transferred to a support with larger work function.

The charge-transfer limit indicates that the intensity of the electronic modulation from supports should be considered. To solve this problem, a series of parameters and suitable probe reactions should be carefully controlled and selected. Then it is necessary to find an appropriate experimental physicochemical parameter quantitatively reflecting the change of electronic structure and correlate it with the catalytic performance. Wang et al. offered a typical example for the selective hydrogenation of halogenated nitrobenzene on supported Pt catalysts.[117] Through size- and shape-controlling colloidal methods and mild surfactant-removing strategy, supported Pt catalysts with clean surface and similar particle size and morphology were obtained over various supports. DFT calculations suggested that the dehalogenation side reaction will not preferentially occur at the interface sites compared with the low coordinated Pt sites. Then the interferences of interface factors can be eliminated. As shown in Figure 23a, results showed that the selectivity of halogenated aniline was linearly related with the remained fraction of metallic Pt on various supports with a slope (K_e) of −1.45. This linear relationship represents the electronic effect from the support, and the slope value further represents the relative intensity.

Perhaps the most challenging work is to decouple the entangled electronic and geometric effects. One option is the selective poisoning or deposition method, but it still faced the accuracy problem and the support effect from deposit sediments.[118,149] Nørskov and co-workers tried to separate the two effects based on the BEP relationships of eq 4-2

$$E_a = \alpha \Delta E_{react} + \beta \qquad (0 < \alpha < 1) \tag{4-3}$$

where E_a represents the energy barrier, and ΔE_{react} is the reaction energy and represents the intrinsic reactivity of a surface. Then, α represents the electronic effect along the reaction coordinate and β represents the purely geometrical effect reflecting the structure of the transition state (TS) of a catalytic reaction (Figure 23b).[119] Then the value of α and β indicates the structure-sensitive dependencies of a reaction. Actually, the key for this challenge is to identify the relationship between the state function of the electronic effect and the size or morphology variation of metal NPs. By extending the size of Pt NPs, Wang et al. surprisingly found that the K_e values are the same for Pt particles ranging from 2.6 nm to 8.2 nm.[117] This means that the intensity of the entangled electronic effect, derived from the change of the energy bands of metal NPs and the charge transfer between metal NPs and supports for metal NPs of different sizes, is independent of the particle size of Pt of controlled shapes. Since the electronic and geometric effects are independent with each other in principle, they should be orthogonal with each other from a mathematical or physical point of view. Then the intensity of the geometric effect is calculated to be −0.69 (K_g, Figure 23a), and the electronic and geometric effects is then quantitatively decoupled. When switching to the new set of rectangular axes involving the state functions of the electronic and geometric effects, the specific relative values for these two effects can then be obtained by projecting the traditional fitted size effect lines to the new axes. Back to the illustration of the BEP relation from Nørskov and co-workers, one can suspect that it would be more reasonable to project β to the vertical of the fitted BEP lines to get a "pure geometric effect". As a result, the two types of decoupling would be mutually unified.

One thing that has been overlooked for most researchers until now is that the charge transfer and Fermi level regulation between metal active sites and the support will induce non-

https://doi.org/10.1021/acscatal.2c05141
ACS Catal. 2023, 13, 974−1019

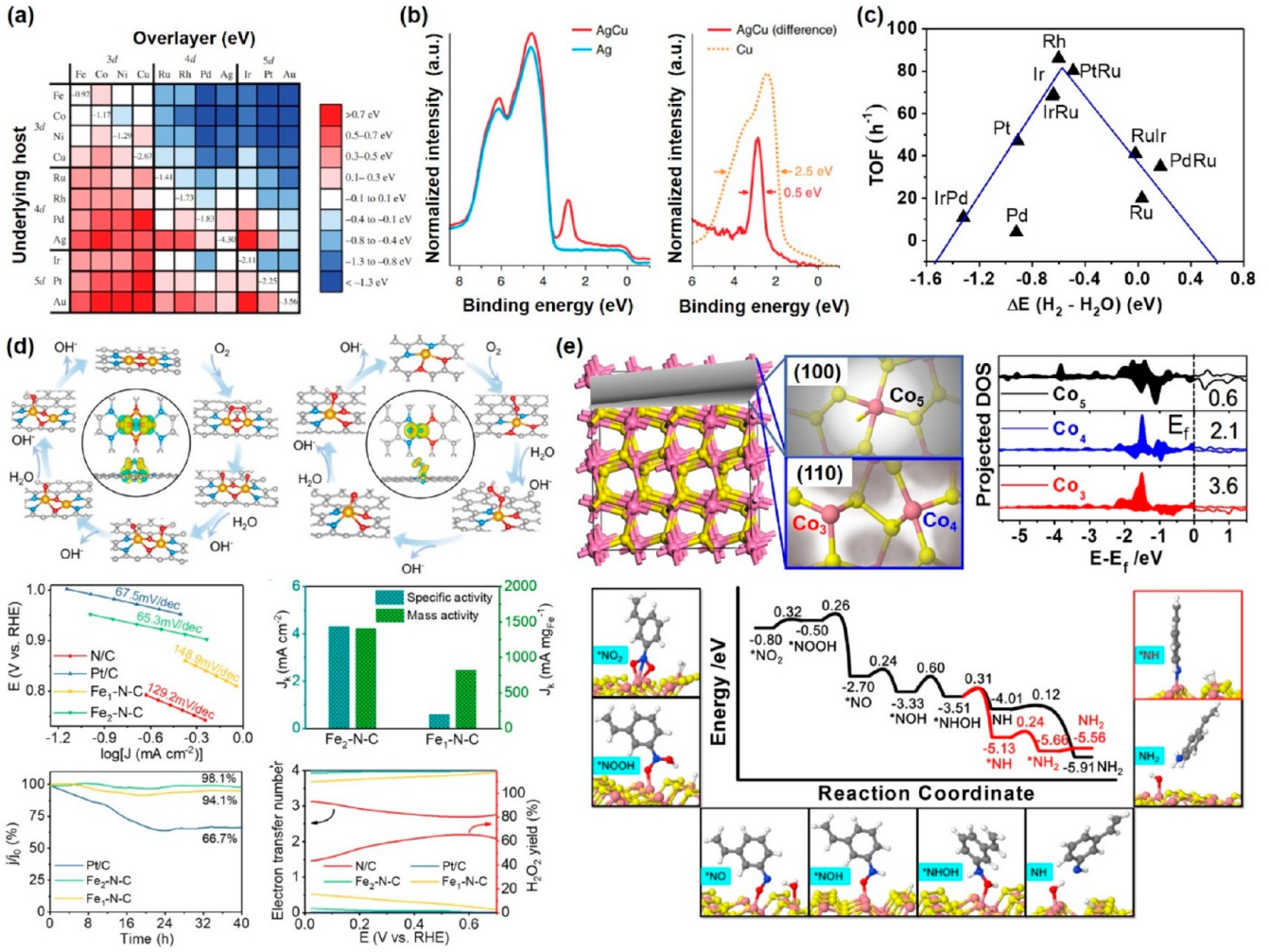

Figure 25. (a) Calculated shifts in the *d*-band centers for several overlayer structures. The shifts are given relative to the *d*-band center for the pure metal surface. (b) Measured valence photoemission spectra ($h\nu$ = 150 eV) of an AgCu alloy reveals the narrow Cu 3d states at a binding energy of ∼2.5 eV. The difference spectrum of AgCu and Ag, plotted with a Cu reference spectrum, demonstrate that the Cu 3d states in AgCu are one-fifth the width they are in bulk Cu. (c) Catalytic activity for selective hydrogenation of benzoic acid plotted as a function of the differential value of dissociation energies or adsorption energies between H_2 and H_2O (ΔE) on various metal catalysts calculated from DFT. (d) ORR reaction mechanisms and differential charge densities for O_2 adsorption on $Fe_2N_4O_2$ and FeN_2O_2. C, N, Fe, and O atoms are presented by gray, blue, orange, and red spheres, respectively. The blue and yellow isosurfaces stand for the negative and positive charges, respectively. The isosurface of charge density is set to 0.005 eÅ^{-3}. The corresponding Tafel curves, specific activity and mass activity, H_2O_2 yield and electron transfer number, and stability evaluation test on Fe_2 dimers and Fe_1 catalysts, respectively. (e) Model and spin density for Co active sites of different coordination on CoS_2, and the reaction mechanism for the selective hydrogenation of nitrostyrene on Co_3−Co_4 active site pair. [Panel (a) has been reproduced with permission from ref 389. Copyright 2015, Wiley−VCH. Panel (b) has been reproduced with permission from ref 370. Copyright 2018, Springer Nature. Panel (c) has been reproduced with permission from ref 393. Copyright 2017, Royal Society of Chemistry, London. Panel (d) has been reproduced with permission from ref 398. Copyright 2022, Wiley−VCH. Panel (e) has been with permission from ref 41. Copyright 2018, Royal Society of Chemistry, London.]

negligible occupied antibonding orbitals below the Fermi level of the catalyst.[371−373] These occupied antibonding orbitals will weaken the bonding strength between the adsorbates and the catalyst or between active sites and the support, as shown in Figures 23c and 23d.[371,372] Disappointingly, the detailed discussion of the reaction process of these occupied antibonds are rare, although this phenomenon may cause a different mechanism for bond making and cleavage beyond the traditional Newns−Anderson−Grimley adsorption model.

The charge transfer can also affect both the thermal and chemical stability of supported metal NPs. It has been well-accepted that metal NPs supported on reducible metal oxides generally are more thermally stable than those on irreducible ones, which is in accordance with the degree of charge transfer.[370] This empirical rule also applies to the carbon support, but there is something different.[371] Carbon support, especially for active carbon or graphene, can be roughly considered as metallic, because of their good conductivity. Then the electrons transferred from metal NPs are injected into the conduction band of the carbon support, as shown in Figure 24a, forming many occupied delocalized antibonds with carbon support.[371] As a result, metal NPs are easy to migrate, agglomerate, and even detach from the support. However, when doping with pyridinic nitrogen, the band gap emerges. The electrons transferred from metal NPs are instead injected into the valence band of the carbon support, forming localized dative bonds with carbon support. Then the thermal stability is enhanced in numerous reactions such as hydrogenation,

https://doi.org/10.1021/acscatal.2c05141
ACS Catal. 2023, 13, 974−1019

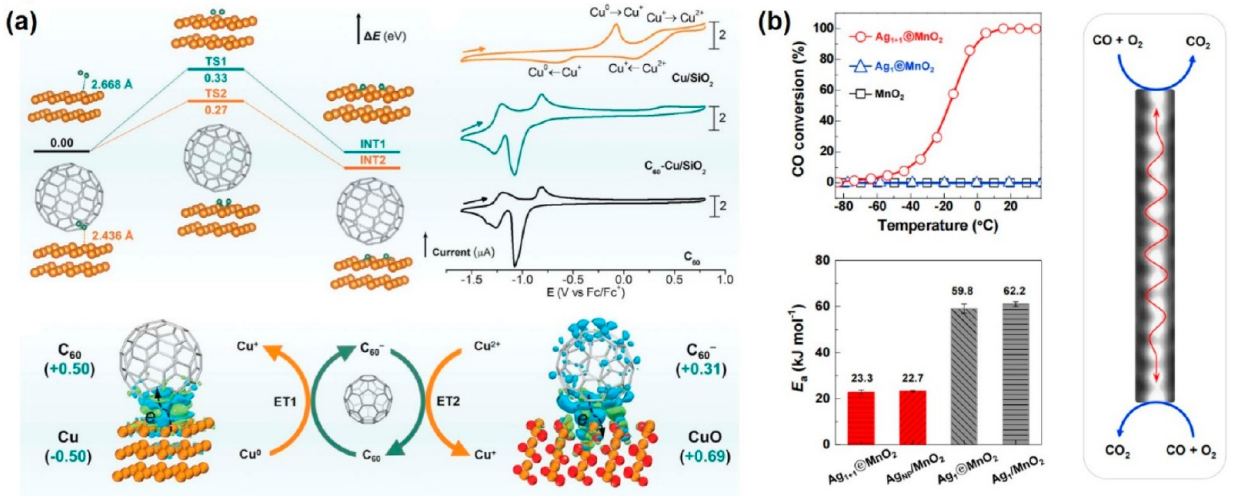

Figure 26. (a) Comparison of H_2 activation and cyclic voltammogram on C_{60}-Cu/SiO_2 and Cu/SiO_2 catalysts. Calculation results of Bader charges for C_{60}-Cu and C_{60}-CuO surface interaction systems also are shown. The red and orange balls represent O and Cu atoms, respectively. ET represents electron transfer. The plus and minus signs represent the degree of the Bader charge. The green and blue areas with isosurface contours denote electron accumulation and electron depletion, respectively. (b) CO conversions as a function of temperature and apparent energy barrier on $Ag_{1+1}©MnO_2$, $Ag_1©MnO_2$, and MnO_2. Also, a schematic representation of the electron delocalized mechanism in low-temperature CO oxidation occurring at two ending active sites of the Ag metallic wire are shown. A scanning transmission electron microscopy image of part of the Ag wire was used. A wave-type double arrow represents the electron shuttling between two ending active sites. [Panel (a) has been reproduced with permission from ref 399. Copyright 2022, AAAS. Panel (b) has been reproduced with permission from ref 400. Copyright 2022, Elsevier.]

oxidation, coupling, etc. On the other hand, nitrogen doping also decreases the spin polarization of metal NPs, preventing it from being oxidized by the oxidants such as oxygen molecule (Figure 24b). That is why the metallic components increase after loading on nitrogen-doped carbon supports (Figure 24c).[374−378] This function is particularly important for early transition metals such as Fe, Co, Ni, etc., which greatly enhance the catalytic activities such as hydrogenation of nitrobenzene (Figure 24d) and electrocatalysis.[377,379−388] It is notable that pure carbon supports can also prevent metal NPs from oxidizing when coating on the surface of metal NPs.

Apart from the modulation from support, alloying is also widely accepted to be effective to tune the electronic structure of metal NPs. For example, the *d*-band center can shift down by >1.3 eV when different alloy elements are employed, which can, in turn, modify the activity of metal NPs (Figure 25a).[332,389] Beside the entire energy band modification, alloying can also turn the target metal atom to a specific electronic state, e.g., pseudo-free single-atom state.[390,391] Greiner and Jones reported a single-atom AgCu alloy catalyst, where the Cu *d*-states are almost unperturbed from their free-atom state (Figure 25b).[390] In addition, in situ XPS demonstrates that this unusual electronic structure can be maintained steady under real reaction conditions. The narrow *d*-state makes the adsorbate state splitting into bonding and antibonding orbitals easier. Although the current single-atom AgCu alloy catalyst exhibits only a 0.1 eV smaller energy barrier than the bulk Cu in methanol reforming, this phenomenon offers a design approach that may well result in alloy catalysts with unprecedented performance. Despite all this, the full illustrating and correlating of the modification of the electronic structure by alloying to catalytic performance are still troublesome. In many cases, the electronic structure change by alloying acts on several reaction processes. A better approach is to divide the analysis process into two steps. The first step is to find an energy descriptor corresponding to the electronic effect, and the second step is to find the relationship between the energy descriptor and the catalytic performance. Obviously, the physicochemical principles between electronic effects and energy descriptors in the first step are very obscure, while the work in the second step is much simpler. The advantage of such treatment is that even if the mechanism behind the first step is not clear, it will not affect the reasonable results given in the second step, so as to find out the rule of alloying on the catalytic performance. For example, the alloying of noble metal catalysts actually tuned the competing adsorption of H_2 and H_2O to achieve a higher activity, based on the Sabatier principle in the selective hydrogenation of benzoic acid, rather than the d-band center, energy barrier of the rate-determining step, or the binding strength of any of the adsorbates alone (Figure 25c).[392,393] In addition, machine learning has recently been used to correlate a large number of electronic structure data and catalytic activity on the basis of calculation and experimental results. Through reasonable data extraction, feature engineering and logical reasoning, it is possible to extract the key influencing factors from complex electronic structure information.[394,395] Another easily overlooked situation is the indirect electronic modulation by noble metals. For example, reducible metal oxides can be richer in electrons when loaded noble metal atoms are exposed in a hydrogen atmosphere.[396,397] The reason lies in that noble-metal species enhance the hydrogen dissociation activity and increase content of oxygen vacancies on the surface of the support accordingly. The increased oxygen vacancies as active sites again enhanced the catalytic performance such as the selective semihydrogenation of acetylene.

When the size of the metal NPs decreases to single-atom site, the construction of an electronic structure as required becomes more convenient. The activity of early-transition-metal single-atom catalysts is always limited by insufficient receiving sites for diatomic molecule activation. In oxygen reduction reaction, adsorbed O_2 on Fe_2 dimers with $Fe_2N_4O_2$

https://doi.org/10.1021/acscatal.2c05141
ACS Catal. 2023, 13, 974−1019

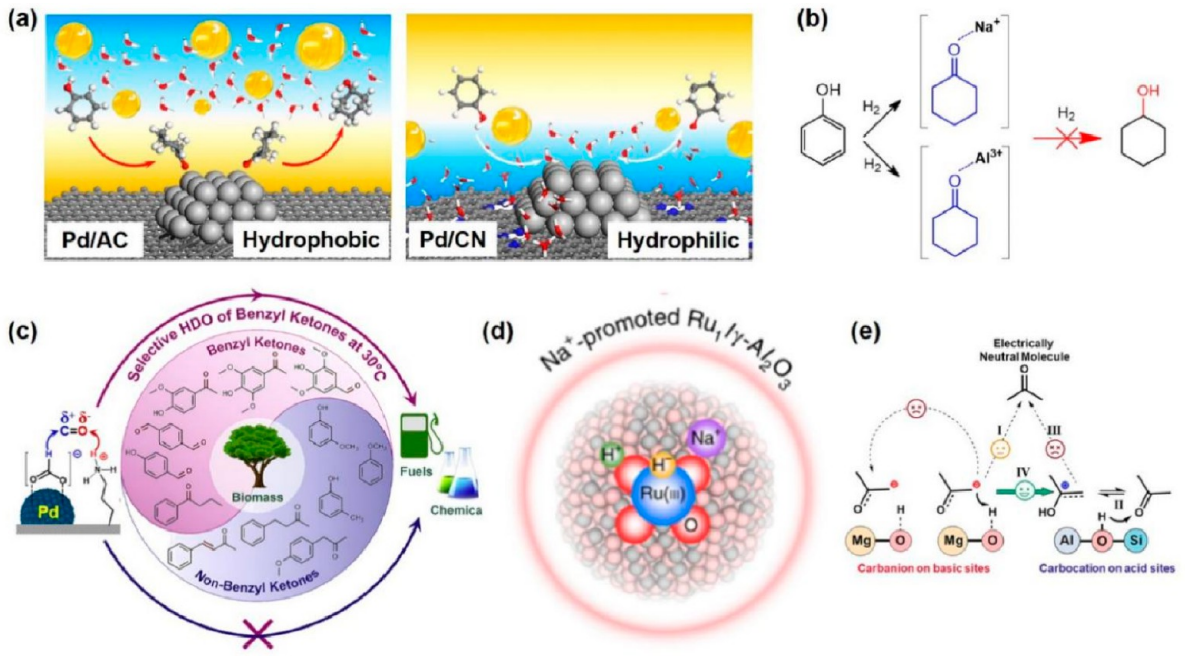

Figure 27. (a) Hydrophilic regulation and (b) blocking the oxygen of the C═O bond in cyclohexanone with additives to prevent overhydrogenation of phenol. Methods to the electrical regulation of intermediates include (c) forming H^+ species, (d) forming H^- species, and (e) generating metastable carbocation and carbanion ion-pair intermediates. [Panel (c) has been reproduced with permission from ref 410. Copyright 2021, Elsevier. Panel (d) has been reproduced with permission from ref 411. Copyright 2020, Springer Nature. Panel (e) has been reproduced with permission from ref 412. Copyright 2021, Elsevier.]

structure exhibits stronger electron depletion between the O−O bond- compared with that on Fe_1 single-atom counterpart with FeN_2O_2 structure as seen in Figure 25d, indicating that the bond strength of O−O on $Fe_2N_4O_2$ is diminished to a greater deal.[398] As a result, the cleavage of the remaining O−O bond will be easier on Fe_2 dimers, which is favorable for the inhibition of H_2O_2 formation. More important is the fact that more electron transfer on Fe_2 dimers does not cause higher binding energy of O_2 and other oxygen species, because of the higher energy level overlap between the p-bands of adsorbed O_2 and the *d*-bands of $Fe_2N_4O_2$, as shown in Figure 25d. The unique role of Fe dimers in activating diatomic O_2 molecules avoids the usual formation of *OOH intermediates. As a result, Fe_2 dimers showed much higher (7 times) specific activity than that of Fe_1 counterparts for oxygen reduction reaction. In the selective hydrogenation of substituted nitrobenzene on CoS_2, Co_3−Co_4 active site pairs with different electronic structures and functions were generated and displayed the synergic effect (Figure 25e).[41] The activity of Co_3−Co_4 active site pairs originates from the larger spin density. Low-coordinated Co_3 site is occupied by 3-nitrostyrene and Co_4 site by H_2 as 3-nitrostyrene binds stronger than H_2. Then the hydrogenation proceeds inside the synergic active site pair. Notably, the adsorbed H_2 on Co_4 maintains its molecular mode, rather than dissociation, which enhances the hydrogenation activity of the catalyst.

It can be seen from the above discussion that researchers in the field of thermal heterogeneous catalysis are usually accustomed to paying attention to the results of electron transfer, rather than the process or even kinetics of electron transfer, since they believed that the velocity of electrons is always much higher than that of atoms, because of their huge mass distinction. In contrast, it is usually very important for electrocatalysis, because the transmission of electrons will inevitably cause a voltage drop, thus reducing the energy efficiency. Two recent works may be a turning point to address the importance of this point.[399,400] Xie et al. showed that fullerene can serve as an electron buffer in the hydrogenation of dimethyl oxalate over a C_{60}-Cu/SiO_2 catalyst at ambient pressure and temperatures of 180−190 °C with a glycol yield of up to 98% ± 1%. The addition of fullerene is favorable to hydrogen activation and the valence recycle of Cu during the reaction (Figure 26a).[399] Fullerene can act as an electron buffer for a Cu/SiO_2 catalyst to eliminate charge accumulation caused by the poor conductivity. By fabricating two types of MnO_2-encapsulated metallic Ag single-atom-site catalysts with one or two ending Ag atoms of each wire exposed on surfaces, Tang et al. found that only the catalyst with both ending Ag atoms exposed can trigger low-temperature CO oxidation, which provided unequivocal evidence that the interaction between active sites is possible upon eligible electron conducting (Figure 26b).[400] These results indicated that effective communication between metal and supports or among metal active sites might be universal in thermal heterogeneous catalysis.

The above discussion is based on the modulation of the electronic structure of the catalyst itself. Actually, it is also effective to modulate the noncovalent electronic interaction with reactants and regulate the electrical properties of the intermediates. For phenol-selective hydrogenation to cyclohexanone, the key is to inhibit the further hydrogenation of cyclohexanone to cyclohexanol. One way to suppress the overhydrogenation is to prevent the adsorption of hydrophobic cyclohexanone by increasing the hydrophilicity of the catalyst, as seen in Figure 27a, which has been confirmed by the nitrogen doping of carbon-based supported Pd catalyst.[354,401−403] The selectivity of cyclohexanone reached >99% at >99% conversion on Pd/mpg-C_3N_4 and Pd/

https://doi.org/10.1021/acscatal.2c05141
ACS Catal. 2023, 13, 974−1019

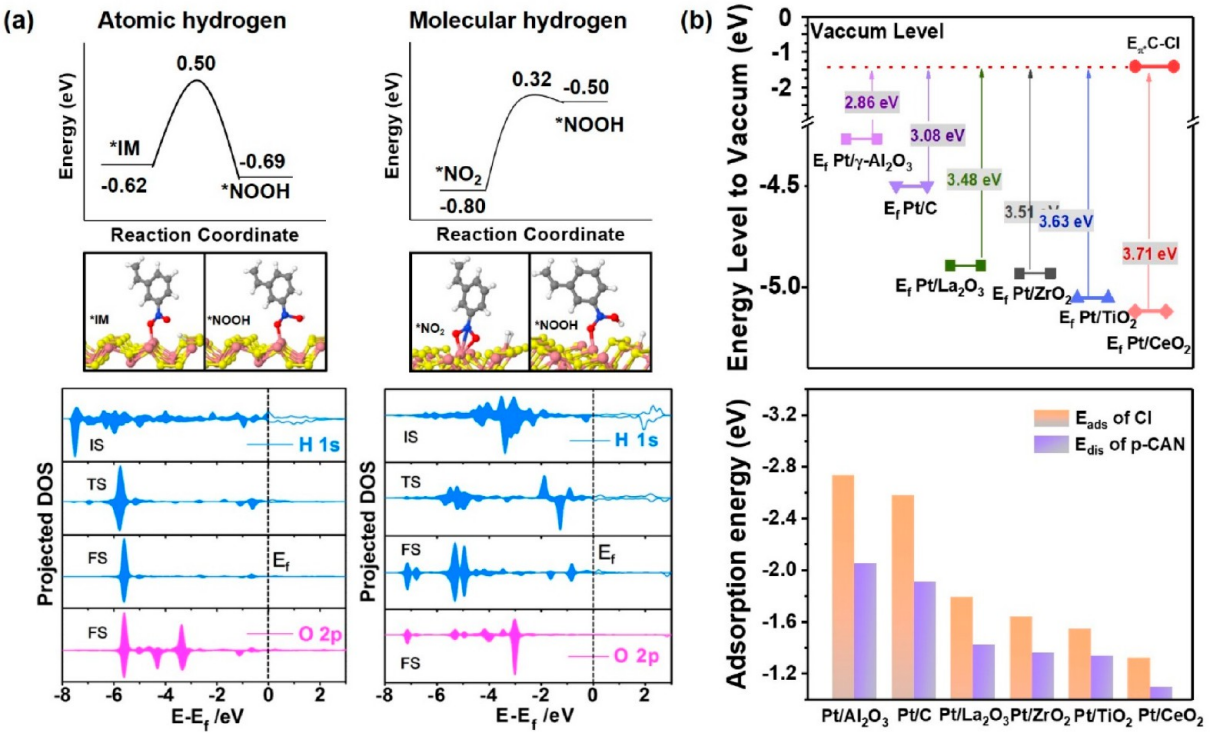

Figure 28. (a) Energy profiles of the first-step hydrogenation of nitrostyrene with atomic hydrogen and chemisorbed molecular hydrogen, respectively. (b) Calculated energy gap between the π^*-antibond (LUMO) of *p*-chloroaniline (p-CAN) and the Fermi level of various Pt catalysts of different supports. And the calculated adsorption energy of Cl atom and dissociation energy of p-CAN on various supported Pt catalysts. [Panel (a) has been reproduced with permission from ref 41. Copyright 2018, Royal Society of Chemistry, London. Panel (b) has been reproduced with permission from ref 117. Copyright 2022, Springer Nature.]

CN.[374,375] However, the selectivity only gave 71% at 98% conversion on commercial Pd/C.[404] This approach is also rather effective to other reactions, particularly those involving two different polarities. By grafting or just physically mixing hydrophobic alkyl compounds to the catalyst surface, the efficiencies for Fischer−Tropsch synthesis,[405] methane oxidation to methanol,[406] etc., have made a breakthrough. Another way is to block the oxygen of the C═O in cyclohexanone with additives as seen in Figure 27b. Han et al. reported both excellent conversion and selectivity for phenol hydrogenation by using a dual-supported Pd Lewis acid catalyst, in which the Lewis acid (Al^{3+})-base (C═O in cyclohexanone) interaction inhibits further hydrogenation to cyclohexanol.[407] Similar results were also found with alkali promoters that form the "−C═O−Na−" conformation and achieves >97% selectivity at >99% conversion for the continuous hydrogenation of phenol on a fixed-bed reactor within 1200 h with a Na−Pd/Al_2O_3 catalyst.[408,409] Sometimes, the electrical regulation of intermediates will also gain dramatic results, as seen in Figures 27c−e. By constructing a (formic acid)−Pd/HPC-NH_2 system, benzyl ketones are effectively recognized and hydrogenated in a mixture of crude lignin-derived oxygenates with the H^+/H^- species generated from the decomposition of formic acid.[410] A TOF of 152.5 h^{-1} at 30 °C for vanillin upgrading was achieved, which is 15 times higher than that in traditional HDO processes (~10 h^{-1}, 100−300 °C). The group recognition activation and high activity under mild conditions proposed a green route to produce biofuels or chemicals from only biomass. Zheng et al. also demonstrated that decorating Ru_1/Al_2O_3 with Na^+ fascinates the heterolytic splitting of H_2 into hydride ($M-H^{\delta-}$) and proton ($O-H^{\delta-}$) species and promotes the hydrogenation of acetone by stabilizing the negatively charged intermediates and transition states (TSs).[411] The tradeoff between selectivity and activity for C−C coupling was overcome after generating metastable carbocation and carbanion ion-pair intermediates by developing oxide−zeolite composite catalysts with spatially separated acid and basic dual sites.[412] A productivity of 1020 mg g_{cat}^{-1} h^{-1} and an isophorone yield of 41% with a lifetime of >1500 h was achieved on an optimal catalyst with acetone as a substrate, while the counterpart usually suffered from poor stability and inferior yield of isophorone (stable productivity <200 mg g_{cat}^{-1} h^{-1}).

Note that the discussion of electronic effects requires special caution, because there is no complete definition for the description of electronic structure. When electronic structure is used as an independent variable, its manifestations are diverse and often closely related to the observation perspective of the researchers. In theory, researchers can define any electronic structure descriptor and discuss its impact on chemical reaction or catalytic performance. However, many electronic structure descriptors are intertwined.[117,118] The change of one electronic structure often leads to the linkage of a variety of other forms of electronic structures. Therefore, one must be very careful when associating the catalytic performance with the electronic structure. It is easy to get an illusion because they are not one to one. In addition, changes in the geometric structure of the catalyst will also cause changes in the electronic structure. These changes in the electronic structure may also appear only as an accompanying result or a spectator in the reaction, without causing any changes in the catalytic performance. Under these circumstances, if other factors, such

https://doi.org/10.1021/acscatal.2c05141
ACS Catal. 2023, 13, 974−1019

as the change of catalyst geometry, are ignored and the cause is forcibly attributed to the electronic effect, wrong conclusions would be given. Another thing to note is the sensitivity of changes in energy and catalytic performance to electronic structure effects. From the reported results, the two do not have a 1:1 numerical correspondence. On the contrary, this sensitivity will vary with different electronic structure parameters, and, in some cases, it is rather low, as seen in Figure 28. For instance, the energy barrier for the first hydrogenation step on 3-nitrostyrene requires only 0.32 eV with molecularly adsorbed H_2 on the Co_4 site of CoS_2, while ~1 eV must be driven to break the bonding σ_g state of H_2 by injecting electrons from the *d*-band of Co_4 to the antibonding state of H_2 (Figure 28a).[41] This means that a large energy shift in the *d*-band will cause only a small change in energy barrier. Similar results have also been found in the selective hydrogenation of halogenated nitrobenzene on supported Pt catalysts and the direct dehydrogenation of alkanes on carbon catalysts, in which the energy-level gaps between the LUMOs of substrates and the HOMOs or Fermi levels of the catalysts are much larger than the activation barrier or the dissociation energy of one specific bond (Figure 28b).[117,413] Therefore, correlating the catalytic performance to tiny a change in the electronic effect will sometimes be unconvincing.

5. SUMMARY AND PERSPECTIVE

In this paper, we summarized the geometric and electronic effects involved in selective hydrogenation. Since the adsorption and activation of reactants are generally the prerequisite for the hydrogenation reaction, we first discussed the homolytic and heterolytic cleavage mechanisms for hydrogen activation and the reaction conditions under which they occur, with special emphasis on the difference between the heterolytic cleavage mechanism and the homolytic cleavage-spillover processes, which is a misunderstanding that researchers are prone to fall into. At the same time, the selective hydrogenation of alkynes and unsaturated ketones has two typical reactions, and the adsorption modes of reactants and intermediates on the catalyst surface are introduced. Then we discussed the reaction kinetics of the hydrogenation reaction and noted that the relative abundance of reaction species on the catalyst surface had an important impact on the reaction performance, which is one of the key focus points for catalyst design. After the introduction of the above basic knowledge, the geometric and electronic effects in catalytic hydrogenation were discussed respectively in detail. In the section that addresed geometric effect, surface coordination or geometric effect and spatial consistency and matching effect were introduced. The catalyst design concepts derived from the structural sensitivity analysis methods based on the chemical bond type and the reaction kinetics curve are completely different for selective hydrogenation. The electronic effect principle behind the surface coordination or steric effect is discussed. In the discussion of spatial confinement and matching effect, the influence of hard and soft confinement based on pore structure and surface ligands on the catalytic performance were classified. In the section of electronic effect, two typical examples were first introduced to highlight the huge risks of electronic effect analysis. Then, several classical electronic effect theories like the energy band theory, quantum size effect, *d*-band center and σ-hole theory, as well as the emerging electron delocalization mechanism, were discussed one by one. Moreover, methods to modulate the electronic effect, such as electronic metal−support interaction (EMSI), alloying, catalyst polarity control, intermediate polarity, and electrical regulation, were presented respectively. At last, we also showed the latest research progress of decoupling the geometric and electronic effects, because of the fact that the separation of these two entangled effects has always been the focus in this field.

Although encouraging advances have been made in the study of geometric and electronic effects in selective hydrogenation reactions, there are yet some challenges to be addressed:

(1) At present, the control of catalytic hydrogenation performance is mainly focused on the geometric and electronic structure of the catalyst itself. In the future, more attention should be paid to the geometric and electronic structure characteristics of the functional groups in the reactant itself. And the means of group recognition hydrogenation should be developed to realize the targeted, rather than preferential, transformation of specific functional groups against several reducible groups, which is somehow familiar with the concept of molecular recognition in supramolecular and separation fields.

(2) The regulation of geometric and electronic structure effects is essentially the modulation of the adsorption, as well as the activation and transformation of reaction species. Therefore, more attention should be paid to the relative abundance of each intermediate, the regulation of the physicochemical properties of active intermediates, as well as the development of short-lived instantaneous detection methods for intermediates.

(3) Heterogeneous catalytic asymmetric hydrogenation has been developed for decades, but its progress is still relatively slow. In the future, we should make bold innovations in theory and experimental means. For example, methods can be developed to break the Sabatier principle and existing LH reaction mechanism.

(4) Traditional catalyst development methods face the problems of low efficiency, long cycle, and low success ratio. In recent years, high-throughput screening, automatic synthesis, machine learning, and other efficient research methods have emerged in materials, biology, energy, organic synthesis, and other fields. Although the influencing factors of heterogeneous catalysis are complex, the application of automation, high-throughput, and artificial intelligence in this field is the trend of the times. Researchers must combine the specific conditions of heterogeneous catalysis to develop suitable automatic and intelligent means.

(5) As a long-term core topic in the study of catalytic structure−performance relationships, the decoupling of geometric and electronic structures has been widely concerned by researchers. However, one must recognize that most of the current research in this field, such as the discussion of size and electronic effects, is only a projection under special circumstances, which is difficult to completely be separated from each other. In the future, based on the inner physical characteristics that each independent factor in the structure−performance relationship is orthogonal to each other, a complete structure−performance relationship equation is eager to be constructed by combining mathematical operations such as dot product, cross product, etc., and a methodology for the analysis of heterogeneous structure−performance relationship is expected to be created accordingly.

https://doi.org/10.1021/acscatal.2c05141
ACS Catal. 2023, 13, 974−1019

AUTHOR INFORMATION

Corresponding Author

Yong Wang − *Advanced Materials and Catalysis Group, Center of Chemistry for Frontier Technologies, State Key Laboratory of Clean Energy Utilization, Institute of Catalysis, Department of Chemistry, Zhejiang University, Hangzhou 310028, People's Republic of China;* orcid.org/0000-0001-8043-5757; Email: chemwy@zju.edu.cn

Authors

Shanjun Mao − *Advanced Materials and Catalysis Group, Center of Chemistry for Frontier Technologies, State Key Laboratory of Clean Energy Utilization, Institute of Catalysis, Department of Chemistry, Zhejiang University, Hangzhou 310028, People's Republic of China;* orcid.org/0000-0003-2047-3465

Zhe Wang − *Advanced Materials and Catalysis Group, Center of Chemistry for Frontier Technologies, State Key Laboratory of Clean Energy Utilization, Institute of Catalysis, Department of Chemistry, Zhejiang University, Hangzhou 310028, People's Republic of China*

Qian Luo − *Advanced Materials and Catalysis Group, Center of Chemistry for Frontier Technologies, State Key Laboratory of Clean Energy Utilization, Institute of Catalysis, Department of Chemistry, Zhejiang University, Hangzhou 310028, People's Republic of China*

Bing Lu − *Advanced Materials and Catalysis Group, Center of Chemistry for Frontier Technologies, State Key Laboratory of Clean Energy Utilization, Institute of Catalysis, Department of Chemistry, Zhejiang University, Hangzhou 310028, People's Republic of China*

Complete contact information is available at: https://pubs.acs.org/10.1021/acscatal.2c05141

Author Contributions

The manuscript was written through contributions of all authors. All authors have given approval to the final version of the manuscript.

Funding

National Key R&D Program of China (No. 2021YFB3801600), National Natural Science Foundation of China (Nos. 21872121, 21908189), "Pioneer" and "Leading Goose" R&D Program of Zhejiang (Nos. 2022C01218, 2022C01151).

Notes

The authors declare no competing financial interest.

ACKNOWLEDGMENTS

Financial support from National Key R&D Program of China (No. 2021YFB3801600), the National Natural Science Foundation of China (Nos. 21872121, 21908189), and the "Pioneer" and "Leading Goose" R&D Program of Zhejiang (Nos. 2022C01218, 2022C01151) are greatly appreciated.

REFERENCES

(1) Ma, Z.; Zaera, F. Heterogeneous Catalysis by Metals. *Encyclopedia of Inorganic and Bioinorganic Chemistry* **2014**, 1−16.

(2) Zhang, L.; Zhou, M.; Wang, A.; Zhang, T. Selective Hydrogenation over Supported Metal Catalysts: From Nanoparticles to Single Atoms. *Chem. Rev.* **2020**, *120* (2), 683−733.

(3) Song, T.; Li, Q.; Ma, Z.; Yang, Y. Recent advance in selective hydrogenation reaction catalyzed by biomass-derived non-noble metal nanocomposites. *Tetrahedron Lett.* **2021**, *83*, 153331.

(4) Prins, R. Book Review: Hydrodesulfurization and Hydrodenitrogenation. By Toshiaki Kabe, Atsushui Ishihara and Weihua Qian. *Angew. Chem., Int. Ed.* **2001**, *40* (8), 1551−1551.

(5) Wang, Z.; Luo, Q.; Mao, S.; Wang, C.; Xiong, J.; Chen, Z.; Wang, Y. Fundamental aspects of alkyne semi-hydrogenation over heterogeneous catalysts. *Nano Res.* **2022**, *15* (12), 10044−10062.

(6) Kong, X.; Gong, Y.; Mao, S.; Wang, Y. Selective Hydrogenation of Phenol. *ChemNanoMat* **2018**, *4* (5), 432−450.

(7) Dodgson, I. L.; Griffin, K. N.; Barberis, G.; Pignataro, F.; Tauszik, G. R. A low cost phenol to cyclohexanone process. *Chem. Ind.* **1989**, *24*, 830−833.

(8) Toyoda, E.; Jinnouchi, R.; Hatanaka, T.; Morimoto, Y.; Mitsuhara, K.; Visikovskiy, A.; Kido, Y. The d-Band Structure of Pt Nanoclusters Correlated with the Catalytic Activity for an Oxygen Reduction Reaction. *J. Phys. Chem. C* **2011**, *115* (43), 21236−21240.

(9) Furimsky, E. Chemistry of Catalytic Hydrodeoxygenation. *Catal. Rev.* **1983**, *25* (3), 421−458.

(10) Bu, Q.; Lei, H.; Zacher, A. H.; Wang, L.; Ren, S.; Liang, J.; Wei, Y.; Liu, Y.; Tang, J.; Zhang, Q.; et al. A review of catalytic hydrodeoxygenation of lignin-derived phenols from biomass pyrolysis. *Bioresour. Technol.* **2012**, *124*, 470−477.

(11) Stanislaus, A.; Cooper, B. H. Aromatic Hydrogenation Catalysis: A Review. *Catal. Rev.* **1994**, *36* (1), 75−123.

(12) Liu, Q.; Xu, G.; Wang, X.; Liu, X.; Mu, X. Highly Selective Upgrading of Biomass-Derived Alcohol Mixtures for Jet/Diesel-Fuel Components. *ChemSusChem* **2016**, *9* (24), 3465−3472.

(13) Guo, N.; Caratzoulas, S.; Doren, D. J.; Sandler, S. I.; Vlachos, D. G. A perspective on the modeling of biomass processing. *Energy Environ. Sci.* **2012**, *5* (5), 6703−6716.

(14) Kelly, T. G.; Chen, J. G. Controlling C-O, C-C and C-H bond scission for deoxygenation, reforming, and dehydrogenation of ethanol using metal-modified molybdenum carbide surfaces. *Green Chem.* **2014**, *16* (2), 777−784.

(15) Wang, T.; Nolte, M. W.; Shanks, B. H. Catalytic dehydration of C6 carbohydrates for the production of hydroxymethylfurfural (HMF) as a versatile platform chemical. *Green Chem.* **2014**, *16* (2), 548−572.

(16) Yang, J.; Williams, C. L.; Ramasubramaniam, A.; Dauenhauer, P. J. Aqueous-phase hydrodeoxygenation of highly oxygenated aromatics on platinum. *Green Chem.* **2014**, *16* (2), 675−682.

(17) Meemken, F.; Baiker, A. Recent Progress in Heterogeneous Asymmetric Hydrogenation of C═O and C═C Bonds on Supported Noble Metal Catalysts. *Chem. Rev.* **2017**, *117* (17), 11522−11569.

(18) Luneau, M.; Lim, J. S.; Patel, D. A.; Sykes, E. C. H.; Friend, C. M.; Sautet, P. Guidelines to Achieving High Selectivity for the Hydrogenation of alpha,beta-Unsaturated Aldehydes with Bimetallic and Dilute Alloy Catalysts: A Review. *Chem. Rev.* **2020**, *120* (23), 12834−12872.

(19) Zaera, F. Chiral Modification of Solid Surfaces: A Molecular View. *J. Phys. Chem. C* **2008**, *112* (42), 16196−16203.

(20) van Santen, R. A.; Neurock, M.; Shetty, S. G. Reactivity Theory of Transition-Metal Surfaces: A Brønsted-Evans-Polanyi Linear Activation Energy-Free-Energy Analysis. *Chem. Rev.* **2010**, *110* (4), 2005−2048.

(21) Komarewsky, V. I.; Bos, L. B.; Coley, J. R. Vanadium Oxide, a Hydrogenation Catalyst1. *J. Am. Chem. Soc.* **1948**, *70* (1), 428−430.

(22) Welch, G. C.; Juan, R. R. S.; Masuda, J. D.; Stephan, D. W. Reversible, Metal-Free Hydrogen Activation. *Science* **2006**, *314* (5802), 1124−1126.

(23) Welch, G. C.; Stephan, D. W. Facile Heterolytic Cleavage of Dihydrogen by Phosphines and Boranes. *J. Am. Chem. Soc.* **2007**, *129* (7), 1880−1881.

(24) Paradies, J. Frustrated Lewis Pair Catalyzed Hydrogenations. *Synlett* **2013**, *24* (07), 777−780.

(25) Rokob, T. A.; Bakó, I.; Stirling, A.; Hamza, A.; Pápai, I. Reactivity Models of Hydrogen Activation by Frustrated Lewis Pairs: Synergistic Electron Transfers or Polarization by Electric Field? *J. Am. Chem. Soc.* **2013**, *135* (11), 4425−4437.

(26) Vilé, G.; Wrabetz, S.; Floryan, L.; Schuster, M. E.; Girgsdies, F.; Teschner, D.; Pérez-Ramírez, J. Stereo- and Chemoselective Character of Supported CeO2 Catalysts for Continuous-Flow Three-Phase Alkyne Hydrogenation. *ChemCatChem.* **2014**, *6* (7), 1928−1934.
(27) Vilé, G.; Colussi, S.; Krumeich, F.; Trovarelli, A.; Pérez-Ramírez, J. Opposite Face Sensitivity of CeO2 in Hydrogenation and Oxidation Catalysis. *Angew. Chem., Int. Ed.* **2014**, *53* (45), 12069−12072.
(28) Song, J.; Huang, Z.-F.; Pan, L.; Zou, J.-J.; Zhang, X.; Wang, L. Oxygen-Deficient Tungsten Oxide as Versatile and Efficient Hydrogenation Catalyst. *ACS Catal.* **2015**, *5* (11), 6594−6599.
(29) Chrétien, S.; Metiu, H. Hydrogen Dissociative Adsorption on Lanthana: Polaron Formation and the Role of Acid-Base Interactions. *J. Phys. Chem. C* **2015**, *119* (34), 19876−19882.
(30) Wu, Z.; Cheng, Y.; Tao, F.; Daemen, L.; Foo, G. S.; Nguyen, L.; Zhang, X.; Beste, A.; Ramirez-Cuesta, A. J. Direct Neutron Spectroscopy Observation of Cerium Hydride Species on a Cerium Oxide Catalyst. *J. Am. Chem. Soc.* **2017**, *139* (28), 9721−9727.
(31) Zhang, S.; Huang, Z.-Q.; Ma, Y.; Gao, W.; Li, J.; Cao, F.; Li, L.; Chang, C.-R.; Qu, Y. Solid frustrated-Lewis-pair catalysts constructed by regulations on surface defects of porous nanorods of CeO_2. *Nat. Commun.* **2017**, *8* (1), 15266.
(32) Huang, Z.-Q.; Liu, L.-P.; Qi, S.; Zhang, S.; Qu, Y.; Chang, C.-R. Understanding All-Solid Frustrated-Lewis-Pair Sites on CeO2 from Theoretical Perspectives. *ACS Catal.* **2018**, *8* (1), 546−554.
(33) Sakata, Y.; Ponec, V. Reduction of benzoic acid on CeO_2 and, the effect of additives. *Appl. Catal., A* **1998**, *166* (1), 173−184.
(34) Grootendorst, E. J.; Pestman, R.; Koster, R. M.; Ponec, V. Selective Reduction of Acetic Acid to Acetaldehyde on Iron Oxides. *J. Catal.* **1994**, *148* (1), 261−269.
(35) Vilé, G.; Bridier, B.; Wichert, J.; Pérez-Ramírez, J. Ceria in Hydrogenation Catalysis: High Selectivity in the Conversion of Alkynes to Olefins. *Angew. Chem., Int. Ed.* **2012**, *51* (34), 8620−8623.
(36) Bonrath, W.; Eggersdorfer, M.; Netscher, T. Catalysis in the industrial preparation of vitamins and nutraceuticals. *Catal. Today* **2007**, *121* (1), 45−57.
(37) Vilé, G.; Dähler, P.; Vecchietti, J.; Baltanás, M.; Collins, S.; Calatayud, M.; Bonivardi, A.; Pérez-Ramírez, J. Promoted ceria catalysts for alkyne semi-hydrogenation. *J. Catal.* **2015**, *324*, 69−78.
(38) Fang, M.; Machalaba, N.; Sánchez-Delgado, R. A. Hydrogenation of arenes and N-heteroaromatic compounds over ruthenium nanoparticles on poly(4-vinylpyridine): a versatile catalyst operating by a substrate-dependent dual site mechanism. *Dalton Trans.* **2011**, *40* (40), 10621−10632.
(39) Fang, M.; Sánchez-Delgado, R. A. Ruthenium nanoparticles supported on magnesium oxide: A versatile and recyclable dual-site catalyst for hydrogenation of mono- and poly-cyclic arenes, N-heteroaromatics, and S-heteroaromatics. *J. Catal.* **2014**, *311*, 357−368.
(40) Liu, P.; Zhao, Y.; Qin, R.; Mo, S.; Chen, G.; Gu, L.; Chevrier, D. M.; Zhang, P.; Guo, Q.; Zang, D.; et al. Photochemical route for synthesizing atomically dispersed palladium catalysts. *Science* **2016**, *352* (6287), 797−800.
(41) Wei, Z.; Mao, S.; Sun, F.; Wang, J.; Mei, B.; Chen, Y.; Li, H.; Wang, Y. The synergic effects at the molecular level in CoS2 for selective hydrogenation of nitroarenes. *Green Chem.* **2018**, *20* (3), 671−679.
(42) Rao, D.; Xue, X.; Cui, G.; He, S.; Xu, M.; Bing, W.; Shi, S.; Wei, M. Metal-acid site synergistic catalysis in Ru-ZrO2 toward selective hydrogenation of benzene to cyclohexene. *Catal. Sci. Technol.* **2018**, *8* (1), 236−243.
(43) Xue, X.; Liu, J.; Rao, D.; Xu, S.; Bing, W.; Wang, B.; He, S.; Wei, M. Double-active site synergistic catalysis in Ru-TiO2 toward benzene hydrogenation to cyclohexene with largely enhanced selectivity. *Catal. Sci. Technol.* **2017**, *7* (3), 650−657.
(44) Meng, W.; Feng, X.; Du, H. Frustrated Lewis Pairs Catalyzed Asymmetric Metal-Free Hydrogenations and Hydrosilylations. *Acc. Chem. Res.* **2018**, *51* (1), 191−201.
(45) Sitte, N. A.; Bursch, M.; Grimme, S.; Paradies, J. Frustrated Lewis Pair Catalyzed Hydrogenation of Amides: Halides as Active Lewis Base in the Metal-Free Hydrogen Activation. *J. Am. Chem. Soc.* **2019**, *141* (1), 159−162.
(46) Lan, X.; Wang, T. Highly Selective Catalysts for the Hydrogenation of Unsaturated Aldehydes: A Review. *ACS Catal.* **2020**, *10* (4), 2764−2790.
(47) Chen, Y.; Wang, Z.; Mao, S.; Wang, Y. Rational design of hydrogenation catalysts using nitrogen-doped porous carbon. *Chin. J. Catal.* **2019**, *40* (7), 971−979.
(48) Wang, H.; Lu, J. A Review on Particle Size Effect in Metal-Catalyzed Heterogeneous Reactions. *Chin. J. Chem.* **2020**, *38* (11), 1422−1444.
(49) Matsumoto, C.; Kim, Y.; Okawa, T.; Sainoo, Y.; Kawai, M. Low-temperature STM investigation of acetylene on Pd(111). *Surf. Sci.* **2005**, *587* (1−2), 19−24.
(50) Okada, T.; Kim, Y.; Sainoo, Y.; Komeda, T.; Trenary, M.; Kawai, M. Coexistence and Interconversion of Di-σ and π-Bonded Ethylene on the Pt(111) and Pd(110) Surfaces. *J. Phys. Chem. Lett.* **2011**, *2* (17), 2263−2266.
(51) Ugeda, M. M.; Yu, M.; Bradley, A. J.; Doak, P.; Liu, W.; Moore, G. F.; Sharp, I. D.; Tilley, T. D.; Neaton, J. B.; Crommie, M. F. Adsorption and Stability of π-Bonded Ethylene on GaP(110). *J. Phys. Chem. C* **2013**, *117* (49), 26091−26096.
(52) Bernardo, C. G. P. M.; Gomes, J. A. N. F. The adsorption of ethylene on the (100) surfaces of platinum, palladium and nickel: a DFT study. *J. Mol. Struct.: THEOCHEM* **2001**, *542* (1), 263−271.
(53) Dewar, J. S. A Review of the Pi-Complex Theory. *Bull. Soc. Chim. Fr.* **1951**, *18* (3−4), C71−C79.
(54) Chatt, J.; Duncanson, L. A. 586. Olefin co-ordination compounds. Part III. Infra-red spectra and structure: attempted preparation of acetylene complexes. *J. Chem. Soc. (Resumed)* **1953**, 2939−2947.
(55) Bernardo, C. G. P. M.; Gomes, J. A. N. F.The Adsorption of Acetylene and Ethylene on Transition Metal Surfaces. In *Theoretical Aspects of Heterogeneous Catalysis*; Lipscomb, W. N., Prigogine, I., Maruani, J., Wilson, S., Ågren, H., Avnir, D., Cioslowski, J., Daudel, R., Gross, E. K. U., van Gunsteren, W. F., et al. Eds.; Springer: Dordrecht, The Netherlands, 2001; pp 217−240.
(56) Steininger, H.; Ibach, H.; Lehwald, S. Surface reactions of ethylene and oxygen on Pt(111). *Surf. Sci.* **1982**, *117* (1), 685−698.
(57) Gates, J. A.; Kesmodel, L. L. EELS analysis of the low temperature phase of ethylene chemisorbed on Pd(111). *Surf. Sci.* **1982**, *120* (2), L461−L467.
(58) Bernardo, G.; Ferreira Gomes, J.The Adsorption of Acetylene and Ethylene on Transition Metal Surfaces. In *Theoretical Aspects of Heterogeneous Catalysis*, Progress in Theoretical Chemistry and Physics, Vol. *8*; Springer, Dordrecht, The Netherlands, 2006; pp 217−240.
(59) Ichihara, S.; Yoshinobu, J.; Ogasawara, H.; Nantoh, M.; Kawai, M.; Domen, K. Adsorption of π-bonded ethylene and ethynyl on Pd(110): an STM study. *J. Electron Spectrosc. Relat. Phenom.* **1998**, *88−91*, 1003−1007.
(60) Dunphy, J. C.; Rose, M.; Behler, S.; Ogletree, D. F.; Salmeron, M.; Sautet, P. Acetylene structure and dynamics on Pd(111). *Phys. Rev. B* **1998**, *57* (20), R12705−R12708.
(61) Pallassana, V.; Neurock, M.; Lusvardi, V. S.; Lerou, J. J.; Kragten, D. D.; van Santen, R. A. A Density Functional Theory Analysis of the Reaction Pathways and Intermediates for Ethylene Dehydrogenation over Pd(111). *J. Phys. Chem. B* **2002**, *106* (7), 1656−1669.
(62) Tysoe, W. T.; Nyberg, G. L.; Lambert, R. M. Low temperature catalytic chemistry of the Pd(111) surface: benzene and ethylene from acetylene. *J. Chem. Soc., Chem. Commun.* **1983**, No. 11, 623−625.
(63) Kesmodel, L. L.; Gates, J. A. Ethylene adsorption and reaction on Pd(111): An angle-dependent EELS analysis. *Surf. Sci.* **1981**, *111* (3), L747−L754.
(64) Lim, K. H.; Mohammad, A. B.; Yudanov, I. V.; Neyman, K. M.; Bron, M.; Claus, P.; Rösch, N. Mechanism of Selective Hydrogenation

https://doi.org/10.1021/acscatal.2c05141
ACS Catal. 2023, 13, 974−1019

of α,β-Unsaturated Aldehydes on Silver Catalysts: A Density Functional Study. *J. Phys. Chem. C* **2009**, *113* (30), 13231−13240.
(65) Singh, U. K.; Albert Vannice, M. Liquid-Phase Hydrogenation of Citral over Pt/SiO_2 Catalysts: I. Temperature Effects on Activity and Selectivity. *J. Catal.* **2000**, *191* (1), 165−180.
(66) Singh, U. K.; Sysak, M. N.; Vannice, M. A. Liquid-Phase Hydrogenation of Citral over Pt/SiO_2 Catalysts: II. Hydrogenation of Reaction Intermediate Compounds. *J. Catal.* **2000**, *191* (1), 181−191.
(67) Singh, U. K.; Vannice, M. A. Kinetics of liquid-phase hydrogenation reactions over supported metal catalysts—A review. *Appl. Catal., A* **2001**, *213* (1), 1−24.
(68) Urmès, C.; Schweitzer, J.-M.; Cabiac, A.; Schuurman, Y. Kinetic Study of the Selective Hydrogenation of Acetylene over Supported Palladium under Tail-End Conditions. *Catalysts* **2019**, *9* (2), 180.
(69) Yang, Z.; Li, Y.; Cao, Y.; Zhao, X.; Chen, W.; Zhang, J.; Qian, G.; Peng, C.; Gong, X.; Duan, X. Al_2O_3 microrods supported Pd catalysts for semi-hydrogenation of acetylene: Acidic properties tuned reaction kinetics behaviors. *Chem. Eng. J.* **2022**, *445*, 136681.
(70) Li, Y.; Yan, K.; Cao, Y.; Ge, X.; Zhou, X.; Yuan, W.; Chen, D.; Duan, X. Mechanistic and Atomic-Level Insights into Semihydrogenation Catalysis to Light Olefins. *ACS Catal.* **2022**, *12* (19), 12138−12161.
(71) Ross, J. R. H.Chapter 7—The Kinetics and Mechanisms of Catalytic Reactions. In *Contemporary Catalysis*; Ross, J. R. H., Ed.; Elsevier, 2019; pp 161−186.
(72) Yang, B.; Burch, R.; Hardacre, C.; Hu, P.; Hughes, P. Selective hydrogenation of acetylene over Cu(211), Ag(211) and Au(211): Horiuti-Polanyi mechanism vs. non-Horiuti-Polanyi mechanism. *Catal. Sci. Technol.* **2017**, *7* (7), 1508−1514.
(73) Borodziński, A.; Bond, G. C. Selective Hydrogenation of Ethyne in Ethene-Rich Streams on Palladium Catalysts, Part 2: Steady-State Kinetics and Effects of Palladium Particle Size, Carbon Monoxide, and Promoters. *Catal. Rev.* **2008**, *50* (3), 379−469.
(74) Rideal, E. K. A note on a simple molecular mechanism for heterogeneous catalytic reactions. *Math. Proc. Cambridge Philos. Soc.* **1939**, *35* (1), 130−132.
(75) Dong, Y.; Zaera, F. Kinetics of hydrogen adsorption during catalytic reactions on transition metal surfaces. *Catal. Sci. Technol.* **2017**, *7* (22), 5354−5364.
(76) Kristinsdóttir, L.; Skúlason, E. A systematic DFT study of hydrogen diffusion on transition metal surfaces. *Surf. Sci.* **2012**, *606* (17), 1400−1404.
(77) Ferrin, P.; Kandoi, S.; Nilekar, A. U.; Mavrikakis, M. Hydrogen adsorption, absorption and diffusion on and in transition metal surfaces: A DFT study. *Surf. Sci.* **2012**, *606* (7), 679−689.
(78) Darling, G. R.; Holloway, $S.H_2$ dissociation dynamics on metals: where do we stand? In *The Chemical Physics of Solid Surfaces*, Vol. *11*; Elsevier, 2003; pp 27−49.
(79) Mitsui, T.; Rose, M. K.; Fomin, E.; Ogletree, D. F.; Salmeron, M. Hydrogen adsorption and diffusion on Pd(111). *Surf. Sci.* **2003**, *540* (1), 5−11.
(80) Fu, F.; Liu, Y.; Li, Y.; Fu, B.; Zheng, L.; Feng, J.; Li, D. Interfacial Bifunctional Effect Promoted Non-Noble Cu/Fe_yMgO_x Catalysts for Selective Hydrogenation of Acetylene. *ACS Catal.* **2021**, *11* (17), 11117−11128.
(81) Ferguson, G. A.; Vorotnikov, V.; Wunder, N.; Clark, J.; Gruchalla, K.; Bartholomew, T.; Robichaud, D. J.; Beckham, G. T. Ab Initio Surface Phase Diagrams for Coadsorption of Aromatics and Hydrogen on the Pt(111) Surface. *J. Phys. Chem. C* **2016**, *120* (46), 26249−26258.
(82) Nelson, R. C.; Baek, B.; Ruiz, P.; Goundie, B.; Brooks, A.; Wheeler, M. C.; Frederick, B. G.; Grabow, L. C.; Austin, R. N. Experimental and Theoretical Insights into the Hydrogen-Efficient Direct Hydrodeoxygenation Mechanism of Phenol over Ru/TiO_2. *ACS Catal.* **2015**, *5* (11), 6509−6523.
(83) Liu, F.; Xia, Y.; Xu, W.; Cao, L.; Guan, Q.; Gu, Q.; Yang, B.; Lu, J. Integration of Bimetallic Electronic Synergy with Oxide Site Isolation Improves the Selective Hydrogenation of Acetylene. *Angew. Chem., Int. Ed.* **2021**, *60* (35), 19324−19330.
(84) Kyriakou, G.; Boucher, M. B.; Jewell, A. D.; Lewis, E. A.; Lawton, T. J.; Baber, A. E.; Tierney, H. L.; Flytzani-Stephanopoulos, M.; Sykes, E. C. H. Isolated Metal Atom Geometries as a Strategy for Selective Heterogeneous Hydrogenations. *Science* **2012**, *335* (6073), 1209−1212.
(85) Bridier, B.; López, N.; Pérez-Ramírez, J. Molecular understanding of alkyne hydrogenation for the design of selective catalysts. *Dalton Trans.* **2010**, *39* (36), 8412.
(86) Koga, N. A review of the mutual dependence of Arrhenius parameters evaluated by the thermoanalytical study of solid-state reactions: The kinetic compensation effect. *Thermochim. Acta* **1994**, *244*, 1−20.
(87) Andreasen, A.; Vegge, T.; Pedersen, A. S. Compensation Effect in the Hydrogenation/Dehydrogenation Kinetics of Metal Hydrides. *J. Phys. Chem. B* **2005**, *109* (8), 3340−3344.
(88) Vogt, E. T. C.; Weckhuysen, B. M. Fluid catalytic cracking: recent developments on the grand old lady of zeolite catalysis. *Chem. Soc. Rev.* **2015**, *44* (20), 7342−7370.
(89) Tao, F.; Grass, M. E.; Zhang, Y.; Butcher, D. R.; Renzas, J. R.; Liu, Z.; Chung, J. Y.; Mun, B. S.; Salmeron, M.; Somorjai, G. A. Reaction-Driven Restructuring of Rh-Pd and Pt-Pd Core-Shell Nanoparticles. *Science* **2008**, *322* (5903), 932−934.
(90) Vendelbo, S. B.; Elkjær, C. F.; Falsig, H.; Puspitasari, I.; Dona, P.; Mele, L.; Morana, B.; Nelissen, B. J.; van Rijn, R.; Creemer, J. F.; et al. Visualization of oscillatory behaviour of Pt nanoparticles catalysing CO oxidation. *Nat. Mater.* **2014**, *13* (9), 884−890.
(91) Ertl, G. Oscillatory Kinetics and Spatio-Temporal Self-Organization in Reactions at Solid Surfaces. *Science* **1991**, *254* (5039), 1750−1755.
(92) van Ravenhorst, I. K.; Vogt, C.; Oosterbeek, H.; Bossers, K. W.; Moya-Cancino, J. G.; van Bavel, A. P.; van der Eerden, A. M. J.; Vine, D.; de Groot, F. M. F.; Meirer, F.; et al. Capturing the Genesis of an Active Fischer−Tropsch Synthesis Catalyst with Operando X-ray Nanospectroscopy. *Angew. Chem., Int. Ed.* **2018**, *57* (37), 11957−11962.
(93) Vogt, C.; Weckhuysen, B. M. The concept of active site in heterogeneous catalysis. *Nat. Rev. Chem.* **2022**, *6* (2), 89−111.
(94) Rao, C. N. R.; Kulkarni, G. U.; Thomas, P. J.; Edwards, P. P. Size-Dependent Chemistry: Properties of Nanocrystals. *Chem.—Eur. J.* **2002**, *8* (1), 28−35.
(95) Cao, S.; Tao, F. F.; Tang, Y.; Li, Y.; Yu, J. Size- and shape-dependent catalytic performances of oxidation and reduction reactions on nanocatalysts. *Chem. Soc. Rev.* **2016**, *45* (17), 4747−4765.
(96) Li, Z.; Ji, S.; Liu, Y.; Cao, X.; Tian, S.; Chen, Y.; Niu, Z.; Li, Y. Well-Defined Materials for Heterogeneous Catalysis: From Nanoparticles to Isolated Single-Atom Sites. *Chem. Rev.* **2020**, *120* (2), 623−682.
(97) Ishida, T.; Murayama, T.; Taketoshi, A.; Haruta, M. Importance of Size and Contact Structure of Gold Nanoparticles for the Genesis of Unique Catalytic Processes. *Chem. Rev.* **2020**, *120* (2), 464−525.
(98) Roldan Cuenya, B.; Behafarid, F. Nanocatalysis: size- and shape-dependent chemisorption and catalytic reactivity. *Surf. Sci. Rep.* **2015**, *70* (2), 135−187.
(99) Che, M.; Bennett, C. O.The Influence of Particle Size on the Catalytic Properties of Supported Metals. In *Advances in Catalysis*, Vol. *36*; Eley, D. D., Pines, H., Weisz, P. B., Eds.; Academic Press, 1989; pp 55−172.
(100) Boudart, M.Catalysis by Supported Metals. In *Advances in Catalysis*, Vol. *20*; Eley, D. D., Pines, H., Weisz, P. B., Eds.; Academic Press, 1969; pp 153−166.
(101) Boudart, M. Heterogeneous catalysis by metals. *J. Mol. Catal.* **1985**, *30* (1), 27−38.
(102) Van Santen, R. A. Complementary Structure Sensitive and Insensitive Catalytic Relationships. *Acc. Chem. Res.* **2009**, *42* (1), 57−66.

https://doi.org/10.1021/acscatal.2c05141
ACS Catal. 2023, 13, 974−1019

(103) Wei, J.; Iglesia, E. Structural requirements and reaction pathways in methane activation and chemical conversion catalyzed by rhodium. *J. Catal.* **2004**, *225* (1), 116−127.
(104) Tsipouriari, V. A.; Efstathiou, A. M.; Zhang, Z. L.; Verykios, X. E. Reforming of methane with carbon dioxide to synthesis gas over supported Rh catalysts. *Catal. Today* **1994**, *21* (2), 579−587.
(105) Wei, J.; Iglesia, E. Mechanism and Site Requirements for Activation and Chemical Conversion of Methane on Supported Pt Clusters and Turnover Rate Comparisons among Noble Metals. *J. Phys. Chem. B* **2004**, *108* (13), 4094−4103.
(106) Yu, J.; Zhang, Z.; Dallmann, F.; Zhang, J.; Miao, D.; Xu, H.; Goldbach, A.; Dittmeyer, R. Facile synthesis of highly active Rh/Al2O3 steam reforming catalysts with preformed support by flame spray pyrolysis. *Appl. Catal., B* **2016**, *198*, 171−179.
(107) Ramallo-López, J. M.; Requejo, F. G.; Craievich, A. F.; Wei, J.; Avalos-Borja, M.; Iglesia, E. Complementary methods for cluster size distribution measurements: supported platinum nanoclusters in methane reforming catalysts. *J. Mol. Catal. A: Chem.* **2005**, *228* (1), 299−307.
(108) Wei, J.; Iglesia, E. Isotopic and kinetic assessment of the mechanism of reactions of CH_4 with CO_2 or H_2O to form synthesis gas and carbon on nickel catalysts. *J. Catal.* **2004**, *224* (2), 370−383.
(109) Bezemer, G. L.; Bitter, J. H.; Kuipers, H. P. C. E.; Oosterbeek, H.; Holewijn, J. E.; Xu, X.; Kapteijn, F.; van Dillen, A. J.; de Jong, K. P. Cobalt Particle Size Effects in the Fischer−Tropsch Reaction Studied with Carbon Nanofiber Supported Catalysts. *J. Am. Chem. Soc.* **2006**, *128* (12), 3956−3964.
(110) Fujitani, T.; Nakamura, I. Methanol Synthesis from CO and CO_2 Hydrogenations over Supported Palladium Catalysts. *Bull. Chem. Soc. Jpn.* **2002**, *75* (6), 1393−1398.
(111) Karelovic, A.; Ruiz, P. Mechanistic study of low temperature CO_2 methanation over Rh/TiO_2 catalysts. *J. Catal.* **2013**, *301*, 141−153.
(112) Schlatter, J. C.; Boudart, M. Hydrogenation of ethylene on supported platinum. *J. Catal.* **1972**, *24* (3), 482−492.
(113) Shaikhutdinov, S.; Heemeier, M.; Bäumer, M.; Lear, T.; Lennon, D.; Oldman, R. J.; Jackson, S. D.; Freund, H. J. Structure-Reactivity Relationships on Supported Metal Model Catalysts: Adsorption and Reaction of Ethene and Hydrogen on Pd/Al2O3/NiAl(110). *J. Catal.* **2001**, *200* (2), 330−339.
(114) Liu, L.; Corma, A. Metal Catalysts for Heterogeneous Catalysis: From Single Atoms to Nanoclusters and Nanoparticles. *Chem. Rev.* **2018**, *118* (10), 4981−5079.
(115) Schmid, G.; Corain, B. Nanoparticulated Gold: Syntheses, Structures, Electronics, and Reactivities. *Eur. J. Inorg. Chem.* **2003**, *2003* (17), 3081−3098.
(116) Halperin, W. P. Quantum size effects in metal particles. *Rev. Mod. Phys.* **1986**, *58* (3), 533−606.
(117) Wang, Z.; Wang, C.; Mao, S.; Lu, B.; Chen, Y.; Zhang, X.; Chen, Z.; Wang, Y. Decoupling the electronic and geometric effects of Pt catalysts in selective hydrogenation reaction. *Nat. Commun.* **2022**, *13* (1), 3561.
(118) Wang, H.; Gu, X.-K.; Zheng, X.; Pan, H.; Zhu, J.; Chen, S.; Cao, L.; Li, W.-X.; Lu, J. Disentangling the size-dependent geometric and electronic effects of palladium nanocatalysts beyond selectivity. *Sci. Adv.* **2019**, *5* (1), No. eaat6413.
(119) Norskov, J. K.; Bligaard, T.; Hvolbaek, B.; Abild-Pedersen, F.; Chorkendorff, I.; Christensen, C. H. The nature of the active site in heterogeneous metal catalysis. *Chem. Soc. Rev.* **2008**, *37* (10), 2163−2171.
(120) Bodineau, T. The Wulff Construction in Three and More Dimensions. *Commun. Math. Phys.* **1999**, *207* (1), 197−229.
(121) Honkala, K.; Hellman, A.; Remediakis, I. N.; Logadottir, A.; Carlsson, A.; Dahl, S.; Christensen, C. H.; Nørskov, J. K. Ammonia Synthesis from First-Principles Calculations. *Science* **2005**, *307* (5709), 555−558.
(122) van Hardeveld, R.; van Montfoort, A. The influence of crystallite size on the adsorption of molecular nitrogen on nickel, palladium and platinum: An infrared and electron-microscopic study. *Surf. Sci.* **1966**, *4* (4), 396−430.
(123) Zambelli, T.; Wintterlin, J.; Trost, J.; Ertl, G. Identification of the "Active Sites" of a Surface-Catalyzed Reaction. *Science* **1996**, *273* (5282), 1688−1690.
(124) Dahl, S.; Logadottir, A.; Egeberg, R. C.; Larsen, J. H.; Chorkendorff, I.; Törnqvist, E.; Nørskov, J. K. Role of Steps in N2 Activation on Ru(0001). *Phys. Rev. Lett.* **1999**, *83* (9), 1814−1817.
(125) Hammer, B. Bond Activation at Monatomic Steps: NO Dissociation at Corrugated Ru(0001). *Phys. Rev. Lett.* **1999**, *83* (18), 3681−3684.
(126) Hammer, B.; Nørskov, J. K.Theoretical surface science and catalysis—calculations and concepts. In *Advances in Catalysis*, Vol. *45*; Academic Press, 2000; pp 71−129.
(127) Shetty, S.; Jansen, A. P. J.; van Santen, R. A. CO Dissociation on the Ru(1121) Surface. *J. Phys. Chem. C* **2008**, *112* (36), 14027−14033.
(128) Ciobîcă, I. M.; Frechard, F.; van Santen, R. A.; Kleyn, A. W.; Hafner, J. A DFT Study of Transition States for C−H Activation on the Ru(0001) Surface. *J. Phys. Chem. B* **2000**, *104* (14), 3364−3369.
(129) Ge, Q.; Neurock, M. Adsorption and Activation of CO over Flat and Stepped Co Surfaces: A First Principles Analysis. *J. Phys. Chem. B* **2006**, *110* (31), 15368−15380.
(130) Lam, Y. L.; Sinfelt, J. H. Cyclohexane conversion on ruthenium catalysts of widely varying dispersion. *J. Catal.* **1976**, *42* (2), 319−322.
(131) Tait, S. L.; Dohnálek, Z.; Campbell, C. T.; Kay, B. D. Methane adsorption and dissociation and oxygen adsorption and reaction with CO on Pd nanoparticles on MgO(100) and on Pd(111). *Surf. Sci.* **2005**, *591* (1), 90−107.
(132) Wei, J.; Iglesia, E. Reaction Pathways and Site Requirements for the Activation and Chemical Conversion of Methane on Ru-Based Catalysts. *J. Phys. Chem. B* **2004**, *108* (22), 7253−7262.
(133) Somorjai, G. A.*Introduction to Surface Chemistry and Catalysis*; John Wiley & Sons, Inc., 1994; pp 54−94.
(134) Watwe, R. M.; Cortright, R. D.; Nørskov, J. K.; Dumesic, J. A. Theoretical Studies of Stability and Reactivity of C2 Hydrocarbon Species on Pt Clusters, Pt(111), and Pt(211). *J. Phys. Chem. B* **2000**, *104* (10), 2299−2310.
(135) Boudart, M.; Aldag, A.; Benson, J. E.; Dougharty, N. A.; Girvin Harkins, C. On the specific activity of platinum catalysts. *J. Catal.* **1966**, *6* (1), 92−99.
(136) Wang, S.; Petzold, V.; Tripkovic, V.; Kleis, J.; Howalt, J. G.; Skúlason, E.; Fernández, E. M.; Hvolbæk, B.; Jones, G.; Toftelund, A.; et al. Universal transition state scaling relations for (de)hydrogenation over transition metals. *Phys. Chem. Chem. Phys.* **2011**, *13* (46), 20760−20765.
(137) Ciobica, I. M.; van Santen, R. A. A DFT Study of CH_x Chemisorption and Transition States for C−H Activation on the Ru(11$\bar{2}$0) Surface. *J. Phys. Chem. B* **2002**, *106* (24), 6200−6205.
(138) Liu, Z.-P.; Hu, P. General Rules for Predicting Where a Catalytic Reaction Should Occur on Metal Surfaces: A Density Functional Theory Study of C−H and C−O Bond Breaking/Making on Flat, Stepped, and Kinked Metal Surfaces. *J. Am. Chem. Soc.* **2003**, *125* (7), 1958−1967.
(139) Diefenbach, A.; de Jong, G. T.; Bickelhaupt, F. M. Activation of H−H, C−H, C−C and C−Cl Bonds by Pd and PdCl-. Understanding Anion Assistance in C−X Bond Activation. *J. Chem. Theory Comput.* **2005**, *1* (2), 286−298.
(140) Liu, B.; Greeley, J. A density functional theory analysis of trends in glycerol decomposition on close-packed transition metal surfaces. *Phys. Chem. Chem. Phys.* **2013**, *15* (17), 6475−6485.
(141) Gajdo, M.; Eichler, A.; Hafner, J. CO adsorption on close-packed transition and noble metal surfaces: trends from ab initio calculations. *J. Phys.: Condens. Matter* **2004**, *16* (8), 1141−1164.
(142) Gajdoš, M.; Hafner, J.; Eichler, A. Ab initio density-functional study of NO adsorption on close-packed transition and noble metal surfaces: II. Dissociative adsorption. *J. Phys.: Condens. Matter* **2006**, *18* (1), 41−54.

https://doi.org/10.1021/acscatal.2c05141
ACS Catal. 2023, 13, 974−1019

(143) Liu, Z.-P.; Hu, P. General trends in CO dissociation on transition metal surfaces. *J. Chem. Phys.* **2001**, *114* (19), 8244−8247.
(144) Liu, Z.-P.; Hu, P. General trends in the barriers of catalytic reactions on transition metal surfaces. *J. Chem. Phys.* **2001**, *115* (11), 4977−4980.
(145) Saadun, A. J.; Zichittella, G.; Paunović, V.; Markaide-Aiastui, B. A.; Mitchell, S.; Pérez-Ramírez, J. Epitaxially Directed Iridium Nanostructures on Titanium Dioxide for the Selective Hydrodechlorination of Dichloromethane. *ACS Catal.* **2020**, *10* (1), 528−542.
(146) Semagina, N.; Renken, A.; Laub, D.; Kiwiminsker, L. Synthesis of monodispersed palladium nanoparticles to study structure sensitivity of solvent-free selective hydrogenation of 2-methyl-3-butyn-2-ol. *J. Catal.* **2007**, *246* (2), 308−314.
(147) Silvestre-Albero, J.; Rupprechter, G.; Freund, H.-J. From Pd nanoparticles to single crystals: 1,3-butadiene hydrogenation on well-defined model catalysts. *Chem. Commun.* **2006**, No. 1, 80−82.
(148) Lindlar, H. Ein neuer Katalysator für selektive Hydrierungen. *Helv. Chim. Acta* **1952**, *35* (2), 446−450.
(149) Mao, S.; Zhao, B.; Wang, Z.; Gong, Y.; Lü, G.; Ma, X.; Yu, L.; Wang, Y. Tuning the catalytic performance for the semi-hydrogenation of alkynols by selectively poisoning the active sites of Pd catalysts. *Green Chem.* **2019**, *21* (15), 4143−4151.
(150) Luo, Q.; Wang, Z.; Chen, Y.; Mao, S.; Wu, K.; Zhang, K.; Li, Q.; Lv, G.; Huang, G.; Li, H.; et al. Dynamic Modification of Palladium Catalysts with Chain Alkylamines for the Selective Hydrogenation of Alkynes. *ACS Appl. Mater. Interfaces* **2021**, *13* (27), 31775−31784.
(151) Evangelisti, C.; Panziera, N.; D'Alessio, A.; Bertinetti, L.; Botavina, M.; Vitulli, G. New monodispersed palladium nanoparticles stabilized by poly-(N-vinyl-2-pyrrolidone): Preparation, structural study and catalytic properties. *J. Catal.* **2010**, *272* (2), 246−252.
(152) Shen, L.; Mao, S.; Li, J.; Li, M.; Chen, P.; Li, H.; Chen, Z.; Wang, Y. PdZn intermetallic on a CN@ZnO hybrid as an efficient catalyst for the semihydrogenation of alkynols. *J. Catal.* **2017**, *350*, 13−20.
(153) Zhou, H.; Yang, X.; Li, L.; Liu, X.; Huang, Y.; Pan, X.; Wang, A.; Li, J.; Zhang, T. PdZn Intermetallic Nanostructure with Pd-Zn-Pd Ensembles for Highly Active and Chemoselective Semi-Hydrogenation of Acetylene. *ACS Catal.* **2016**, *6* (2), 1054−1061.
(154) Cao, Y.; Ge, X.; Li, Y.; Si, R.; Sui, Z.; Zhou, J.; Duan, X.; Zhou, X. Structural and Kinetics Understanding of Support Effects in Pd-Catalyzed Semi-Hydrogenation of Acetylene. *Engineering* **2021**, *7* (1), 103−110.
(155) Pei, G. X.; Liu, X. Y.; Yang, X.; Zhang, L.; Wang, A.; Li, L.; Wang, H.; Wang, X.; Zhang, T. Performance of Cu-Alloyed Pd Single-Atom Catalyst for Semihydrogenation of Acetylene under Simulated Front-End Conditions. *ACS Catal.* **2017**, *7* (2), 1491−1500.
(156) Huang, F.; Deng, Y.; Chen, Y.; Cai, X.; Peng, M.; Jia, Z.; Xie, J.; Xiao, D.; Wen, X.; Wang, N.; et al. Anchoring Cu1 species over nanodiamond-graphene for semi-hydrogenation of acetylene. *Nat. Commun.* **2019**, *10* (1), 4431.
(157) Sun, M.; Wang, F.; Lv, G.; Zhang, X. Size effect of PdC nanoparticles synthesized by S-containing silane coupling agents on semi-hydrogenation of acetylene. *Appl. Surf. Sci.* **2022**, *589*, 153021.
(158) Zhou, S.; Shang, L.; Zhao, Y.; Shi, R.; Waterhouse, G. I. N.; Huang, Y.-C.; Zheng, L.; Zhang, T. Pd Single-Atom Catalysts on Nitrogen-Doped Graphene for the Highly Selective Photothermal Hydrogenation of Acetylene to Ethylene. *Adv. Mater.* **2019**, *31* (18), 1900509.
(159) Huang, X.; Yan, H.; Huang, L.; Zhang, X.; Lin, Y.; Li, J.; Xia, Y.; Ma, Y.; Sun, Z.; Wei, S.; et al. Toward Understanding of the Support Effect on Pd1 Single-Atom-Catalyzed Hydrogenation Reactions. *J. Phys. Chem. C* **2019**, *123* (13), 7922−7930.
(160) Sarkany, A. Semi-hydrogenation of 1,3-butadiene over Pd—Ag/α-Al_2O_3 poisoned by hydrocarbonaceous deposits. *Appl. Catal., A* **1997**, *165* (1), 87−101.
(161) Armbrüster, M.; Kovnir, K.; Behrens, M.; Teschner, D.; Grin, Y.; Schlögl, R. Pd-Ga Intermetallic Compounds as Highly Selective Semihydrogenation Catalysts. *J. Am. Chem. Soc.* **2010**, *132* (42), 14745−14747.
(162) Gao, R.; Xu, J.; Wang, J.; Lim, J.; Peng, C.; Pan, L.; Zhang, X.; Yang, H.; Zou, J.-J. Pd/Fe_2O_3 with Electronic Coupling Single-Site Pd−Fe Pair Sites for Low-Temperature Semihydrogenation of Alkynes. *J. Am. Chem. Soc.* **2022**, *144* (1), 573−581.
(163) Li, Z.; Zhang, J.; Tian, J.; Feng, K.; Jiang, Z.; Yan, B. Unveiling the origin of enhanced catalytic performance of NiCu alloy for semi-hydrogenation of acetylene. *Chem. Eng. J.* **2022**, *450*, 138244.
(164) Larsson, M.; Jansson, J.; Asplund, S. The Role of Coke in Acetylene Hydrogenation on Pd/α-Al_2O_3. *J. Catal.* **1998**, *178* (1), 49−57.
(165) Asplund, S. Coke Formation and Its Effect on Internal Mass Transfer and Selectivity in Pd-Catalysed Acetylene Hydrogenation. *J. Catal.* **1996**, *158* (1), 267−278.
(166) Shao, L.; Zhang, W.; Armbrüster, M.; Teschner, D.; Girgsdies, F.; Zhang, B.; Timpe, O.; Friedrich, M.; Schlögl, R.; Su, D. S. Nanosizing Intermetallic Compounds Onto Carbon Nanotubes: Active and Selective Hydrogenation Catalysts. *Angew. Chem., Int. Ed.* **2011**, *50* (43), 10231−10235.
(167) Feng, Q.; Zhao, S.; Wang, Y.; Dong, J.; Chen, W.; He, D.; Wang, D.; Yang, J.; Zhu, Y.; Zhu, H.; et al. Isolated Single-Atom Pd Sites in Intermetallic Nanostructures: High Catalytic Selectivity for Semihydrogenation of Alkynes. *J. Am. Chem. Soc.* **2017**, *139* (21), 7294−7301.
(168) Cao, Y.; Zhang, H.; Ji, S.; Sui, Z.; Jiang, Z.; Wang, D.; Zaera, F.; Zhou, X.; Duan, X.; Li, Y. Adsorption Site Regulation to Guide Atomic Design of Ni-Ga Catalysts for Acetylene Semi-Hydrogenation. *Angew. Chem., Int. Ed.* **2020**, *59* (28), 11647−11652.
(169) Ge, X.; Dou, M.; Cao, Y.; Liu, X.; Yuwen, Q.; Zhang, J.; Qian, G.; Gong, X.; Zhou, X.; Chen, L.; et al. Mechanism driven design of trimer Ni1Sb2 site delivering superior hydrogenation selectivity to ethylene. *Nat. Commun.* **2022**, *13* (1), 5534.
(170) Ge, X.; Cao, Y.; Yan, K.; Li, Y.; Zhou, L.; Dai, S.; Zhang, J.; Gong, X.; Qian, G.; Zhou, X.; et al. Increasing the Distance of Adjacent Palladium Atoms for Configuration Matching in Selective Hydrogenation. *Angew. Chem., Int. Ed.* **2022**, *61* (51), No. e202215225.
(171) Lou, B.; Kang, H.; Yuan, W.; Ma, L.; Huang, W.; Wang, Y.; Jiang, Z.; Du, Y.; Zou, S.; Fan, J. Highly Selective Acetylene Semihydrogenation Catalyst with an Operation Window Exceeding 150 °C. *ACS Catal.* **2021**, *11* (10), 6073−6080.
(172) Studt, F.; Abild-Pedersen, F.; Bligaard, T.; Sørensen, R. Z.; Christensen, C. H.; Nørskov, J. K. Identification of Non-Precious Metal Alloy Catalysts for Selective Hydrogenation of Acetylene. *Science* **2008**, *320* (5881), 1320−1322.
(173) Osswald, J.; Kovnir, K.; Armbrüster, M.; Giedigkeit, R.; Jentoft, R. E.; Wild, U.; Grin, Y.; Schlögl, R. Palladium-gallium intermetallic compounds for the selective hydrogenation of acetylene: Part II: Surface characterization and catalytic performance. *J. Catal.* **2008**, *258* (1), 219−227.
(174) McCue, A. J.; Guerrero-Ruiz, A.; Ramirez-Barria, C.; Rodríguez-Ramos, I.; Anderson, J. A. Selective hydrogenation of mixed alkyne/alkene streams at elevated pressure over a palladium sulfide catalyst. *J. Catal.* **2017**, *355*, 40−52.
(175) Guo, Q.; Chen, R.; Guo, J.; Qin, C.; Xiong, Z.; Yan, H.; Gao, W.; Pei, Q.; Wu, A.; Chen, P. Enabling Semihydrogenation of Alkynes to Alkenes by Using a Calcium Palladium Complex Hydride. *J. Am. Chem. Soc.* **2021**, *143* (49), 20891−20897.
(176) Liu, Y.; Fu, F.; McCue, A.; Jones, W.; Rao, D.; Feng, J.; He, Y.; Li, D. Adsorbate-Induced Structural Evolution of Pd Catalyst for Selective Hydrogenation of Acetylene. *ACS Catal.* **2020**, *10* (24), 15048−15059.
(177) Mortensen, P. M.; Grunwaldt, J.-D.; Jensen, P. A.; Jensen, A. D. Influence on nickel particle size on the hydrodeoxygenation of phenol over Ni/SiO_2. *Catal. Today* **2016**, *259*, 277−284.
(178) Resende, K. A.; Hori, C. E.; Noronha, F. B.; Shi, H.; Gutierrez, O. Y.; Camaioni, D. M.; Lercher, J. A. Aqueous phase hydrogenation

https://doi.org/10.1021/acscatal.2c05141
ACS Catal. 2023, 13, 974−1019

of phenol catalyzed by Pd and PdAg on ZrO_2. *Appl. Catal., A* **2017**, *548*, 128−135.
(179) Yang, Z.; Li, D.; Zhang, L.; Zheng, J.; Zhang, N.; Chen, B. H. Coupling Synergetic Effect between Ruthenium and Ruthenium Oxide with Size Effect of Ruthenium Particles on Ketone Catalytic Hydrogenation. *ChemCatChem.* **2017**, *9* (2), 338−346.
(180) Wang, H.; Bai, S.; Pi, Y.; Shao, Q.; Tan, Y.; Huang, X. A Strongly Coupled Ultrasmall Pt_3Co Nanoparticle-Ultrathin $Co(OH)_2$ Nanosheet Architecture Enhances Selective Hydrogenation of α,β-Unsaturated Aldehydes. *ACS Catal.* **2019**, *9* (1), 154−159.
(181) Singh, U. K.; Vannice, M. A. Liquid-Phase Citral Hydrogenation over SiO_2-Supported Group VIII Metals. *J. Catal.* **2001**, *199* (1), 73−84.
(182) Shi, J.; Nie, R.; Chen, P.; Hou, Z. Selective hydrogenation of cinnamaldehyde over reduced graphene oxide supported Pt catalyst. *Catal. Commun.* **2013**, *41*, 101−105.
(183) Liu, C.; Zhang, J.; Liu, H.; Qiu, J.; Zhang, X. Heterogeneous Ligand-Free Rhodium Oxide Catalyst Embedded within Zeolitic Microchannel to Enhance Regioselectivity in Hydroformylation. *Ind. Eng. Chem. Res.* **2019**, *58* (47), 21285−21295.
(184) Jiang, F.; Cai, J.; Liu, B.; Xu, Y.; Liu, X. Particle size effects in the selective hydrogenation of cinnamaldehyde over supported palladium catalysts. *RSC Adv.* **2016**, *6* (79), 75541−75551.
(185) Shi, J.; Nie, R.; Zhang, M.; Zhao, M.; Hou, Z. Microwave-assisted fast fabrication of a nanosized Pt3Co alloy on reduced graphene oxides. *Chin. J. Catal.* **2014**, *35* (12), 2029−2037.
(186) Zheng, R.; Porosoff, M. D.; Weiner, J. L.; Lu, S.; Zhu, Y.; Chen, J. G. Controlling hydrogenation of CO and CC bonds in cinnamaldehyde using silica supported Co-Pt and Cu-Pt bimetallic catalysts. *Appl. Catal., A* **2012**, *419*−*420*, 126−132.
(187) Plomp, A. J.; Vuori, H.; Krause, A. O. I.; de Jong, K. P.; Bitter, J. H. Particle size effects for carbon nanofiber supported platinum and ruthenium catalysts for the selective hydrogenation of cinnamaldehyde. *Appl. Catal., A* **2008**, *351* (1), 9−15.
(188) Wang, X.; Liang, X.; Geng, P.; Li, Q. Recent Advances in Selective Hydrogenation of Cinnamaldehyde over Supported Metal-Based Catalysts. *ACS Catal.* **2020**, *10* (4), 2395−2412.
(189) Dohade, M. G.; Dhepe, P. L. Efficient hydrogenation of concentrated aqueous furfural solutions into furfuryl alcohol under ambient conditions in presence of PtCo bimetallic catalyst. *Green Chem.* **2017**, *19* (4), 1144−1154.
(190) Khromova, S. A.; Bykova, M. V.; Bulavchenko, O. A.; Ermakov, D. Y.; Saraev, A. A.; Kaichev, V. V.; Venderbosch, R. H.; Yakovlev, V. A. Furfural Hydrogenation to Furfuryl Alcohol over Bimetallic Ni-Cu Sol-Gel Catalyst: A Model Reaction for Conversion of Oxygenates in Pyrolysis Liquids. *Top. Catal.* **2016**, *59* (15), 1413−1423.
(191) Shi, J.; Zhang, M.; Du, W.; Ning, W.; Hou, Z. SnO_2-isolated Pt3Sn alloy on reduced graphene oxide: An efficient catalyst for selective hydrogenation of C=O in unsaturated aldehydes. *Catal. Sci. Technol.* **2015**, *5* (6), 3108−3112.
(192) Tamura, M.; Tokonami, K.; Nakagawa, Y.; Tomishige, K. Selective Hydrogenation of Crotonaldehyde to Crotyl Alcohol over Metal Oxide Modified Ir Catalysts and Mechanistic Insight. *ACS Catal.* **2016**, *6* (6), 3600−3609.
(193) Li, C.; Ke, C.; Han, R.; Fan, G.; Yang, L.; Li, F. The remarkable promotion of in situ formed Pt-cobalt oxide interfacial sites on the carbonyl reduction to allylic alcohols. *Mol. Catal.* **2018**, *455*, 78−87.
(194) Xue, Y.; Xin, H.; Xie, W.; Wu, P.; Li, X. Pt nanoparticles supported on $YCo_xFe_{1-x}O_3$ perovskite oxides: highly efficient catalysts for liquid-phase hydrogenation of cinnamaldehyde. *Chem. Commun.* **2019**, *55* (23), 3363−3366.
(195) Zhao, M.; Yuan, K.; Wang, Y.; Li, G.; Guo, J.; Gu, L.; Hu, W.; Zhao, H.; Tang, Z. Metal-organic frameworks as selectivity regulators for hydrogenation reactions. *Nature* **2016**, *539* (7627), 76−80.
(196) Yuan, K.; Song, T.; Wang, D.; Zhang, X.; Gao, X.; Zou, Y.; Dong, H.; Tang, Z.; Hu, W. Effective and Selective Catalysts for Cinnamaldehyde Hydrogenation: Hydrophobic Hybrids of Metal-Organic Frameworks, Metal Nanoparticles, and Micro- and Mesoporous Polymers. *Angew. Chem., Int. Ed.* **2018**, *57* (20), 5708−5713.
(197) Yi, H.; Du, H.; Hu, Y.; Yan, H.; Jiang, H.-L.; Lu, J. Precisely Controlled Porous Alumina Overcoating on Pd Catalyst by Atomic Layer Deposition: Enhanced Selectivity and Durability in Hydrogenation of 1,3-Butadiene. *ACS Catal.* **2015**, *5* (5), 2735−2739.
(198) Lou, Y.; Zheng, Y.; Li, X.; Ta, N.; Xu, J.; Nie, Y.; Cho, K.; Liu, J. Pocketlike Active Site of $Rh1/MoS_2$ Single-Atom Catalyst for Selective Crotonaldehyde Hydrogenation. *J. Am. Chem. Soc.* **2019**, *141* (49), 19289−19295.
(199) Wu, B.; Huang, H.; Yang, J.; Zheng, N.; Fu, G. Selective Hydrogenation of α,β-Unsaturated Aldehydes Catalyzed by Amine-Capped Platinum-Cobalt Nanocrystals. *Angew. Chem., Int. Ed.* **2012**, *51* (14), 3440−3443.
(200) Ishida, T.; Honma, T.; Nakada, K.; Murayama, H.; Mamba, T.; Kume, K.; Izawa, Y.; Utsunomiya, M.; Tokunaga, M. Pd-catalyzed decarbonylation of furfural: Elucidation of support effect on Pd size and catalytic activity using in-situ XAFS. *J. Catal.* **2019**, *374*, 320−327.
(201) Goulas, K. A.; Song, Y.; Johnson, G. R.; Chen, J. P.; Gokhale, A. A.; Grabow, L. C.; Toste, F. D. Selectivity tuning over monometallic and bimetallic dehydrogenation catalysts: effects of support and particle size. *Catal. Sci. Technol.* **2018**, *8* (1), 314−327.
(202) Pushkarev, V. V.; Musselwhite, N.; An, K.; Alayoglu, S.; Somorjai, G. A. High structure sensitivity of vapor-phase furfural decarbonylation/hydrogenation reaction network as a function of size and shape of Pt nanoparticles. *Nano Lett.* **2012**, *12* (10), 5196−5201.
(203) Singh, U. K.; Albert Vannice, M. Liquid-Phase Hydrogenation of Citral over Pt/SiO_2 Catalysts. *J. Catal.* **2000**, *191* (1), 165−180.
(204) Waghray, A.; Blackmond, D. G. Infrared spectroscopic studies of the adsorption and reaction of 3-methyl-2-butenal over alkali-promoted ruthenium/silica catalysts. *J. Phys. Chem.* **1993**, *97* (22), 6002−6006.
(205) Englisch, M.; Ranade, V. S.; Lercher, J. A. Liquid phase hydrogenation of crotonaldehyde over Pt/SiO_2 catalysts. *Appl. Catal., A* **1997**, *163* (1), 111−122.
(206) Shekhar, R.; Barteau, M. A.; Plank, R. V.; Vohs, J. M. Adsorption and Reaction of Aldehydes on Pd Surfaces. *J. Phys. Chem. B* **1997**, *101* (40), 7939−7951.
(207) Davis, J. L.; Barteau, M. A. Polymerization and decarbonylation reactions of aldehydes on the Pd(111) surface. *J. Am. Chem. Soc.* **1989**, *111* (5), 1782−1792.
(208) Brown, N. F.; Barteau, M. A. Reactions of unsaturated oxygenates on rhodium(111) as probes of multiple coordination of adsorbates. *J. Am. Chem. Soc.* **1992**, *114* (11), 4258−4265.
(209) Houtman, C. J.; Barteau, M. A. Divergent pathways of acetaldehyde and ethanol decarbonylation on the Rh(111) surface. *J. Catal.* **1991**, *130* (2), 528−546.
(210) McCabe, R. W.; Schmidt, L. D. Binding States of CO on Single Crystal Planes of Pt. *Surf. Sci.* **1977**, *66*, 101−124.
(211) Ertl, G.; Neumann, M.; Streit, K. M. Chemisorption of CO on the Pt(111) surface. *Surf. Sci.* **1977**, *64* (2), 393−410.
(212) Singh, U. K.; Vannice, M. A.The influence of metal-support interactions during liquid-phase hydrogenation of an α,β-unsaturated aldehyde over Pt. In *Studies in Surface Science and Catalysis*, Vol. *130*; Corma, A., Melo, F. V., Mendioroz, S., Fierro, J. L. G., Eds.; Elsevier, 2000; pp 497−502, DOI: 10.1016/S0167-2991(00)81006-X.
(213) Manogue, W. H.; Katzer, J. R. On subdivision of the classification of demanding reactions. *J. Catal.* **1974**, *32* (1), 166−169.
(214) Somorjai, G. A.; Carrazza, J. Structure sensitivity of catalytic reactions. *Ind. Eng. Chem. Fundam.* **1986**, *25* (1), 63−69.
(215) Wang, Z.; Liang, S.; Meng, X.; Mao, S.; Lian, X.; Wang, Y. Ultrasmall PdAu alloy nanoparticles anchored on amine-functionalized hierarchically porous carbon as additive-free catalysts for highly efficient dehydrogenation of formic acid. *Appl. Catal., B* **2021**, *291*, 120140.
(216) Li, X.-T.; Chen, L.; Wei, G.-F.; Shang, C.; Liu, Z.-P. Sharp Increase in Catalytic Selectivity in Acetylene Semihydrogenation on

Pd Achieved by a Machine Learning Simulation-Guided Experiment. *ACS Catal.* **2020**, *10* (17), 9694−9705.
(217) Hoffmann, R. A chemical and theoretical way to look at bonding on surfaces. *Rev. Mod. Phys.* **1988**, *60* (3), 601−628.
(218) Fukui, K. Role of Frontier Orbitals in Chemical Reactions. *Science* **1982**, *218* (4574), 747−754.
(219) Hoffmann, R. How Chemistry and Physics Meet in the Solid State. *Angew. Chem., Int. Ed. Engl.* **1987**, *26* (9), 846−878.
(220) Hoffman, R.*Solids and Surfaces: A Chemist's View of Bonding in Extended Structures*; Wiley−VCH, 1988; pp 50−65.
(221) Wang, C.; Mao, S.; Wang, Z.; Chen, Y.; Yuan, W.; Ou, Y.; Zhang, H.; Gong, Y.; Wang, Y.; Mei, B.; et al. Insight into Single-Atom-Induced Unconventional Size Dependence over CeO_2-Supported Pt Catalysts. *Chem.* **2020**, *6* (3), 752−765.
(222) Mercadante, L.; Neri, G.; Milone, C.; Donato, A.; Galvagno, S. Hydrogenation of α,β-unsaturated aldehydes over Ru/Al_2O_3 catalysts. *J. Mol. Catal. A: Chem.* **1996**, *105* (3), 93−101.
(223) Delbecq, F.; Sautet, P. Competitive C=C and C=O Adsorption of α-β-Unsaturated Aldehydes on Pt and Pd Surfaces in Relation with the Selectivity of Hydrogenation Reactions: A Theoretical Approach. *J. Catal.* **1995**, *152* (2), 217−236.
(224) Birchem, T.; Pradier, C. M.; Berthier, Y.; Cordier, G. Reactivity of 3-Methyl-Crotonaldehyde on Pt(111). *J. Catal.* **1994**, *146* (2), 503−510.
(225) Beccat, P.; Bertolini, J. C.; Gauthier, Y.; Massardier, J.; Ruiz, P. Crotonaldehyde and methylcrotonaldehyde hydrogenation over Pt(111) and $Pt_{80}Fe_{20}$(111) single crystals. *J. Catal.* **1990**, *126* (2), 451−456.
(226) Marinelli, T. B. L. W.; Nabuurs, S.; Ponec, V. Activity and Selectivity in the Reactions of Substituted α,β-Unsaturated Aldehydes. *J. Catal.* **1995**, *151* (2), 431−438.
(227) Csicsery, S. M. Shape-selective catalysis in zeolites. *Zeolites* **1984**, *4* (3), 202−213.
(228) Li, J.; He, Y.; Tan, L.; Zhang, P.; Peng, X.; Oruganti, A.; Yang, G.; Abe, H.; Wang, Y.; Tsubaki, N. Integrated tuneable synthesis of liquid fuels via Fischer−Tropsch technology. *Nat. Catal.* **2018**, *1* (10), 787−793.
(229) Jiao, F.; Pan, X.; Gong, K.; Chen, Y.; Li, G.; Bao, X. Shape-Selective Zeolites Promote Ethylene Formation from Syngas via a Ketene Intermediate. *Angew. Chem., Int. Ed.* **2018**, *57* (17), 4692−4696.
(230) Weisz, P. B. Molecular Diffusion in Microporous Materials: Formalisms and Mechanisms. *Ind. Eng. Chem. Res.* **1995**, *34* (8), 2692−2699.
(231) Laursen, A. B.; Højholt, K. T.; Lundegaard, L. F.; Simonsen, S. B.; Helveg, S.; Schüth, F.; Paul, M.; Grunwaldt, J.-D.; Kegnæs, S.; Christensen, C. H.; et al. Substrate Size-Selective Catalysis with Zeolite-Encapsulated Gold Nanoparticles. *Angew. Chem., Int. Ed.* **2010**, *49* (20), 3504−3507.
(232) Cui, T.-L.; Ke, W.-Y.; Zhang, W.-B.; Wang, H.-H.; Li, X.-H.; Chen, J.-S. Encapsulating Palladium Nanoparticles Inside Mesoporous MFI Zeolite Nanocrystals for Shape-Selective Catalysis. *Angew. Chem., Int. Ed.* **2016**, *55* (32), 9178−9182.
(233) Liu, J.; Xie, L.; Wang, Z.; Mao, S.; Gong, Y.; Wang, Y. Biomass-derived ordered mesoporous carbon nano-ellipsoid encapsulated metal nanoparticles inside: Ideal nanoreactors for shape-selective catalysis. *Chem. Commun.* **2020**, *56* (2), 229−232.
(234) Wang, C.; Wang, L.; Zhang, J.; Wang, H.; Lewis, J. P.; Xiao, F.-S. Product Selectivity Controlled by Zeolite Crystals in Biomass Hydrogenation over a Palladium Catalyst. *J. Am. Chem. Soc.* **2016**, *138* (25), 7880−7883.
(235) Wang, Y.; Wang, C.; Wang, L.; Wang, L.; Xiao, F.-S. Zeolite Fixed Metal Nanoparticles: New Perspective in Catalysis. *Acc. Chem. Res.* **2021**, *54* (11), 2579−2590.
(236) Chai, Y.; Liu, S.; Zhao, Z.-J.; Gong, J.; Dai, W.; Wu, G.; Guan, N.; Li, L. Selectivity Modulation of Encapsulated Palladium Nanoparticles by Zeolite Microenvironment for Biomass Catalytic Upgrading. *ACS Catal.* **2018**, *8* (9), 8578−8589.
(237) Li, Z.; Li, M.; Bian, Z.; Kathiraser, Y.; Kawi, S. Design of highly stable and selective core/yolk-shell nanocatalysts—A review. *Appl. Catal., B* **2016**, *188*, 324−341.
(238) Xiong, S.; Tang, R.; Gong, D.; Deng, Y.; Zhang, C.; Zheng, J.; Zhong, M. e.; Su, L.; Yang, L.; Liao, C. Yolk-Shell catalyst: From past to future. *Appl. Mater. Today* **2020**, *21*, 100798.
(239) Guan, B.; Wang, X.; Xiao, Y.; Liu, Y.; Huo, Q. A versatile cooperative template-directed coating method to construct uniform microporous carbon shells for multifunctional core-shell nanocomposites. *Nanoscale* **2013**, *5* (6), 2469−2475.
(240) Sun, Q.; Wang, N.; Zhang, T.; Bai, R.; Mayoral, A.; Zhang, P.; Zhang, Q.; Terasaki, O.; Yu, J. Zeolite-Encaged Single-Atom Rhodium Catalysts: Highly-Efficient Hydrogen Generation and Shape-Selective Tandem Hydrogenation of Nitroarenes. *Angew. Chem., Int. Ed.* **2019**, *58* (51), 18570−18576.
(241) Moliner, M.; Gabay, J. E.; Kliewer, C. E.; Carr, R. T.; Guzman, J.; Casty, G. L.; Serna, P.; Corma, A. Reversible Transformation of Pt Nanoparticles into Single Atoms inside High-Silica Chabazite Zeolite. *J. Am. Chem. Soc.* **2016**, *138* (48), 15743−15750.
(242) Zhang, J.; Wang, L.; Zhang, B.; Zhao, H.; Kolb, U.; Zhu, Y.; Liu, L.; Han, Y.; Wang, G.; Wang, C.; et al. Sinter-resistant metal nanoparticle catalysts achieved by immobilization within zeolite crystals via seed-directed growth. *Nat. Catal.* **2018**, *1* (7), 540−546.
(243) Liu, L.; Díaz, U.; Arenal, R.; Agostini, G.; Concepción, P.; Corma, A. Generation of subnanometric platinum with high stability during transformation of a 2D zeolite into 3D. *Nat. Mater.* **2017**, *16* (1), 132−138.
(244) Zhang, J.; Wang, L.; Shao, Y.; Wang, Y.; Gates, B. C.; Xiao, F.-S. A Pd@Zeolite Catalyst for Nitroarene Hydrogenation with High Product Selectivity by Sterically Controlled Adsorption in the Zeolite Micropores. *Angew. Chem., Int. Ed.* **2017**, *56* (33), 9747−9751.
(245) Cao, Y.; Zhao, B.; Bao, X.; Wang, Y. Fabricating Metal@N-Doped Carbon Catalysts via a Thermal Method. *ACS Catal.* **2018**, *8* (8), 7077−7085.
(246) Cao, Y.; Tang, M.; Li, M.; Deng, J.; Xu, F.; Xie, L.; Wang, Y. In Situ Synthesis of Chitin-Derived Rh/N-C Cataylsts: Efficient Hydrogenation of Benzoic Acid and Derivatives. *ACS Sustainable Chem. Eng.* **2017**, *5* (11), 9894−9902.
(247) Fihri, A.; Bouhrara, M.; Nekoueishahraki, B.; Basset, J.-M.; Polshettiwar, V. Nanocatalysts for Suzuki cross-coupling reactions. *Chem. Soc. Rev.* **2011**, *40* (10), 5181−5203.
(248) Wang, H.; Wang, L.; Xiao, F.-S. Metal@Zeolite Hybrid Materials for Catalysis. *ACS Central Sci.* **2020**, *6* (10), 1685−1697.
(249) Li, Z.; Mo, L.; Kathiraser, Y.; Kawi, S. Yolk-Satellite-Shell Structured Ni-Yolk@Ni@SiO_2 Nanocomposite: Superb Catalyst toward Methane CO_2 Reforming Reaction. *ACS Catal.* **2014**, *4* (5), 1526−1536.
(250) Huang, Q.; Fang, X.; Cheng, Q.; Li, Q.; Xu, X.; Xu, L.; Liu, W.; Gao, Z.; Zhou, W.; Wang, X. Synthesis of a Highly Active and Stable Nickel-Embedded Alumina Catalyst for Methane Dry Reforming: On the Confinement Effects of Alumina Shells for Nickel Nanoparticles. *ChemCatChem.* **2017**, *9* (18), 3563−3571.
(251) Lu, Y.; Guo, D.; Ruan, Y.; Zhao, Y.; Wang, S.; Ma, X. Facile one-pot synthesis of Ni@HSS as a novel yolk-shell structure catalyst for dry reforming of methane. *J. CO_2 Util.* **2018**, *24*, 190−199.
(252) Wang, Y.; Yu, L.; Ma, X.; Mao, J.; Wang, Z.; Mao, S.; Tang, J. L.Composite catalyst, method for manufacturing composite catalyst and application thereof. U.S. Patent No. 10,668,460 B2, 2020.
(253) Wang, Y.; Yu, L.; Ma, X.; Mao, J.; Wang, Z.; Mao, S.; Li, J.; Chen, Z.PdIn alloy catalyst, method for manufacturing PdIn alloy catalyst and application thereof. U.S. Patent No. 10,737,250 B2, 2020.
(254) Wang, Y.; Lv, G.; Yu, L.; Wang, Z.; Mao, S.; Tang, J. L.; Li, H.; Chen, Z.Composite catalyst, method for manufacturing composite catalyst and application thereof. Chin. Patent No. ZL201811010567.1, 2019.
(255) Wang, Y.; Ma, X.; Yu, L.; Wang, Z.; Mao, S.; Li, J.; Chen, G.; Li, H.; Chen, Z.PdIn alloy catalyst, method for manufacturing PdIn alloy catalyst and application thereof. Chin. Patent No. ZL201811010568.6, 2019.

https://doi.org/10.1021/acscatal.2c05141
ACS Catal. 2023, 13, 974−1019

(256) Li, T.; Dong, Q.; Huang, Z.; Wu, L.; Yao, Y.; Gao, J.; Wang, X.; Zhang, H.; Wang, D.; Li, T.; et al. Interface Engineering Between Multi-Elemental Alloy Nanoparticles and a Carbon Support Toward Stable Catalysts. *Adv. Mater.* **2022**, *34* (9), 2106436.
(257) Li, X.; Pereira-Hernández, X. I.; Chen, Y.; Xu, J.; Zhao, J.; Pao, C.-W.; Fang, C.-Y.; Zeng, J.; Wang, Y.; Gates, B. C.; et al. Functional CeO_x nanoglues for robust atomically dispersed catalysts. *Nature* **2022**, *611* (7935), 284−288.
(258) Lang, R.; Du, X.; Huang, Y.; Jiang, X.; Zhang, Q.; Guo, Y.; Liu, K.; Qiao, B.; Wang, A.; Zhang, T. Single-Atom Catalysts Based on the Metal-Oxide Interaction. *Chem. Rev.* **2020**, *120* (21), 11986−12043.
(259) Xiong, H.; Datye, A. K.; Wang, Y. Thermally Stable Single-Atom Heterogeneous Catalysts. *Adv. Mater.* **2021**, *33* (50), 2004319.
(260) Wang, A.; Li, J.; Zhang, T. Heterogeneous single-atom catalysis. *Nat. Rev. Chem.* **2018**, *2* (6), 65−81.
(261) Chen, Z.; Liu, J.; Koh, M. J.; Loh, K. P. Single-Atom Catalysis: From Simple Reactions to the Synthesis of Complex Molecules. *Adv. Mater.* **2022**, *34* (25), 2103882.
(262) Li, L.; Chang, X.; Lin, X.; Zhao, Z.-J.; Gong, J. Theoretical insights into single-atom catalysts. *Chem. Soc. Rev.* **2020**, *49* (22), 8156−8178.
(263) Chen, Y.; Ji, S.; Chen, C.; Peng, Q.; Wang, D.; Li, Y. Single-Atom Catalysts: Synthetic Strategies and Electrochemical Applications. *Joule* **2018**, *2* (7), 1242−1264.
(264) Kottwitz, M.; Li, Y.; Wang, H.; Frenkel, A. I.; Nuzzo, R. G. Single Atom Catalysts: A Review of Characterization Methods. *Chem.—Methods* **2021**, *1* (6), 278−294.
(265) Roucoux, A.; Schulz, J.; Patin, H. Reduced Transition Metal Colloids: A Novel Family of Reusable Catalysts? *Chem. Rev.* **2002**, *102* (10), 3757−3778.
(266) Collins, G.; Schmidt, M.; McGlacken, G. P.; O'Dwyer, C.; Holmes, J. D. Stability, Oxidation, and Shape Evolution of PVP-Capped Pd Nanocrystals. *J. Phys. Chem. C* **2014**, *118* (12), 6522−6530.
(267) Zhong, R.-Y.; Sun, K.-Q.; Hong, Y.-C.; Xu, B.-Q. Impacts of Organic Stabilizers on Catalysis of Au Nanoparticles from Colloidal Preparation. *ACS Catal.* **2014**, *4* (11), 3982−3993.
(268) Vilé, G.; Almora-Barrios, N.; Mitchell, S.; López, N.; Pérez-Ramírez, J. From the Lindlar Catalyst to Supported Ligand-Modified Palladium Nanoparticles: Selectivity Patterns and Accessibility Constraints in the Continuous-Flow Three-Phase Hydrogenation of Acetylenic Compounds. *Chem.—Eur. J.* **2014**, *20* (20), 5926−5937.
(269) Witte, P. T.; Boland, S.; Kirby, F.; van Maanen, R.; Bleeker, B. F.; de Winter, D. A. M.; Post, J. A.; Geus, J. W.; Berben, P. H. NanoSelect Pd Catalysts: What Causes the High Selectivity of These Supported Colloidal Catalysts in Alkyne Semi-Hydrogenation? *ChemCatChem.* **2013**, *5* (2), 582−587.
(270) Witte, P. T.; Berben, P. H.; Boland, S.; Boymans, E. H.; Vogt, D.; Geus, J. W.; Donkervoort, J. G. BASF NanoSelect Technology: Innovative Supported Pd- and Pt-based Catalysts for Selective Hydrogenation Reactions. *Top. Catal.* **2012**, *55* (7), 505−511.
(271) Niu, M.; Wang, Y.; Li, W.; Jiang, J.; Jin, Z. Highly efficient and recyclable ruthenium nanoparticle catalyst for semihydrogenation of alkynes. *Catal. Commun.* **2013**, *38*, 77−81.
(272) Lee, S.; Shin, S.-J.; Baek, H.; Choi, Y.; Hyun, K.; Seo, M.; Kim, K.; Koh, D.-Y.; Kim, H.; Choi, M. Dynamic metal-polymer interaction for the design of chemoselective and long-lived hydrogenation catalysts. *Sci. Adv.* **2020**, *6* (28), No. eabb7369.
(273) Gu, J.; Jian, M.; Huang, L.; Sun, Z.; Li, A.; Pan, Y.; Yang, J.; Wen, W.; Zhou, W.; Lin, Y.; et al. Synergizing metal-support interactions and spatial confinement boosts dynamics of atomic nickel for hydrogenations. *Nat. Nanotechnol.* **2021**, *16* (10), 1141−1149.
(274) Wu, D.; Baaziz, W.; Gu, B.; Marinova, M.; Hernández, W. Y.; Zhou, W.; Vovk, E. I.; Ersen, O.; Safonova, O. V.; Addad, A.; et al. Surface molecular imprinting over supported metal catalysts for size-dependent selective hydrogenation reactions. *Nat. Catal.* **2021**, *4* (7), 595−606.
(275) Furukawa, S.; Ochi, K.; Luo, H.; Miyazaki, M.; Komatsu, T. Selective Stereochemical Catalysis Controlled by Specific Atomic Arrangement of Ordered Alloys. *ChemCatChem.* **2015**, *7* (21), 3472−3479.
(276) Zaera, F. Regio-, Stereo-, and Enantioselectivity in Hydrocarbon Conversion on Metal Surfaces. *Acc. Chem. Res.* **2009**, *42* (8), 1152−1160.
(277) LeBlond, C.; Wang, J.; Liu, J.; Andrews, A. T.; Sun, Y. K. Highly Enantioselective Heterogeneously Catalyzed Hydrogenation of α-Ketoesters under Mild Conditions. *J. Am. Chem. Soc.* **1999**, *121* (20), 4920−4921.
(278) Li, X.; Wells, R. P. K.; Wells, P. B.; Hutchings, G. J. New insights into the relationship between conversion and enantioselectivity for the asymmetric hydrogenation of alkyl pyruvate. *J. Catal.* **2004**, *221* (2), 653−656.
(279) Hutchings, G. J. Heterogeneous Asymmetric Catalysts: Strategies for Achieving High Enantioselection. *Annu. Rev. Mater. Res.* **2005**, *35* (1), 143−166.
(280) Bartok, M. Heterogeneous Catalytic Enantioselective Hydrogenation of Activated Ketones. *Curr. Org. Chem.* **2006**, *10* (13), 1533−1567.
(281) Mallat, T.; Szabó, S.; Schürch, M.; Göbel, U. W.; Baiker, A. Enantioselective hydrogenation of carbonyl compounds over Pd-Pt/alumina catalysts. *Catal. Lett.* **1997**, *47* (3/4), 221−227.
(282) Slipszenko, J. A.; Griffiths, S. P.; Johnston, P.; Simons, K. E.; Vermeer, W. A. H.; Wells, P. B. Enantioselective Hydrogenation: V. Hydrogenation of Butane-2,3-dione and of 3-Hydroxybutan-2-one Catalysed by Cinchona-Modified Platinum. *J. Catal.* **1998**, *179* (1), 267−276.
(283) von Arx, M.; Mallat, T.; Baiker, A. Unprecedented selectivity behaviour in the hydrogenation of an α,β-unsaturated ketone: hydrogenation of ketoisophorone over alumina-supported Pt and Pd. *J. Mol. Catal. A: Chem.* **1999**, *148* (1), 275−283.
(284) Szabo, A.; Künzle, N.; Mallat, T.; Baiker, A. Enantioselective hydrogenation of pyrrolidine-2,3,5-triones over the Pt-cinchonidine system. *Tetrahedron: Asymmetry* **1999**, *10* (1), 61−76.
(285) Kim, B.; Nakatsuji, M.; Mameda, T.; Kubota, T.; Fujita, M.; Sugimura, T.; Okamoto, Y. Kinetic Analysis of Enantioselective Hydrogenation of 2,3-(E)-Diarylpropenoic Acids over a Chiral Cinchona Alkaloid-Modified Pd/C Catalyst. *Bull. Chem. Soc. Jpn.* **2020**, *93* (1), 163−175.
(286) Györffy, N.; Tungler, A.; Fodor, M. Stereodifferentiation in heterogeneous catalytic hydrogenation. Kinetic resolution and asymmetric hydrogenation in the presence of (S)-proline: Catalyst-dependent processes. *J. Catal.* **2010**, *270* (1), 2−8.
(287) Rodríguez-García, L.; Hungerbühler, K.; Baiker, A.; Meemken, F. Enantioselection on Heterogeneous Noble Metal Catalyst: Proline-Induced Asymmetry in the Hydrogenation of Isophorone on Pd Catalyst. *J. Am. Chem. Soc.* **2015**, *137* (37), 12121−12130.
(288) Ruggera, J. F.; Merlo, A. B.; Diez, R. P.; Casella, M. L. Experimental and theoretical investigation of the enantioselective hydrogenation of ethyl pyruvate with a Pt catalyst with new non-cinchona chiral modifiers. *J. Mol. Catal. A: Chem.* **2016**, *423*, 233−239.
(289) Netscher, T.Synthesis of Vitamin E. In *Vitamins & Hormones*, Vol. *76*; Academic Press, 2007; pp 155−202.
(290) Wang, Y.; Mao, S.; Wang, Z.Preparation method of nitrogen-doped hierarchical-porous carbon-loaded nanometer Pd catalyst and product and application thereof. US Patent No. 0121855 A1, 2019.
(291) Deng, J.; Xiong, T.; Xu, F.; Li, M.; Han, C.; Gong, Y.; Wang, H.; Wang, Y. Inspired by bread leavening: one-pot synthesis of hierarchically porous carbon for supercapacitors. *Green Chem.* **2015**, *17* (7), 4053−4060.
(292) Tang, M.; Deng, J.; Li, M.; Li, X.; Li, H.; Chen, Z.; Wang, Y. 3D-interconnected hierarchical porous N-doped carbon supported ruthenium nanoparticles as an efficient catalyst for toluene and quinoline hydrogenation. *Green Chem.* **2016**, *18* (22), 6082−6090.
(293) Wang, Z.; Wang, C.; Mao, S.; Gong, Y.; Chen, Y.; Wang, Y. Pd nanoparticles anchored on amino-functionalized hierarchically porous carbon for efficient dehydrogenation of formic acid under ambient conditions. *J. Mater. Chem. A* **2019**, *7* (45), 25791−25795.

https://doi.org/10.1021/acscatal.2c05141
ACS Catal. 2023, 13, 974−1019

(294) Hammer, B.; Norskov, J. K. Why Gold Is the Noblest of All the Metals. *Nature* **1995**, *376* (6537), 238−240.
(295) Haruta, M.; Kobayashi, T.; Sano, H.; Yamada, N. Novel Gold Catalysts for the Oxidation of Carbon Monoxide at a Temperature far Below 0 °C. *Chem. Lett.* **1987**, *16* (2), 405−408.
(296) Haruta, M.; Yamada, N.; Kobayashi, T.; Iijima, S. Gold catalysts prepared by coprecipitation for low-temperature oxidation of hydrogen and of carbon monoxide. *J. Catal.* **1989**, *115* (2), 301−309.
(297) Min, B. K.; Friend, C. M. Heterogeneous Gold-Based Catalysis for Green Chemistry: Low-Temperature CO Oxidation and Propene Oxidation. *Chem. Rev.* **2007**, *107* (6), 2709−2724.
(298) Wu, Y. Y.; Mashayekhi, N. A.; Kung, H. H. Au-metal oxide support interface as catalytic active sites. *Catal. Sci. Technol.* **2013**, *3* (11), 2881−2891.
(299) Liu, J.; Chen, W.; Liu, X.; Zhou, K.; Li, Y. Au/$LaVO_4$ Nanocomposite: Preparation, characterization, and catalytic activity for CO oxidation. *Nano Res.* **2008**, *1* (1), 46−55.
(300) Tseng, C.-H.; Yang, T. C. K.; Wu, H.-E.; Chiang, H.-C. Catalysis of oxidation of carbon monoxide on supported gold nanoparticle. *J. Hazard. Mater.* **2009**, *166* (2), 686−694.
(301) Ma, Z.; Dai, S. Development of novel supported gold catalysts: A materials perspective. *Nano Res.* **2011**, *4* (1), 3−32.
(302) Valden, M.; Lai, X.; Goodman, D. W. Onset of Catalytic Activity of Gold Clusters on Titania with the Appearance of Nonmetallic Properties. *Science* **1998**, *281* (5383), 1647−1650.
(303) Lopez, N.; Janssens, T. V. W.; Clausen, B. S.; Xu, Y.; Mavrikakis, M.; Bligaard, T.; Nørskov, J. K. On the origin of the catalytic activity of gold nanoparticles for low-temperature CO oxidation. *J. Catal.* **2004**, *223* (1), 232−235.
(304) Falsig, H.; Hvolbæk, B.; Kristensen, I. S.; Jiang, T.; Bligaard, T.; Christensen, C. H.; Nørskov, J. K. Trends in the Catalytic CO Oxidation Activity of Nanoparticles. *Angew. Chem., Int. Ed.* **2008**, *47* (26), 4835−4839.
(305) Hvolbæk, B.; Janssens, T. V. W.; Clausen, B. S.; Falsig, H.; Christensen, C. H.; Nørskov, J. K. Catalytic activity of Au nanoparticles. *Nano Today* **2007**, *2* (4), 14−18.
(306) Lopez, N.; Nørskov, J. K. Catalytic CO Oxidation by a Gold Nanoparticle: A Density Functional Study. *J. Am. Chem. Soc.* **2002**, *124* (38), 11262−11263.
(307) Lemire, C.; Meyer, R.; Shaikhutdinov, S.; Freund, H.-J. Do Quantum Size Effects Control CO Adsorption on Gold Nanoparticles? *Angew. Chem., Int. Ed.* **2004**, *43* (1), 118−121.
(308) Overbury, S. H.; Schwartz, V.; Mullins, D. R.; Yan, W.; Dai, S. Evaluation of the Au size effect: CO oxidation catalyzed by Au/TiO2. *J. Catal.* **2006**, *241* (1), 56−65.
(309) Green, I. X.; Tang, W.; Neurock, M.; Yates, J. T. Spectroscopic Observation of Dual Catalytic Sites During Oxidation of CO on a Au/TiO_2 Catalyst. *Science* **2011**, *333* (6043), 736−739.
(310) Haruta, M.; Tsubota, S.; Kobayashi, T.; Kageyama, H.; Genet, M. J.; Delmon, B. Low-Temperature Oxidation of CO over Gold Supported on TiO_2, α-Fe_2O_3, and Co_3O_4. *J. Catal.* **1993**, *144* (1), 175−192.
(311) Wang, J.; Tan, H.; Yu, S.; Zhou, K. Morphological Effects of Gold Clusters on the Reactivity of Ceria Surface Oxygen. *ACS Catal.* **2015**, *5* (5), 2873−2881.
(312) Cargnello, M.; Doan-Nguyen, V. V. T.; Gordon, T. R.; Diaz, R. E.; Stach, E. A.; Gorte, R. J.; Fornasiero, P.; Murray, C. B. Control of Metal Nanocrystal Size Reveals Metal-Support Interface Role for Ceria Catalysts. *Science* **2013**, *341* (6147), 771−773.
(313) Haruta, M. Size- and support-dependency in the catalysis of gold. *Catal. Today* **1997**, *36* (1), 153−166.
(314) Kotobuki, M.; Leppelt, R.; Hansgen, D. A.; Widmann, D.; Behm, R. J. Reactive oxygen on a Au/TiO_2 supported catalyst. *J. Catal.* **2009**, *264* (1), 67−76.
(315) Yan, T.; Redman, D. W.; Yu, W.-Y.; Flaherty, D. W.; Rodriguez, J. A.; Mullins, C. B. CO oxidation on inverse Fe2O3/Au(111) model catalysts. *J. Catal.* **2012**, *294*, 216−222.
(316) Zhou, Z.; Kooi, S.; Flytzani-Stephanopoulos, M.; Saltsburg, H. The Role of the Interface in CO Oxidation on Au/CeO_2 Multilayer Nanotowers. *Adv. Funct. Mater.* **2008**, *18* (18), 2801−2807.
(317) Yao, Q.; Wang, C.; Wang, H.; Yan, H.; Lu, J. Revisiting the Au Particle Size Effect on TiO_2-Coated Au/TiO_2 Catalysts in CO Oxidation Reaction. *J. Phys. Chem. C* **2016**, *120* (17), 9174−9183.
(318) Qian, K.; Luo, L.; Bao, H.; Hua, Q.; Jiang, Z.; Huang, W. Catalytically active structures of SiO_2-supported Au nanoparticles in low-temperature CO oxidation. *Catal. Sci. Technol.* **2013**, *3* (3), 679−687.
(319) Widmann, D.; Behm, R. J. Activation of Molecular Oxygen and the Nature of the Active Oxygen Species for CO Oxidation on Oxide Supported Au Catalysts. *Acc. Chem. Res.* **2014**, *47* (3), 740−749.
(320) Crespo-Quesada, M.; Yarulin, A.; Jin, M.; Xia, Y.; Kiwi-Minsker, L. Structure Sensitivity of Alkynol Hydrogenation on Shape- and Size-Controlled Palladium Nanocrystals: Which Sites Are Most Active and Selective? *J. Am. Chem. Soc.* **2011**, *133* (32), 12787−12794.
(321) Prestianni, A.; Crespo-Quesada, M.; Cortese, R.; Ferrante, F.; Kiwi-Minsker, L.; Duca, D. Structure Sensitivity of 2-Methyl-3-butyn-2-ol Hydrogenation on Pd: Computational and Experimental Modeling. *J. Phys. Chem. C* **2014**, *118* (6), 3119−3128.
(322) Laskar, M.; Skrabalak, S. E. Decoupling the Geometric Parameters of Shape-Controlled Pd Nanocatalysts. *ACS Catal.* **2014**, *4* (4), 1120−1128.
(323) Yarulin, A.; Yuranov, I.; Cárdenas-Lizana, F.; Abdulkin, P.; Kiwi-Minsker, L. Size-Effect of Pd-(Poly(N-vinyl-2-pyrrolidone)) Nanocatalysts on Selective Hydrogenation of Alkynols with Different Alkyl Chains. *J. Phys. Chem. C* **2013**, *117* (26), 13424−13434.
(324) Osswald, J.; Giedigkeit, R.; Jentoft, R. E.; Armbrüster, M.; Girgsdies, F.; Kovnir, K.; Ressler, T.; Grin, Y.; Schlögl, R. Palladium-gallium intermetallic compounds for the selective hydrogenation of acetylene: Part I: Preparation and structural investigation under reaction conditions. *J. Catal.* **2008**, *258* (1), 210−218.
(325) Cao, Y.; Sui, Z.; Zhu, Y.; Zhou, X.; Chen, D. Selective Hydrogenation of Acetylene over Pd-In/Al_2O_3 Catalyst: Promotional Effect of Indium and Composition-Dependent Performance. *ACS Catal.* **2017**, *7* (11), 7835−7846.
(326) González-Fernández, A.; Berenguer-Murcia, Á.; Cazorla-Amorós, D.; Cárdenas-Lizana, F. Zn-Promoted Selective Gas-Phase Hydrogenation of Tertiary and Secondary C4 Alkynols over Supported Pd. *ACS Appl. Mater. Interfaces* **2020**, *12* (25), 28158−28168.
(327) Ball, M. R.; Rivera-Dones, K. R.; Gilcher, E. B.; Ausman, S. F.; Hullfish, C. W.; Lebrón, E. A.; Dumesic, J. A. AgPd and CuPd Catalysts for Selective Hydrogenation of Acetylene. *ACS Catal.* **2020**, *10* (15), 8567−8581.
(328) Pei, G.; Liu, X.; Chai, M.; Wang, A.; Zhang, T. Isolation of Pd atoms by Cu for semi-hydrogenation of acetylene: Effects of Cu loading. *Chin. J. Catal.* **2017**, *38* (9), 1540−1548.
(329) Jiang, L.; Liu, K.; Hung, S.-F.; Zhou, L.; Qin, R.; Zhang, Q.; Liu, P.; Gu, L.; Chen, H. M.; Fu, G.; et al. Facet engineering accelerates spillover hydrogenation on highly diluted metal nanocatalysts. *Nat. Nanotechnol.* **2020**, *15* (10), 848−853.
(330) Liu, J.; Uhlman, M. B.; Montemore, M. M.; Trimpalis, A.; Giannakakis, G.; Shan, J.; Cao, S.; Hannagan, R. T.; Sykes, E. C. H.; Flytzani-Stephanopoulos, M. Integrated Catalysis-Surface Science-Theory Approach to Understand Selectivity in the Hydrogenation of 1-Hexyne to 1-Hexene on PdAu Single-Atom Alloy Catalysts. *ACS Catal.* **2019**, *9* (9), 8757−8765.
(331) Hammer, B.; Morikawa, Y.; Nørskov, J. K. CO Chemisorption at Metal Surfaces and Overlayers. *Phys. Rev. Lett.* **1996**, *76* (12), 2141−2144.
(332) Ruban, A.; Hammer, B.; Stoltze, P.; Skriver, H. L.; Nørskov, J. K. Surface electronic structure and reactivity of transition and noble metals1Communication presented at the First Francqui Colloquium, Brussels, 19−20 February 1996.1. *J. Mol. Catal. A: Chem.* **1997**, *115* (3), 421−429.

https://doi.org/10.1021/acscatal.2c05141
ACS Catal. 2023, 13, 974−1019

(333) McCue, A. J.; Guerrero-Ruiz, A.; Rodríguez-Ramos, I.; Anderson, J. A. Palladium sulphide—A highly selective catalyst for the gas phase hydrogenation of alkynes to alkenes. *J. Catal.* **2016**, *340*, 10−16.
(334) Edwards, P. P.; Johnston, R. L.; Rao, C. N. R. On the Size-Induced Metal-Insulator Transition in Clusters and Small Particles. *Metal Clusters Chem.* **1999**, 1454−1481.
(335) Roduner, E. Size matters: why nanomaterials are different. *Chem. Soc. Rev.* **2006**, *35* (7), 583−592.
(336) Li, J.; Li, X.; Zhai, H.-J.; Wang, L.-S. Au20: A Tetrahedral Cluster. *Science* **2003**, *299* (5608), 864−867.
(337) Aruna, I.; Mehta, B. R.; Malhotra, L. K.; Shivaprasad, S. M. Size dependence of core and valence binding energies in Pd nanoparticles: Interplay of quantum confinement and coordination reduction. *J. Appl. Phys.* **2008**, *104* (6), 064308.
(338) Springborg, M.; Dong, Y.Chapter 4 The Jellium Model. In *Handbook of Metal Physics*, Springborg, M., Dong, Y., Eds.; Vol. *1*; Elsevier, 2006; pp 37−44.
(339) Polozkov, R. G.; Ivanov, V. K.; Verkhovtsev, A. V.; Korol, A. V.; Solov'yov, A. V. New applications of the jellium model for the study of atomic clusters. *J. Phys: Conf. Ser.* **2013**, *438*, 012009.
(340) Taketoshi, A.; Haruta, M. Size- and Structure-specificity in Catalysis by Gold Clusters. *Chem. Lett.* **2014**, *43* (4), 380−387.
(341) Visikovskiy, A.; Matsumoto, H.; Mitsuhara, K.; Nakada, T.; Akita, T.; Kido, Y. Electronic d-band properties of gold nanoclusters grown on amorphous carbon. *Phys. Rev. B* **2011**, *83* (16), 165428.
(342) Aiyer, H. N.; Vijayakrishnan, V.; Subbanna, G. N.; Rao, C. N. R. Investigations of Pd clusters by the combined use of HREM, STM, high-energy spectroscopies and tunneling conductance measurements. *Surf. Sci.* **1994**, *313* (3), 392−398.
(343) Pesika, N. S.; Stebe, K. J.; Searson, P. C. Relationship between Absorbance Spectra and Particle Size Distributions for Quantum-Sized Nanocrystals. *J. Phys. Chem. B* **2003**, *107* (38), 10412−10415.
(344) Vázquez-Vázquez, C.; Bañobre-López, M.; Mitra, A.; López-Quintela, M. A.; Rivas, J. Synthesis of Small Atomic Copper Clusters in Microemulsions. *Langmuir* **2009**, *25* (14), 8208−8216.
(345) Hövel, H.; Barke, I. Morphology and electronic structure of gold clusters on graphite: Scanning-tunneling techniques and photoemission. *Prog. Surf. Sci.* **2006**, *81* (2), 53−111.
(346) Taylor, K. J.; Pettiette-Hall, C. L.; Cheshnovsky, O.; Smalley, R. E. Ultraviolet photoelectron spectra of coinage metal clusters. *J. Chem. Phys.* **1992**, *96* (4), 3319−3329.
(347) Murray, J. S.; Lane, P.; Politzer, P. Expansion of the σ-hole concept. *J. Mol. Model.* **2009**, *15* (6), 723−729.
(348) Clark, T.; Hennemann, M.; Murray, J. S.; Politzer, P. Halogen bonding: the σ-hole. *J. Mol. Model.* **2007**, *13* (2), 291−296.
(349) Stenlid, J. H.; Brinck, T. Extending the σ-Hole Concept to Metals: An Electrostatic Interpretation of the Effects of Nanostructure in Gold and Platinum Catalysis. *J. Am. Chem. Soc.* **2017**, *139* (32), 11012−11015.
(350) Hammer, B.; Norskov, J. K. Electronic factors determining the reactivity of metal surfaces. *Surf. Sci.* **1995**, *343* (3), 211−220.
(351) Kitchin, J. R.; Nørskov, J. K.; Barteau, M. A.; Chen, J. G. Modification of the surface electronic and chemical properties of Pt(111) by subsurface 3d transition metals. *J. Chem. Phys.* **2004**, *120* (21), 10240−10246.
(352) Nilsson, A.; Pettersson, L. G. M.; Hammer, B.; Bligaard, T.; Christensen, C. H.; Norskov, J. K. The electronic structure effect in heterogeneous catalysis. *Catal. Lett.* **2005**, *100* (3−4), 111−114.
(353) Pallassana, V.; Neurock, M.; Hansen, L. B.; Hammer, B.; Norskov, J. K. Theoretical analysis of hydrogen chemisorption on Pd(111), Re(0001) and Pd(ML)/Re(0001), Re(ML)/Pd(111) pseudomorphic overlayers. *Phys. Rev. B* **1999**, *60* (8), 6146−6154.
(354) Mao, S.; Wang, Z.; Chen, Z.; Wu, K.; Zhang, K.; Li, Q.; Yan, H.; Lü, G.; Huang, G.; Wang, Y. Towards the selectivity distinction of phenol hydrogenation on noble metal catalysts. *Nano Mater. Sci.* **2020**, DOI: 10.1016/j.nanoms.2020.11.002.
(355) Santos, E.; Schmickler, W. d-Band Catalysis in Electrochemistry. *ChemPhysChem* **2006**, *7* (11), 2282−2285.
(356) Pallassana, V.; Neurock, M. Electronic Factors Governing Ethylene Hydrogenation and Dehydrogenation Activity of Pseudomorphic PdML/Re(0001), PdML/Ru(0001), Pd(111), and PdML/Au(111) Surfaces. *J. Catal.* **2000**, *191* (2), 301−317.
(357) Ando, F.; Tanabe, T.; Gunji, T.; Kaneko, S.; Takeda, T.; Ohsaka, T.; Matsumoto, F. Effect of the d-Band Center on the Oxygen Reduction Reaction Activity of Electrochemically Dealloyed Ordered Intermetallic Platinum-Lead (PtPb) Nanoparticles Supported on TiO2-Deposited Cup-Stacked Carbon Nanotubes. *ACS Appl. Nano Mater.* **2018**, *1* (6), 2844−2850.
(358) Pettersson, L. G. M.; Nilsson, A. A Molecular Perspective on the d-Band Model: Synergy Between Experiment and Theory. *Top. Catal.* **2014**, *57* (1), 2−13.
(359) Calle-Vallejo, F.; Martínez, J. I.; García-Lastra, J. M.; Sautet, P.; Loffreda, D. Fast Prediction of Adsorption Properties for Platinum Nanocatalysts with Generalized Coordination Numbers. *Angew. Chem., Int. Ed.* **2014**, *53* (32), 8316−8319.
(360) Calle-Vallejo, F.; Tymoczko, J.; Colic, V.; Vu, Q. H.; Pohl, M. D.; Morgenstern, K.; Loffreda, D.; Sautet, P.; Schuhmann, W.; Bandarenka, A. S. Finding optimal surface sites on heterogeneous catalysts by counting nearest neighbors. *Science* **2015**, *350* (6257), 185−189.
(361) Ma, X.; Xin, H. Orbitalwise Coordination Number for Predicting Adsorption Properties of Metal Nanocatalysts. *Phys. Rev. Lett.* **2017**, *118* (3), 036101.
(362) Roling, L. T.; Li, L.; Abild-Pedersen, F. Configurational Energies of Nanoparticles Based on Metal-Metal Coordination. *J. Phys. Chem. C* **2017**, *121* (41), 23002−23010.
(363) Roling, L. T.; Abild-Pedersen, F. Structure-Sensitive Scaling Relations: Adsorption Energies from Surface Site Stability. *ChemCatChem.* **2018**, *10* (7), 1643−1650.
(364) Roling, L. T.; Choksi, T. S.; Abild-Pedersen, F. A coordination-based model for transition metal alloy nanoparticles. *Nanoscale* **2019**, *11* (10), 4438−4452.
(365) Xin, H.; Vojvodic, A.; Voss, J.; Nørskov, J. K.; Abild-Pedersen, F. Effects of *d*-band shape on the surface reactivity of transition-metal alloys. *Phys. Rev. B* **2014**, *89* (11), 115114.
(366) Bhattacharjee, S.; Waghmare, U. V.; Lee, S.-C. An improved d-band model of the catalytic activity of magnetic transition metal surfaces. *Sci. Rep.* **2016**, *6* (1), 35916.
(367) Saini, S.; Halldin Stenlid, J.; Abild-Pedersen, F. Electronic structure factors and the importance of adsorbate effects in chemisorption on surface alloys. *NPJ. Comput. Mater.* **2022**, *8* (1), 163.
(368) Ruiz Puigdollers, A.; Schlexer, P.; Tosoni, S.; Pacchioni, G. Increasing Oxide Reducibility: The Role of Metal/Oxide Interfaces in the Formation of Oxygen Vacancies. *ACS Catal.* **2017**, *7* (10), 6493−6513.
(369) Vayssilov, G. N.; Lykhach, Y.; Migani, A.; Staudt, T.; Petrova, G. P.; Tsud, N.; Skála, T.; Bruix, A.; Illas, F.; Prince, K. C.; et al. Support nanostructure boosts oxygen transfer to catalytically active platinum nanoparticles. *Nat. Mater.* **2011**, *10* (4), 310−315.
(370) Lykhach, Y.; Kozlov, S. M.; Skála, T.; Tovt, A.; Stetsovych, V.; Tsud, N.; Dvořák, F.; Johánek, V.; Neitzel, A.; Mysliveček, J.; et al. Counting electrons on supported nanoparticles. *Nat. Mater.* **2016**, *15* (3), 284−288.
(371) Mao, S.; Wang, C.; Wang, Y. The chemical nature of N doping on N doped carbon supported noble metal catalysts. *J. Catal.* **2019**, *375*, 456−465.
(372) Zheng, X.; Qin, M.; Ma, S.; Chen, Y.; Ning, H.; Yang, R.; Mao, S.; Wang, Y. Strong Oxide-Support Interaction over IrO2/V2O5 for Efficient pH-Universal Water Splitting. *Adv. Sci.* **2022**, *9* (11), 2104636.
(373) Liu, S.; Li, Y.; Yu, X.; Han, S.; Zhou, Y.; Yang, Y.; Zhang, H.; Jiang, Z.; Zhu, C.; Li, W.-X.; et al. Tuning crystal-phase of bimetallic single-nanoparticle for catalytic hydrogenation. *Nat. Commun.* **2022**, *13* (1), 4559.

(374) Wang, Y.; Yao, J.; Li, H.; Su, D.; Antonietti, M. Highly Selective Hydrogenation of Phenol and Derivatives over a Pd@ Carbon Nitride Catalyst in Aqueous Media. *J. Am. Chem. Soc.* **2011**, *133* (8), 2362−2365.
(375) Xu, X.; Li, H.; Wang, Y. Selective Hydrogenation of Phenol to Cyclohexanone in Water over Pd@N-Doped Carbon Derived from Ionic-Liquid Precursors. *ChemCatChem.* **2014**, *6* (12), 3328−3332.
(376) Xu, X.; Tang, M.; Li, M.; Li, H.; Wang, Y. Hydrogenation of Benzoic Acid and Derivatives over Pd Nanoparticles Supported on N-Doped Carbon Derived from Glucosamine Hydrochloride. *ACS Catal.* **2014**, *4* (9), 3132−3135.
(377) Wei, Z.; Wang, J.; Mao, S.; Su, D.; Jin, H.; Wang, Y.; Xu, F.; Li, H.; Wang, Y. In Situ-Generated CoO-Co_3O_4/N-Doped Carbon Nanotubes Hybrids as Efficient and Chemoselective Catalysts for Hydrogenation of Nitroarenes. *ACS Catal.* **2015**, *5* (8), 4783−4789.
(378) Jin, H.; Wang, J.; Su, D.; Wei, Z.; Pang, Z.; Wang, Y. In situ Cobalt-Cobalt Oxide/N-Doped Carbon Hybrids As Superior Bifunctional Electrocatalysts for Hydrogen and Oxygen Evolution. *J. Am. Chem. Soc.* **2015**, *137* (7), 2688−2694.
(379) Wang, J.; Wei, Z.; Gong, Y.; Wang, S.; Su, D.; Han, C.; Li, H.; Wang, Y. Ni-promoted synthesis of graphitic carbon nanotubes from in situ produced graphitic carbon for dehydrogenation of ethylbenzene. *Chem. Commun.* **2015**, *51* (64), 12859−12862.
(380) Wang, S.; Wang, J.; Zhu, M.; Bao, X.; Xiao, B.; Su, D.; Li, H.; Wang, Y. Molybdenum-Carbide-Modified Nitrogen-Doped Carbon Vesicle Encapsulating Nickel Nanoparticles: A Highly Efficient, Low-Cost Catalyst for Hydrogen Evolution Reaction. *J. Am. Chem. Soc.* **2015**, *137* (50), 15753−15759.
(381) Su, D.; Wei, Z.; Mao, S.; Wang, J.; Li, Y.; Li, H.; Chen, Z.; Wang, Y. Reactivity and mechanism investigation of selective hydrogenation of 2,3,5-trimethylbenzoquinone on in situ generated metallic cobalt. *Catal. Sci. Technol.* **2016**, *6* (12), 4503−4510.
(382) Kong, X.; Fang, Z.; Bao, X.; Wang, Z.; Mao, S.; Wang, Y. Efficient hydrogenation of stearic acid over carbon coated NiFe catalyst. *J. Catal.* **2018**, *367*, 139−149.
(383) Wang, J.; Wei, Z.; Mao, S.; Li, H.; Wang, Y. Highly uniform Ru nanoparticles over N-doped carbon: pH and temperature-universal hydrogen release from water reduction. *Energy Environ. Sci.* **2018**, *11* (4), 800−806.
(384) Wei, Z.; Li, Y.; Wang, J.; Li, H.; Wang, Y. Chemoselective hydrogenation of phenol to cyclohexanol using heterogenized cobalt oxide catalysts. *Chin. Chem. Lett.* **2018**, *29* (6), 815−818.
(385) Wang, S.; Zhu, M.; Bao, X.; Wang, J.; Chen, C.; Li, H.; Wang, Y. Synthesis of Mesoporous Fe·N/C Materials with High Catalytic Performance in the Oxygen Reduction Reaction. *ChemCatChem.* **2015**, *7* (18), 2937−2944.
(386) Bao, X.; Wang, J.; Lian, X.; Jin, H.; Wang, S.; Wang, Y. Ni/nitrogen-doped graphene nanotubes acted as a valuable tailor for remarkably enhanced hydrogen evolution performance of platinum-based catalysts. *J. Mater. Chem. A* **2017**, *5* (31), 16249−16254.
(387) Jin, H.; Chen, J.; Mao, S.; Wang, Y. Transition Metal Induced the Contraction of Tungsten Carbide Lattice as Superior Hydrogen Evolution Reaction Catalyst. *ACS Appl. Mater. Interfaces* **2018**, *10* (26), 22094−22101.
(388) Jin, H.; Zhang, H.; Chen, J.; Mao, S.; Jiang, Z.; Wang, Y. A general synthetic approach for hexagonal phase tungsten nitride composites and their application in the hydrogen evolution reaction. *J. Mater. Chem. A* **2018**, *6* (23), 10967−10975.
(389) Nørskov, J. K.; Studt, F.; Abild-Pedersen, F.; Bligaard, T. The Electronic Factor in Heterogeneous Catalysis. *Fundam. Concepts Hetero. Catal.* **2014**, 114−137.
(390) Greiner, M. T.; Jones, T. E.; Beeg, S.; Zwiener, L.; Scherzer, M.; Girgsdies, F.; Piccinin, S.; Armbrüster, M.; Knop-Gericke, A.; Schlögl, R. Free-atom-like d states in single-atom alloy catalysts. *Nat. Chem.* **2018**, *10* (10), 1008−1015.
(391) Spivey, T. D.; Holewinski, A. Selective Interactions between Free-Atom-like d-States in Single-Atom Alloy Catalysts and Near-Frontier Molecular Orbitals. *J. Am. Chem. Soc.* **2021**, *143* (31), 11897−11902.
(392) Tang, M.; Mao, S.; Li, M.; Wei, Z.; Xu, F.; Li, H.; Wang, Y. RuPd Alloy Nanoparticles Supported on N-Doped Carbon as an Efficient and Stable Catalyst for Benzoic Acid Hydrogenation. *ACS Catal.* **2015**, *5* (5), 3100−3107.
(393) Tang, M.; Mao, S.; Li, X.; Chen, C.; Li, M.; Wang, Y. Highly effective Ir-based catalysts for benzoic acid hydrogenation: experiment- and theory-guided catalyst rational design. *Green Chem.* **2017**, *19* (7), 1766−1774.
(394) Wang, S.-H.; Pillai, H. S.; Wang, S.; Achenie, L. E. K.; Xin, H. Infusing theory into deep learning for interpretable reactivity prediction. *Nat. Commun.* **2021**, *12* (1), 5288.
(395) Feng, H.; Ding, H.; Wang, S.; Liang, Y.; Deng, Y.; Yang, Y.; Wei, M.; Zhang, X. Machine-Learning-Assisted Catalytic Performance Predictions of Single-Atom Alloys for Acetylene Semihydrogenation. *ACS Appl. Mater. Interfaces* **2022**, *14* (22), 25288−25296.
(396) Riley, C.; Zhou, S.; Kunwar, D.; De La Riva, A.; Peterson, E.; Payne, R.; Gao, L.; Lin, S.; Guo, H.; Datye, A. Design of Effective Catalysts for Selective Alkyne Hydrogenation by Doping of Ceria with a Single-Atom Promotor. *J. Am. Chem. Soc.* **2018**, *140* (40), 12964−12973.
(397) Li, Y.; Cao, Y.; Ge, X.; Zhang, H.; Yan, K.; Zhang, J.; Qian, G.; Jiang, Z.; Gong, X.; Li, A.; et al. Pt-O_4 moiety induced electron localization toward In_2O-Triggered acetylene Semi-Hydrogenation. *J. Catal.* **2022**, *407*, 290−299.
(398) Fan, R.; Wang, H.; Zheng, X.; Chen, J.; Ou, Y.; Wang, Y.; Mao, S. Fe2 Dimers for Non-Polar Diatomic O_2 Electroreduction. *ChemSusChem* **2022**, *15* (15), No. e202200532.
(399) Zheng, J.; Huang, L.; Cui, C.-H.; Chen, Z.-C.; Liu, X.-F.; Duan, X.; Cao, X.-Y.; Yang, T.-Z.; Zhu, H.; Shi, K.; et al. Ambient-pressure synthesis of ethylene glycol catalyzed by C_{60}-buffered Cu/SiO_2. *Science* **2022**, *376* (6590), 288−292.
(400) Huang, Z.; Liang, J.-X.; Tang, D.; Chen, Y.; Qu, W.; Hu, X.; Chen, J.; Dong, Y.; Xu, D.; Golberg, D.; et al. Interplay between remote single-atom active sites triggers speedy catalytic oxidation. *Chem.* **2022**, *8* (11), 3008−3017.
(401) Makowski, P.; Demir Cakan, R.; Antonietti, M.; Goettmann, F.; Titirici, M.-M. Selective partial hydrogenation of hydroxy aromatic derivatives with palladium nanoparticles supported on hydrophilic carbon. *Chem. Commun.* **2008**, No. 8, 999.
(402) Pérez, Y.; Fajardo, M.; Corma, A. Highly selective palladium supported catalyst for hydrogenation of phenol in aqueous phase. *Catal. Commun.* **2011**, *12* (12), 1071−1074.
(403) Zhang, F.; Chen, S.; Li, H.; Zhang, X.-M.; Yang, H. Pd nanoparticles embedded in the outershell of a mesoporous core-shell catalyst for phenol hydrogenation in pure water. *RSC Adv.* **2015**, *5* (124), 102811−102817.
(404) Li, Y.; Xu, X.; Zhang, P.; Gong, Y.; Li, H.; Wang, Y. Highly selective Pd@mpg-C_3N_4 catalyst for phenol hydrogenation in aqueous phase. *RSC Adv.* **2013**, *3* (27), 10973−10982.
(405) Fang, W.; Wang, C.; Liu, Z.; Wang, L.; Liu, L.; Li, H.; Xu, S.; Zheng, A.; Qin, X.; Liu, L.; et al. Physical mixing of a catalyst and a hydrophobic polymer promotes CO hydrogenation through dehydration. *Science* **2022**, *377* (6604), 406−410.
(406) Jin, Z.; Wang, L.; Zuidema, E.; Mondal, K.; Zhang, M.; Zhang, J.; Wang, C.; Meng, X.; Yang, H.; Mesters, C.; et al. Hydrophobic zeolite modification for in situ peroxide formation in methane oxidation to methanol. *Science* **2020**, *367* (6474), 193−197.
(407) Liu, H.; Jiang, T.; Han, B.; Liang, S.; Zhou, Y. Selective Phenol Hydrogenation to Cyclohexanone Over a Dual Dual Supported Pd-Lewis Acid Catalyst. *Science* **2009**, *326* (5957), 1250−1252.
(408) Chen, Y.; Kong, X.; Mao, S.; Wang, Z.; Gong, Y.; Wang, Y. Study of the role of alkaline sodium additive in selective hydrogenation of phenol. *Chin. J. Catal.* **2019**, *40* (10), 1516−1524.
(409) Scirè, S.; Crisafulli, C.; Maggiore, R.; Minicò, S.; Galvagno, S. FT-IR characterization of alkali-doped Pd catalysts for the selective hydrogenation of phenol to cyclohexanone. *Appl. Surf. Sci.* **1996**, *93* (4), 309−316.
(410) Ning, H.; Chen, Y.; Wang, Z.; Mao, S.; Chen, Z.; Gong, Y.; Wang, Y. Selective upgrading of biomass-derived benzylic ketones by

(formic acid)-Pd/HPC-NH2 system with high efficiency under ambient conditions. *Chem.* **2021**, *7* (11), 3069−3084.
(411) Qin, R.; Zhou, L.; Liu, P.; Gong, Y.; Liu, K.; Xu, C.; Zhao, Y.; Gu, L.; Fu, G.; Zheng, N. Alkali ions secure hydrides for catalytic hydrogenation. *Nat. Catal.* **2020**, *3* (9), 703−709.
(412) Lu, B.; Wang, Z.; Ma, S.; Mao, S.; Chen, Z.; Wang, Y. Spatial charge separation induced new mechanism of efficient C−C coupling by forming ion-pair intermediates. *Chem. Catal.* **2021**, *1* (7), 1449−1465.
(413) Mao, S.; Sun, X.; Li, B.; Su, D. S. Rationale of the effects from dopants on C−H bond activation for sp^2 hybridized nanostructured carbon catalysts. *Nanoscale* **2015**, *7* (40), 16597−16600.

https://doi.org/10.1021/acscatal.2c05141
ACS Catal. 2023, 13, 974−1019